Durham E-Theses

Weak interactions and excited states from Coulomb-attenuated DFT

DWYER, AUSTIN,DERMOT

How to cite:

DWYER, AUSTIN,DERMOT (2011) *Weak interactions and excited states from Coulomb-attenuated DFT*, Durham theses, Durham University. Available at Durham E-Theses Online: http://etheses.dur.ac.uk/1404/

Use policy

The full-text may be used and/or reproduced, and given to third parties in any format or medium, without prior permission or charge, for personal research or study, educational, or not-for-profit purposes provided that:

- a full bibliographic reference is made to the original source
- a link is made to the metadata record in Durham E-Theses
- the full-text is not changed in any way

The full-text must not be sold in any format or medium without the formal permission of the copyright holders.

Please consult the full Durham E-Theses policy for further details.

Academic Support Office, Durham University, University Office, Old Elvet, Durham DH1 3HP
e-mail: e-theses.admin@dur.ac.uk Tel: +44 0191 334 6107
http://etheses.dur.ac.uk

Weak interactions and excited states from Coulomb-attenuated DFT

Austin Dwyer

Department of Chemistry

Durham University

Submitted in partial fulfilment of the requirements

for the degree of Doctor of Philosophy

2011

Abstract

Density functional theory (DFT) is currently the most widely applied electronic structure theory in Chemistry. It is favoured for its computational efficiency, coupled with good accuracy. Although formally exact, approximations are required when practically applied. In the Kohn-Sham formalism, these approximations are contained within the exchange-correlation functional. Well established exchange-correlation functionals, such as the ubiquitous B3LYP, provide reasonable accuracy, but their continued use is increasingly based on the collective experience with the functional that has been accumulated, rather than the results that can be achieved. This thesis considers the circumstances under which conventional functionals fail and how a recent modification—coulomb attenuation—can resolve such issues.

An outline of basic electronic structure theory is provided in chapter 1, particularly the formulation of the Hartree-Fock approach. This is extended to more sophisticated wavefunction based methods. Chapter 2 provides a formal proof for the validity of DFT as well as a framework for its implementation. A recently developed exchange-correlation functional (CAM-B3LYP) based on a varying quantity of exact exchange is outlined. Also discussed is the time-dependent DFT (TDDFT) approach to the determination of excitation energies, its failures and how such failures can be predicted and eliminated. The subsequent chapters consider the application of CAM-B3LYP to the description of weak interactions and excited states.

Chapter 3 considers some key problems facing modern DFT—dispersion, fractional spins and fractional charges—in terms of the force and the Feynman electron density distortion, in addition to the conventional viewpoint of the energy. Two model systems, H_2 and H_2^+ are employed to illustrate how increasing quantities of exact exchange can increase the fractional spin error while decreasing the fractional charge error, respectively. This is reflected in the improved description offered by CAM-B3LYP for H_2 and the corresponding poor performance for H_2^+.

Chapter 4 takes a more detailed look at the dispersion interaction. C_6 dispersion coefficients are calculated using a range of functionals—CAM-B3LYP showing a clear improvement over GGA and hybrid functionals. Dispersion corrected potential energy surfaces and interaction energies are determined with CAM-B3LYP providing comparable accuracy to other, existing long-range corrected functionals.

Chapters 5 and 6 consider the application of CAM-B3LYP to the excited states of large systems of chemical and biological importance, respectively. In the former, the difficulty of comparing theoretically determined excitation energies with experimentally observed absorption spectra is of particular focus. In the latter, the failure of conventional functionals to correctly predict the energy and character of charge-transfer excitations is highlighted. For both cases, it is shown that CAM-B3LYP can provide a significant improvement over conventional functionals, all but eradicating the charge-transfer issue in the latter case.

Chapter 7 further investigates the charge-transfer issue experienced by conventional functionals and illustrates how the error can manifest itself as an inaccuracy in the *character* of an excited state rather than the energy. CAM-B3LYP provides an accurate description of both aspects. Triplet excitation energies are determined from TDDFT and the ΔSCF approach—the latter providing improved results for conventional functionals.

Contents

List of Figures

List of Tables

Author's Declaration

The material contained within this thesis has not previously been submitted for a degree at the University of Durham or any other university. The research reported within this thesis has been conducted by the author unless otherwise indicated.

Copyright Notice

The copyright of this thesis rests with the author. No quotation from it should be published without their prior written consent and information derived from it should be acknowledged.

Acknowledgements

Firstly, the most credit must go to David Tozer. His expert supervision and endless enthusiasm have been invaluable sources of motivation during the last three years.

I'd like to thank Michael Peach, particularly for his help with computational issues I've encountered during the last three years. I'd also like to thank Alex Borgoo and the undergraduate students I've had the pleasure of working with: John Kattirtzi, Paul Wiggins, David Griffiths and Jonathan Gledhill.

For providing me the opportunity to work collaboratively with them on the retinal and pyrene projects, I thank Marius Wanko and Todd Marder, respectively. I'd also like to thank Andrew Crawford for his help and good humour while working on the latter.

There are four people without whose excellent teaching, I would never have found myself in the position of being able to do a PhD. Therefore, I thank Kevin Frobisher, Theresa Alexander, Stephen Roberts and Fred Manby.

I'd like to thank my family for more reasons than I can list here: Marian, Ben, Owen, Liam, Laura, Callum, Billy and Brian.

I'd like to thank everyone from 200 and 200X with whom, over the last few years, I've had the pleasure of sharing tea, coffee, cake, curry, poker, paintball ...

Finally, and in no particular order, I thank: Ant, Sam, Jeff, Layla, Furzana, Elise, Luke and Emma.

Chapter 1

Introduction

The ultimate goal of the quantum chemist is the exact solution of the non-relativistic electronic Schrödinger equation, involving the description of all electrostatic interactions between particles and the motion of the particles, including all quantum effects. Traditionally, the many-electron wavefunction was used as the central quantity in *ab initio* calculations. This led to the development of Hartree-Fock theory and, later, more complete electronic structure theories.

Alternatively, the density can be used in the formally exact density functional theory (DFT). The comparative simplicity of the density with respect to the wavefunction makes this theory much less computationally intensive. It is this advantage, coupled with the possibility of high quality results, which drives the development of DFT.

Given the computational similarity of the theories, an outline of the Hartree-Fock procedure and other wavefunction methods will be given before discussing DFT in detail in chapter 2.

1.1 Hartree-Fock Theory

The energy, E, of any molecular system is described by the non-relativistic Schrödinger equation[1]

$$\hat{H}\Psi_{\text{tot}} = E\Psi_{\text{tot}} \tag{1.1}$$

where the Hamiltonian operator, in atomic units ($m_\mathrm{e} = \hbar = e = 4\pi\epsilon_0 = 1$), is

$$\hat{H} = -\frac{1}{2}\sum_{i=1}^{N}\nabla_i^2 - \sum_{i=1}^{N}\sum_{A=1}^{M}\frac{Z_A}{r_{iA}} + \sum_{i=1}^{N}\sum_{j>i}^{N}\frac{1}{r_{ij}} - \sum_{A=1}^{M}\frac{\nabla_A^2}{2M_A} + \sum_{A=1}^{M}\sum_{B>A}^{M}\frac{Z_A Z_B}{R_{AB}}. \tag{1.2}$$

In any system, the mass of the nuclei are far greater than the mass of the electrons, to the extent that for our purposes, the nuclei can be considered as fixed in space. Successive calculations can be done at altered nuclear configurations, building up a potential energy surface. This decoupling of the electronic and nuclear motions, known as the Born-Oppenheimer[2] approximation, allows the total wavefunction to be written as a product of the nuclear wavefunction and a single electronic wavefunction

$$\Psi_\mathrm{tot} = \Psi_\mathrm{N}(\mathbf{R})\Psi_\mathrm{e}(\mathbf{r};\mathbf{R}) \tag{1.3}$$

where the wavefunctions are functions of all electronic ($\mathbf{r}$) and nuclear ($\mathbf{R}$) coordinates. The parametric dependence of the electronic wavefunction on the nuclear coordinates has been included, which accounts for the variation of the electronic wavefunction with different nuclear configurations. As a consequence of the fixed nuclear framework in the Born-Oppenheimer approximation, the kinetic energy of the nuclei is zero and the electrostatic repulsion between the nuclei is a constant. The result is a theory in which the electronic energy is found as a solution to the time-independent electronic Schrödinger equation

$$\hat{H}_\mathrm{e}\Psi_\mathrm{e}(\mathbf{r}) = E_\mathrm{e}\Psi_\mathrm{e}(\mathbf{r}) \tag{1.4}$$

where $\hat{H}_\mathrm{e}$ is the electronic Hamiltonian and E_e is the electronic energy. The electronic Hamiltonian

$$\hat{H}_\mathrm{e} = -\frac{1}{2}\sum_{i=1}^{N}\nabla_i^2 - \sum_{i=1}^{N}\sum_{A=1}^{M}\frac{Z_A}{r_{iA}} + \sum_{i=1}^{N}\sum_{j>i}^{N}\frac{1}{r_{ij}}, \tag{1.5}$$

comprises terms describing the kinetic energy of the electrons, the interactions between the electrons and the nuclei and the interaction between the electrons, respectively. The nuclear-nuclear term has been omitted for clarity and will be done so for the remainder of the thesis. The Born-Oppenheimer approximation is only valid if a change in nuclear

position does not coincide with a change in electronic state. If two states are sufficiently close in energy that a change in nuclear coordinates does cause a change of state then the Born-Oppenheimer approximation breaks down and the energies of the states are poorly described. All our calculations therefore concern the energy of the electrons within a fixed nuclear framework.

Hartree-Fock theory[3–7] approximates the electronic wavefunction as a single determinant.[8,9] The use of a determinant ensures the wavefunction is antisymmetric with respect to the interchange of the space-spin coordinates of a pair of electrons, thereby satisfying the Pauli principle.[10] The wavefunction is

$$\Psi_{\mathrm{SD}} = \frac{1}{\sqrt{n!}} \begin{vmatrix} \chi_1(\mathbf{x}_1) & \chi_2(\mathbf{x}_1) & \cdots & \chi_n(\mathbf{x}_1) \\ \chi_1(\mathbf{x}_2) & \chi_2(\mathbf{x}_2) & \cdots & \chi_n(\mathbf{x}_2) \\ \vdots & \vdots & \ddots & \vdots \\ \chi_1(\mathbf{x}_n) & \chi_2(\mathbf{x}_n) & \cdots & \chi_n(\mathbf{x}_n) \end{vmatrix} \tag{1.6}$$

which is an antisymmetrized product of one-electron orthonormal spin orbitals. Each orbital $\chi_i(\mathbf{x}_i)$ is the product of a spatial $\psi_i(\mathbf{r})$ and spin $\sigma(s)$ component.

To determine the energy of a Slater determinant it is helpful to separate the electronic Hamiltonian into a sum of one- and two-electron operators,

$$\hat{H}_{\mathrm{e}} = \sum_{i=1}^{N} \hat{h}(\mathbf{r}_i) + \sum_{i=1}^{N} \sum_{j>i}^{N} \frac{1}{r_{ij}}. \tag{1.7}$$

The energy of a Slater determinant is then given by the expectation value,

$$E_{\mathrm{e}} = \langle \Psi_{\mathrm{SD}} | \, \hat{H}_{\mathrm{e}} \, | \Psi_{\mathrm{SD}} \rangle \tag{1.8}$$

$$= \sum_{i=1}^{N} \langle \chi_i | \, \hat{h} \, | \chi_i \rangle + \frac{1}{2} \sum_{i=1}^{N} \sum_{j=1}^{N} \langle \chi_i \chi_j | \, \frac{1}{r_{ij}} \, | \chi_i \chi_j \rangle - \langle \chi_i \chi_j | \, \frac{1}{r_{ij}} \, | \chi_j \chi_i \rangle \tag{1.9}$$

$$= \sum_{i=1}^{N} h_{ii} + \frac{1}{2} \sum_{i=1}^{N} \sum_{j=1}^{n} (J_{ij} - K_{ij}). \tag{1.10}$$

The first term in (1.10), due to one-electron operators, describes the kinetic energy of the electrons and the attractive Coulombic interaction between the electrons and the

nuclei,

$$h_{ii} = -\langle\chi_i|\,\frac{1}{2}\nabla^2\,|\chi_i\rangle + \langle\chi_i|\,v_{\text{ext}}\,|\chi_i\rangle\,. \tag{1.11}$$

where

$$v_{\text{ext}}(\mathbf{r}_i) = -\sum_{A=1}^{N}\frac{Z_A}{|\mathbf{r}_i - \mathbf{R}_{\text{A}}|} \tag{1.12}$$

The second term in (1.10), due to the two-electron operator, has two contributions known as the Coulomb (J) and exchange (K) integrals. The former of these describes the classical repulsive interaction between the electrons and the latter accounts for the avoidance of like-spin electrons due to the Pauli principle. As such, the Coulomb energy is a positive contribution, while exchange lowers the energy as it forces the electrons to avoid each other. These two-electron integrals can be written using the following convenient notation,

$$J_{ij} - K_{ij} = (ii|jj) - (ij|ji) \tag{1.13}$$

where

$$(ij|kl) = \iint \chi_i(\mathbf{x}_1)\chi_j(\mathbf{x}_1)\frac{1}{r_{12}}\chi_k(\mathbf{x}_2)\chi_l(\mathbf{x}_2)\,d\mathbf{x}_1 d\mathbf{x}_2. \tag{1.14}$$

The Hartree-Fock procedure consists of minimising the energy of a Slater determinant with respect to changes in the orbitals, subject to the constraint that the orbitals remain orthonormal. This is done through the use of Lagrange multipliers and gives the Hartree-Fock equations,

$$\hat{F}\chi_i = \sum_j \varepsilon_{ji}\chi_j \tag{1.15}$$

where ε is a matrix of Lagrange multipliers and $\hat{F}$ is the Fock operator,

$$\hat{F} = \hat{h} + \hat{J} - \hat{K}, \tag{1.16}$$

in which the Coulomb and exchange operators are defined as,

$$\hat{J}\chi_j(\mathbf{x}_1) = \sum_i \int \frac{\chi_i(\mathbf{x}_2)\chi_i(\mathbf{x}_2)}{r_{12}}\, d\mathbf{x}_2 \chi_j(\mathbf{x}_1) \tag{1.17}$$

$$\hat{K}\chi_j(\mathbf{x}_1) = \sum_i \int \frac{\chi_i(\mathbf{x}_2)\chi_j(\mathbf{x}_2)}{r_{12}}\, d\mathbf{x}_2 \chi_i(\mathbf{x}_1). \tag{1.18}$$

The Coulomb operator is local, requiring only knowledge of the orbital it is operating on at a particular point in space corresponding to the location of the electron. The exchange operator, requiring a knowledge of the entire orbital at all points in space, is a non-local operator.

The Fock operator is invariant to unitary transformations so the orbitals can be transformed in such a way that ε is diagonal, giving the canonical form of the Hartree-Fock equations,

$$\hat{F}\chi_i' = \varepsilon_i \chi_i' \tag{1.19}$$

where the χ_i' are transformed orbitals. The Hartree-Fock equations are a set of one-electron equations whose eigenvalues ε_i are physically interpreted as orbital energies. The Fock operator is a one-electron Hamiltonian operator. The solutions to the Hartree-Fock equations are found iteratively as, through the electron-electron terms, the Fock operator is defined in terms of the orbitals which are being determined.

For closed shell systems, a restricted formalism is used in which electrons of opposite spin are paired so that they have equivalent spatial components

$$\chi_i(\mathbf{x}) = \begin{cases} \psi_i(\mathbf{r})\alpha(s) \\ \overline{\psi_i}(\mathbf{r})\beta(s) \end{cases}, \tag{1.20}$$

where $\psi_i(\mathbf{r}) = \overline{\psi_i}(\mathbf{r})$. Restricted Hartree-Fock is unable to account for static correlation in stretched H_2 where the limitations placed on the spatial component of the α and β electrons gives rise to the unphysical H^+—H^- electronic configuration. Alternatively, unrestricted Hartree-Fock does not make the assumption that the spatial components of paired electrons must be equal and are instead allowed to differ. The unrestricted treatment of stretched H_2 allows the correct dissociation into two hydrogen atoms, at

the expense of spin contamination. By expanding the unknown wavefunction in a set of known basis functions (see section 1.4) we arrive at the Roothaan-Hall equations.[11,12] In a similar manner to the Roothaan-Hall equations, the unrestricted picture is solved through the Pople-Nesbet equations.[13]

The total Hartree-Fock energy is not simply a sum of orbital energies. The Fock operator has terms describing repulsion to all other electrons via the Coulomb and exchange operators and a sum would double count the electron-electron repulsion. Therefore, the total Hartree-Fock energy is

$$E_{\mathrm{e}} = \sum_{i}^{N} \varepsilon_i - \frac{1}{2} \sum_{ij}^{N} (J_{ij} - K_{ij}). \tag{1.21}$$

The Hartree-Fock procedure determines the lowest energy from a single determinant wavefunction. As the energy is determined as the expectation value of the Hamiltonian, the procedure is variational. Only the exact ground state wavefunction (Ψ_0) will return the exact ground state energy (E_0). Any other choice of wavefunction ($\tilde{\Psi}$) will produce an energy greater than this,

$$\langle \tilde{\Psi} | \, \hat{H} \, | \tilde{\Psi} \rangle \geq \langle \Psi_0 | \, \hat{H} \, | \Psi_0 \rangle = E_0. \tag{1.22}$$

However, for all but one-electron systems, the Hartree-Fock approach is flawed as each electron is treated as being in an average field of all other electrons. The result is that in the Hartree-Fock picture, electrons are permitted to come too close to one another. The Hartree-Fock energy is therefore above the exact energy of the system. To quantify this error the term "correlation energy" is defined as the difference in energy between the Hartree-Fock solution and the exact non-relativistic solution, within the Born-Oppenheimer approximation. The term "correlation energy" can be misleading as, through the exchange terms, like-spin electrons are to some extent correlated. In order to improve upon Hartree-Fock theory, a more accurate wavefunction is required, accounting for the interaction of electrons correctly. The first approach we consider is Configuration Interaction (CI).

1.2 Configuration Interaction

As the Hartree-Fock wavefunction is able to obtain most of the electronic energy, it is a good a starting point and can be systematically improved by the addition of excited state determinants

$$|\Psi_{\mathrm{CI}}\rangle = |\Psi_{\mathrm{HF}}\rangle + \sum_{ia} c_a^i \hat{\tau}_i^a |\Psi_{\mathrm{HF}}\rangle + \sum_{i<j} \sum_{a<b} c_{ab}^{ij} \hat{\tau}_{ij}^{ab} |\Psi_{\mathrm{HF}}\rangle + \cdots . \tag{1.23}$$

The first term is just the regular Hartree-Fock wavefunction and the second and third terms correspond to singly (singles) and doubly (doubles) excited determinants respectively. The excitation operator $\hat{\tau}_i^a$ changes the orbital occupancy of the wavefunction so that an electron that was in an occupied orbital i is now in a virtual orbital a. The coefficients c_a^i are termed the 'amplitudes' and are determined by minimising the CI energy. The double, $\hat{\tau}_{ij}^{ab}$, (and higher) excitation operators behave similarly, but for more electrons. The CI wavefunction may be more conveniently expressed as

$$|\Psi_{\mathrm{CI}}\rangle = (1 + \hat{T}_1 + \hat{T}_2 + \cdots) |\Psi_{\mathrm{HF}}\rangle . \tag{1.24}$$

where

$$\hat{T}_1 = \sum_{ia} c_a^i \hat{\tau}_i^a \tag{1.25}$$

$$\hat{T}_2 = \frac{1}{4} \sum_{ij,ab} c_{ab}^{ij} \hat{\tau}_{ij}^{ab} \tag{1.26}$$

are the excitation operators giving rise to the singly and doubly excited determinants. If all possible excited Slater determinants are included, the full configuration interaction (FCI) limit is achieved, which gives the exact solution within the basis set used. However, even for the smallest systems, the number of terms involved in such an approach is unmanageable. It is therefore necessary to truncate the wavefunction at a reasonable level of excitation.

The inclusion of singles only has no effect on the ground state energy. Solution of the Hartree-Fock eigenvalue problem requires that the off-diagonal elements of the Fock matrix be zero. That is, $\langle \Psi_{\mathrm{HF}}| \hat{H} \hat{\tau}_i^a |\Psi_{\mathrm{HF}}\rangle = 0$, meaning there is no coupling

between the ground and excited state determinants. It is therefore necessary to include at least singles and doubles (CISD) to give some improvement for the ground state energy, which is the point at which the theory is often truncated. The energy is found through a constrained minimisation such that the CI wavefunction remains normalized. However, it is the amplitudes which are optimised, rather than the reference Hartree-Fock wavefunction, to give the lowest energy possible. Therefore, as the orbitals are not affected by the minimisation procedure, the orbitals used in a CI calculation are the equivalent Hartree-Fock orbitals.

When considering relative energies, it is important for the theory being employed to be size extensive. That is, the energy of a system of two non-interacting monomers is equal to the sum of the isolated monomer energies. Although FCI is size extensive, any truncated form is not. This is most usefully illustrated by the example of two non-interacting H_2 molecules. While CISD is able to give all required excitations for a single, isolated hydrogen molecule, when the dimer is considered, it is not able to describe the situation where all four electrons over both molecules are excited. Therefore, this description will not reproduce twice the energy of a single hydrogen molecule. A theory truncated at fourth order (CISDTQ) would be necessary to provide a size-extensive description in this case. This failure of truncated CI theory limits its usefulness and it is therefore beneficial to consider coupled cluster theory (CC), which is size extensive at all levels of truncation.

1.3 Coupled Cluster Theory

In coupled cluster theory, the linear sum of terms which make up the CI wavefunction is replaced by a product,[14–16]

$$|\Psi_{\mathrm{CI}}\rangle = (1 + \sum_{\mu} c_\mu \hat{\tau}_\mu)\,|\Psi_{\mathrm{HF}}\rangle \tag{1.27}$$

$$|\Psi_{\mathrm{CC}}\rangle = \prod_{\mu} (1 + t_\mu \hat{\tau}_\mu)\,|\Psi_{\mathrm{HF}}\rangle \tag{1.28}$$

where μ indicates the number of excitation operations. Expressing the wavefunction in this form means that regardless of truncation, there will be numerous operators

exciting each electron in the system. The form of the CC wavefunction is equal to the Taylor series expansion of the exponential form (as, by definition, $\hat{\tau}_\mu^2 = 0$), allowing the wavefunction to be rewritten as

$$|\Psi_{\mathrm{CC}}\rangle = \exp(t_\mu \hat{\tau}_\mu)\,|\Psi_{\mathrm{HF}}\rangle = e^{\hat{T}}\,|\Psi_{\mathrm{HF}}\rangle \tag{1.29}$$

where the cluster operator

$$\hat{T} = \sum_\mu t_\mu \tau_\mu \tag{1.30}$$

$$= \hat{T}_1 + \hat{T}_2 + \hat{T}_3 + \cdots . \tag{1.31}$$

$\hat{T}_1$ contains all the single excitations, $\hat{T}_2$ contains all the double excitations etc. If the theory is truncated at second order (CCSD), as is common, doubly excited determinants are obtained in two ways. Firstly, through connected doubles, arising from the application of the $\hat{T}_2$ operator and secondly, through disconnected doubles arising from products of the $\hat{T}_1$ operator. Therefore, it is possible—to some extent—for truncated coupled cluster theory to account for higher excitations through disconnected operators. By including these higher order terms, coupled cluster theory ensures size-extensivity. For the previous case of two separated H_2 molecules, CCSD accounts for the independent excitation of both electrons on each molecule through the $\hat{T}_2^2$ operator or equivalent products of single operators.

CCSD represents one of the most commonly used and trusted wavefunction methods. It is possible to systematically improve the description of the wavefunction by inclusion of higher order terms, although beyond CCSD(T),[17] where the triples are considered perturbatively, the expense of the calculations becomes prohibitive for all but small systems. CCSD itself can be too computationally demanding for anything but the smallest systems so it can be common to use an approximation to this theory, known as CC2.[18,19] Throughout this thesis, coupled cluster methods will be used as a reference against which DFT can be compared.

1.4 Basis Sets

To solve the Hartree-Fock equations (1.19), the orbitals in the Slater determinants must be constructed from a finite set of basis functions

$$\psi_i(\mathbf{r}) = \sum_a c_{ai}\eta_a(\mathbf{r}). \tag{1.32}$$

As the set of functions used for this is necessarily finite, it is an approximation to the actual orbital. If an infinite number of functions (a complete basis) were used then this would not represent an approximation. The choice of function type is a balance between similarity to actual electronic structure and computational cost. Slater type orbitals

$$\eta(\mathbf{r}) = Nx^n y^m z^l e^{-\zeta\mathbf{r}} \tag{1.33}$$

reproduce the hydrogenic orbitals but certain necessary integrals can not be solved analytically for this form. Gaussian type orbitals[20]

$$\eta(\mathbf{r}) = Nx^n y^m z^l e^{-\alpha\mathbf{r}^2} \tag{1.34}$$

do not have the correct 'cusp' at the nucleus and drop off too rapidly at large distances, but they are computationally much more favourable than Slater functions. To obtain the correct shape of the wavefunction, more Gaussian-type functions are required. However, despite this drawback, their use is still computationally superior than using Slater-type functions. The form of the basis sets shown here is known as Cartesian, given their dependence on the three Cartesian coordinates x, y and z. For orbitals whose angular momentum is $L \geq 2$, this form requires a greater number of functions than when using spherical harmonics

$$\eta(\mathbf{r}) = Nr^L e^{-\alpha\mathbf{r}^2} Y_L^M(\theta, \phi). \tag{1.35}$$

Therefore, by transforming from Cartesian to the spherical harmonic basis, the calculation requires fewer basis functions and will, as a result, be computationally faster.

The choice of the number of functions, as well as the the function type is important.

A minimal basis set consists of one basis function for each atomic orbital. However, it is useful to have additional functions to be able to describe non-uniform electronic distributions. An atom may be bonded to its nearest neighbours by different types of bonds, each of which may require different functions in order to be described sufficiently well at the same time. Wavefunction-based theories require additional functions of higher angular momentum to be able to accurately describe the electron-electron cusp in the wavefunction.

By expanding (1.19) in (1.32), projecting from the left with a basis function and integrating, we arrive at the Roothaan-Hall equations[11,12]

$$\int \eta_b(\mathbf{r}_1)\hat{F}\sum_a c_{ai}\eta_a(\mathbf{r}_1)\,d\mathbf{r}_1 = \varepsilon_i \int \eta_b(\mathbf{r}_1)\sum_a c_{ai}\eta_a(\mathbf{r}_1)\,d\mathbf{r}_1 \tag{1.36}$$

$$\sum_a c_{ai}\int \eta_b(\mathbf{r}_1)\hat{F}\eta_a(\mathbf{r}_1)\,d\mathbf{r}_1 = \varepsilon_i \sum_a c_{ai}\int \eta_b(\mathbf{r}_1)\eta_a(\mathbf{r}_1)\,d\mathbf{r}_1 \tag{1.37}$$

$$\mathbf{Fc} = \mathbf{Sc}\varepsilon \tag{1.38}$$

where $\mathbf{S}$ is the overlap matrix

$$S_{ij} = \int \eta_i(\mathbf{r})\eta_j(\mathbf{r})\,d\mathbf{r}. \tag{1.39}$$

Chapter 2

Density Functional Theory

The electron density is obtained from a multiple integral of the square of the modulus of the wavefunction

$$\rho(\mathbf{r}_1) = N \int \cdots \int |\Psi(\mathbf{x}_1, \mathbf{x}_2, \ldots, \mathbf{x}_N)|^2 \, ds_1 d\mathbf{x}_2 \cdots d\mathbf{x}_N, \tag{2.1}$$

where only the spatial part of the first electron is omitted from the integration. Due to the indistinguishability of electrons, $\rho(\mathbf{r}_1)d\mathbf{r}_1$ represents the chance of finding any electron in the volume element $d\mathbf{r}_1$. Before considering a formal proof for the validity of the electron density as a quantity for calculating the electronic energy its use can be justified from the following arguments: The electron density integrates to give the number of electrons in a system

$$\int \rho(\mathbf{r}) d\mathbf{r} = N, \tag{2.2}$$

and it also exhibits cusps at the nuclei, whose slope is directly related to the atomic charge. Therefore, the electron density contains complete information on the number of electrons, as well as the charge and positions of the nuclei. As noted by Bright-Wilson,[21] this is all that is required to construct the electronic Hamiltonian of equation (1.5).

The motivation for using the electron density rather than the wavefunction lies in its simplicity. The wavefunction depends on four coordinates (three spatial and one spin) for each electron. As the size of a system increases, the complexity quickly becomes unmanageable. However, as a function of only four coordinates in total, the electron

density is much more appealing. In fact, its appeal is so great that early attempts at using it as a basis for a theory of electronic structure were made before any proof that this was possible had been provided. Thomas-Fermi-Dirac[22–25] theory constructs the energy from components which can be expressed in terms of the density

$$E_{\mathrm{TFD}} = C_{\mathrm{T}} \int \rho^{\frac{5}{3}}(\mathbf{r}) d\mathbf{r} + E_{\mathrm{Ne}} + J + C_{\mathrm{X}} \int \rho^{\frac{4}{3}}(\mathbf{r}) d\mathbf{r}, \tag{2.3}$$

where E_{Ne} is the nuclear-electron energy. The electron-electron energy V_{ee} is approximated as the classical Coulomb interaction, J plus exchange. The first and last terms are the kinetic and exchange energy terms which are the exact results for the uniform electron gas, but here applied locally. The approximation for the kinetic energy in TFD theory is so poor that it fails to even bind molecular systems. The terms in the TFD energy expression will be elaborated upon later in this chapter.

2.1 The Hohenberg-Kohn Theorems

To verify the suitability of the electron density as a quantity for determining the electronic energy, it is necessary to show that the density uniquely determines the Hamiltonian for that system. This is the motivation behind the first Hohenberg-Kohn theorem.[26] Consider two Hamiltonians, $\hat{H}_1$ and $\hat{H}_2$ whose external potentials differ by more than a trivial additive constant but which have ground state wavefunctions Ψ_1 and Ψ_2 respectively, both of which have the same density. Both wavefunctions must therefore correspond to systems with the same number of electrons.

We know that the expectation value of a Hamiltonian with the exact wavefunction gives the energy of that system. If any other wavefunction is used, the variational principle states that the energy that results will be higher than when the exact wavefunction is used,

$$E_1 = \langle \Psi_1 | \hat{H}_1 | \Psi_1 \rangle \tag{2.4}$$

$$E_1 < \langle \Psi_2 | \hat{H}_1 | \Psi_2 \rangle . \tag{2.5}$$

Using the simple identity $\hat{H}_1 = \hat{H}_2 + [\hat{H}_1 - \hat{H}_2]$, we have

$$E_1 < \langle \Psi_2 | \hat{H}_1 | \Psi_2 \rangle = \langle \Psi_2 | \hat{H}_2 | \Psi_2 \rangle + \langle \Psi_2 | [\hat{H}_1 - \hat{H}_2] | \Psi_2 \rangle . \tag{2.6}$$

As the kinetic and electron-electron energy terms are defined only by the number of electrons, the Hamiltonians only differ in the external potentials v_1 and v_2(equation (1.12)). Exchanging the labels in equation (2.6) leads to the following two results,

$$E_1 < E_2 + \int \rho(\mathbf{r})[v_1(\mathbf{r}) - v_2(\mathbf{r})]\, d\mathbf{r} \tag{2.7}$$

$$E_2 < E_1 + \int \rho(\mathbf{r})[v_2(\mathbf{r}) - v_1(\mathbf{r})]\, d\mathbf{r} \tag{2.8}$$

giving the following contradiction

$$E_1 + E_2 < E_2 + E_1. \tag{2.9}$$

Through this proof by *reductio ad absurdum*, it has been shown that two potentials, which differ by more than an additive constant, can not lead to the same electron density. Thus, the density uniquely determines the Hamiltonian and it can be used to calculate the energy. It is therefore possible to construct the energy in terms of functionals of the density,

$$E[\rho] = T[\rho] + V_{\mathrm{Ne}}[\rho] + V_{\mathrm{ee}}[\rho] \tag{2.10}$$

where the terms relate to the kinetic energy of the electrons, the nuclear-electron and electron-electron potentials, respectively. It is usual to collect the kinetic energy and the electron-electron terms together into one functional, $F[\rho(\mathbf{r})]$,

$$E[\rho] = \int \rho(\mathbf{r}) v(\mathbf{r}) d\mathbf{r} + F[\rho]. \tag{2.11}$$

The second Hohenberg-Kohn theorem concerns the introduction of a variational principle based on the density. As shown by the first theorem, any density ρ will uniquely determine the Hamiltonian, which is equivalent to determining the external potential, v, and therefore its own wavefunction Ψ. By using a trial wavefunction $\tilde{\Psi}$

which gives density $\tilde{\rho}$, we see that

$$\langle \tilde{\Psi} | \hat{H} | \tilde{\Psi} \rangle = \int \tilde{\rho}(\mathbf{r}) v(\mathbf{r}) d\mathbf{r} + F[\tilde{\rho}] = E[\tilde{\rho}] \geq E[\rho]. \tag{2.12}$$

In an analogous manner to the Hartree-Fock energy minimisation, the energy can therefore be minimised with respect to variations in the density. However, the variations must be constrained to those that maintain the number of electrons in the system through equation (2.2). Again, this is achieved through the use of a Lagrange multiplier. Minimising the energy subject to the necessary constraint and then substituting in the energy expression of equation (2.11) gives the Euler equation

$$\begin{aligned} \frac{\delta}{\delta\rho(\mathbf{r})} \left(E[\rho] - \mu \left[\int \rho(\mathbf{r}) d\mathbf{r} - N \right] \right) &= 0 \\ \frac{\delta E[\rho]}{\delta\rho(\mathbf{r})} - \mu &= 0 \\ v(\mathbf{r}) + \frac{\delta F[\rho]}{\delta\rho(\mathbf{r})} &= \mu \\ v(\mathbf{r}) + \frac{\delta V_{\mathrm{ee}}[\rho]}{\delta\rho(\mathbf{r})} + \frac{\delta T[\rho]}{\delta\rho(\mathbf{r})} &= \mu. \end{aligned} \tag{2.13}$$

We have therefore arrived at a position where we can express the electronic energy in terms of the density through the use of the functional $F[\rho]$ and we can minimise this energy variationally. However, there is no indication of the form of this unknown functional, so although we know that obtaining the energy is a possibility, at this point there is no procedure for doing it.

2.2 The Levy constrained search

The density in the Hohenberg-Kohn analysis must be obtained from a valid antisymmetric ground state wavefunction associated with a Hamiltonian of the form in equation (1.5). This condition is known as v-representability. The conditions for v-representability are not known and it is possible to obtain physically reasonable trial densities which are non-v-representable.[27] The Levy constrained search[28,29] removes the need to consider v-representable densities by minimising over N-representable densities—those that are obtained from N-electron wavefunctions. The exact energy is the result of the min-

imisation of the expectation value of the N-electron Hamiltonian over all N-electron wavefunctions

$$E_0 = \min_{\Psi} \langle \Psi | \, \hat{T} + \hat{V}_{\mathrm{ee}} + \sum_{i}^{N} v(\mathbf{r}_i) \, | \Psi \rangle \tag{2.14}$$

This minimisation can be done in two parts: firstly minimising over all wavefunctions yielding one particular N-representable density, followed by minimisation over all N-representable densities

$$E_0 = \min_{\rho} \left(\min_{\Psi \to \rho} \langle \Psi | \, \hat{T} + \hat{V}_{\mathrm{ee}} + \sum_{i}^{N} v(\mathbf{r}_i) \, | \Psi \rangle \right). \tag{2.15}$$

The external potential is only dependent upon the density and can therefore be omitted from the minimisation over wavefunctions to give

$$E_0 = \min_{\rho} \left(\min_{\Psi \to \rho} \langle \Psi | \, \hat{T} + \hat{V}_{\mathrm{ee}} \, | \Psi \rangle + \int v(\mathbf{r}) \rho(\mathbf{r}) d\mathbf{r} \right). \tag{2.16}$$

It is now possible to extend the definition of $F[\rho]$ in equation (2.11) to

$$F[\rho] = \min_{\Psi \to \rho} \langle \Psi | \, \hat{T} + \hat{V}_{\mathrm{ee}} \, | \Psi \rangle \, . \tag{2.17}$$

The minimisation of the energy now only needs to be considered for N-representable densities, the conditions for which are known: the density should integrate to the number of electrons, be everywhere positive and satisfy $\int |\nabla \rho^{1/2}|^2 \, d\mathbf{r} < \infty$ for finite systems. However, the form of the function $F[\rho]$ is still unknown.

2.3 Kohn-Sham Theory

The precise form of the quantity $F[\rho(\mathbf{r})]$ introduced in the last section is unknown. However, specific parts of the energy are known. Kohn-Sham (KS) theory[30] therefore adopts a philosophy of collecting all known terms and all unknown terms, and making the former as large as possible, to minimise the size of the latter. Therefore, if and when approximations are introduced to calculate the unknown parts of the functional, any errors will have as small an effect on the energy as possible.

If we consider a fictitious system of non-interacting electrons it is possible to write the kinetic energy in terms of one-electron orbitals as

$$T_{\mathrm{S}}[\rho] = \sum_i \langle \psi_i(\mathbf{r}) | -\frac{1}{2}\nabla^2 | \psi_i(\mathbf{r}) \rangle \tag{2.18}$$

and the density as

$$\rho(\mathbf{r}) = \sum_i^N |\psi_i(\mathbf{r})|^2. \tag{2.19}$$

In the KS scheme T_{S} is used to approximate the kinetic energy of the real, fully interacting system.

A large part of the electron-electron repulsion energy can be obtained from the classical Coulomb repulsion of the density

$$J[\rho] = \frac{1}{2}\iint \frac{\rho(\mathbf{r}_1)\rho(\mathbf{r}_2)}{\mathbf{r}_{12}} d\mathbf{r}_1 d\mathbf{r}_2. \tag{2.20}$$

We now define a new term, the exchange-correlation energy functional, which is the difference between the kinetic energies of the real, interacting system and that of the fictitious, non-interacting system together with the difference between the V_{ee} of the real system and the Coulomb energy

$$E_{\mathrm{XC}}[\rho] = T[\rho] - T_{\mathrm{S}}[\rho] + V_{\mathrm{ee}}[\rho] - J[\rho], \tag{2.21}$$

which allows us to express the energy as

$$E[\rho] = \int \rho(\mathbf{r}) v(\mathbf{r}) d\mathbf{r} + T_{\mathrm{S}}[\rho] + J[\rho] + E_{\mathrm{XC}}[\rho]. \tag{2.22}$$

The first three terms can all be written down exactly, while all approximations are now contained within the final term, the exchange-correlation energy.

Minimising the energy of equation (2.22) with respect to changes in the density, subject to the constraint that the number of electrons remains constant, gives the Euler

equation,

$$v(\mathbf{r}) + \frac{\delta T_{\mathrm{S}}[\rho]}{\delta\rho(\mathbf{r})} + \frac{\delta J[\rho]}{\delta\rho(\mathbf{r})} + \frac{\delta E_{\mathrm{XC}}[\rho]}{\delta\rho(\mathbf{r})} = \mu \tag{2.23}$$

which we write as

$$v_{\mathrm{eff}}(\mathbf{r}) + \frac{\delta T_{\mathrm{S}}[\rho]}{\delta\rho(\mathbf{r})} = \mu \tag{2.24}$$

where

$$v_{\mathrm{eff}}(\mathbf{r}) = v(\mathbf{r}) + \frac{\delta J[\rho]}{\delta\rho(\mathbf{r})} + \frac{\delta E_{\mathrm{XC}}[\rho]}{\delta\rho(\mathbf{r})}. \tag{2.25}$$

Equation (2.24)—which yields the exact density of the real system—is the same Euler equation as in equation (2.13) for a system of non-interacting electrons moving in an external potential, $v_{\mathrm{eff}}(\mathbf{r})$ (that is to say, a system of electrons for which $T = T_{\mathrm{S}}$ and $V_{\mathrm{ee}} = 0$). It follows that the density of the real system can be obtained by determining the density of a non-interacting system moving in an effective potential, $v_{\mathrm{eff}}(\mathbf{r})$. This can be done exactly as the Hamiltonian is uncoupled,

$$\hat{H} = -\sum_{i}^{N} \frac{1}{2}\nabla_i^2 + \sum_{i}^{N} v_{\mathrm{eff}}(\mathbf{r}_i) \tag{2.26}$$

and so the exact solution is just a single determinant of orbitals obtained from a set of one-electron equations

$$\left(-\frac{1}{2}\nabla^2 + v_{\mathrm{eff}}(\mathbf{r})\right)\psi_i(\mathbf{r}) = \varepsilon_i\psi_i(\mathbf{r}). \tag{2.27}$$

These orbitals can then be used to determine T_{S} (equation (2.18)) and the density (equation (2.19)). The energy is then evaluated using equation (2.22). Through the introduction of orbitals, it has been possible to derive the exact form for most of $F[\rho]$. However, the form of the exchange-correlation functional remains unknown. Kohn-Sham theory is exact; the exact form of the exchange-correlation functional would allow the calculation of the exact electronic energy. Understandably, the principal focus of research in DFT is on developing new exchange-correlation functionals, while assessing and understanding

the strengths and weaknesses of existing forms. It is therefore common to refer to any particular form of the exchange-correlation functional simply as a "functional".

2.4 Exchange-Correlation Functionals

As seen in the attempts of Thomas, Fermi and Dirac, the uniform electron gas (UEG) can be used as a basis for theories employing the electron density as the principal quantity. The development of exchange-correlation functionals will be considered with this as a starting point. The UEG is a system of infinite volume, with an infinite number of electrons balanced by a background positive charge. Applying the UEG result locally yields

$$E_{\mathrm{X}}^{\mathrm{LDA}}[\rho] = -\frac{3}{4}\left(\frac{3}{\pi}\right)^{\frac{1}{3}} \int \rho^{\frac{4}{3}}(\mathbf{r})\, d\mathbf{r}. \tag{2.28}$$

In order to develop a corresponding functional of the density for the correlation energy of a UEG, Ceperly and Alder[31] performed quantum Monte-Carlo simulations on the UEG. Their results have been parameterised into several forms, most notably by Vosko, Wilk and Nusair (VWN).[32] The molecular application of the UEG exact expression for the exchange energy, $E_{\mathrm{X}}^{\mathrm{LDA}}$, and the essentially exact UEG correlation energy, $E_{\mathrm{C}}^{\mathrm{LDA}}$, gives the local density approximation (LDA). It is useful when applied in Physics to problems involving bulk metallic systems whose structure resembles that of a uniform gas of electrons. However, in Chemistry, this model is not as relevant for molecules where electron density is more localised and it generally overbinds molecular systems.

In order to improve upon the UEG model, higher order density-dependent terms are introduced. Information about the gradient of the density will take some account of the variation of the electron density within a molecule. The generalised gradient approximation (GGA) takes as the form of the exchange-correlation functional

$$E_{\mathrm{XC}}[\rho] = \int F(\rho(\mathbf{r}), \nabla\rho(\mathbf{r}))\, d\mathbf{r}. \tag{2.29}$$

Functionals such as those due to Perdew, Burke and Ernzerhof (PBE)[33] and Perdew and Wang[34,35] are designed to satisfy conditions of the exact E_{XC} under various limits. More

success in chemistry has been found by fitting the functional form to known molecular properties. However, functionals derived from this approach are susceptible to problems when applied to cases outside of the type included in the set of molecules used for the fitting procedure. Becke used atomic properties to fit a gradient correction to $E_{\mathrm{X}}^{\mathrm{LDA}}$ in his 1988 exchange functional (B88X).[36] He subsequently incorporated a gradient corrected correlation functional developed by Perdew and Wang.[34] Similarly, the BLYP GGA functional is a combination of B88X and the gradient corrected correlation functional of Lee, Yang and Parr (LYP).[37]

Hybrid functionals augment the functional form of GGAs with a proportion of exact exchange as defined in Hartree-Fock, evaluated using Kohn-Sham orbitals (see the final term of equation (1.9)). The justification for this can be seen through a consideration of the adiabatic connection.[38–42] This involves the connection between the Kohn-Sham non-interacting reference system and the fully interacting real system. The Levy constrained search functional

$$F[\rho] = \min_{\Psi \to \rho} \langle \Psi | \, \hat{T} + \hat{V}_{\mathrm{ee}} \, | \Psi \rangle \,, \tag{2.30}$$

can be re-written with the electron-electron operator scaled by a parameter λ which connects the non-interacting Kohn-Sham system ($\lambda = 0$) to the fully interacting, real system ($\lambda = 1$). The Hamiltonian

$$\hat{H}_{\lambda} = \hat{T} + \hat{V}^{\lambda} + \lambda \hat{V}_{\mathrm{ee}} \tag{2.31}$$

has its density fixed at that of the interacting system through the choice of the external potential, $\hat{V}^{\lambda}$. Equation (2.30) is then generalised to

$$F_{\lambda}[\rho] = \min_{\Psi \to \rho} \langle \Psi | \, \hat{T} + \lambda \hat{V}_{\mathrm{ee}} \, | \Psi \rangle = \langle \Psi_{\lambda} | \, \hat{T} + \lambda \hat{V}_{\mathrm{ee}} \, | \Psi_{\lambda} \rangle \,. \tag{2.32}$$

It is known that for the non-interacting ($\lambda = 0$) and the fully interacting ($\lambda = 1$) systems

$$F_0[\rho] = T_{\mathrm{S}}[\rho] \tag{2.33}$$

$$F_1[\rho] = T[\rho] + V_{\mathrm{ee}}[\rho], \tag{2.34}$$

respectively. This allows the expression of the exchange-correlation energy in equation (2.21) as

$$E_{\mathrm{XC}}[\rho] = F_1[\rho] - F_0[\rho] - J[\rho] = \int_0^1 \frac{\partial F_\lambda[\rho]}{\partial \lambda}\, d\lambda - J[\rho]. \tag{2.35}$$

Employing the Hellmann-Feynman theorem,[43,44] this becomes

$$E_{\mathrm{XC}}[\rho] = \int_0^1 \langle \Psi_\lambda | \hat{V}_{\mathrm{ee}} | \Psi_\lambda \rangle \; d\lambda - J[\rho] \tag{2.36}$$

It is therefore possible to write the exchange-correlation energy exactly as

$$E_{\mathrm{XC}}[\rho] = \int_0^1 W_\lambda \, d\lambda \tag{2.37}$$

where

$$W_\lambda = \langle \Psi_\lambda | \hat{V}_{\mathrm{ee}} | \Psi_\lambda \rangle - J[\rho]. \tag{2.38}$$

It is clear that the exact form of W_λ would yield the exact exchange-correlation energy through a simple integration. An accurate description of W_λ is therefore highly desirable. Becke approximated the form as $W_\lambda = a + b\lambda$[45] and used the exact conditions for W_0 and W_1 to determine the values of a and b. Firstly, for $\lambda = 0$,

$$W_0 = a = \langle \Psi_0 | \hat{V}_{\mathrm{ee}} | \Psi_0 \rangle - J[\rho] = E_{\mathrm{X}} \tag{2.39}$$

which is the value of exact orbital exchange evaluated using the KS orbitals. For $\lambda = 1$,

$$W_1 = a + b = \langle \Psi_1 | \hat{V}_{\mathrm{ee}} | \Psi_1 \rangle - J = V_{\mathrm{ee}} - J. \tag{2.40}$$

This was approximated as $U_{\mathrm{XC}}^{\mathrm{LDA}}$, which is the potential energy of exchange-correlation taken from the LDA. Integrating Becke's approximation to the adiabatic connection then gives

$$E_{\mathrm{XC}} = \frac{1}{2} E_{\mathrm{X}} + \frac{1}{2} U_{\mathrm{XC}}^{\mathrm{LDA}}. \tag{2.41}$$

This is known as Becke's "half and half" functional, which shows that the incorpora-

tion of some amount of exact exchange into exchange-correlation functionals is often desirable. Such functionals are known as hybrid functionals. There are numerous hybrid functionals in the literature. By combining the result of equation (2.41) with the correlation functional LYP, the BH-HLYP functional is obtained. The functional with the most widespread use is B3LYP[46] whose ubiquitous presence is a result of it being embraced by the chemical community for its generally good, all-round performance. The functional includes exchange and correlation terms based on the density as well as gradient corrections for both, but also a portion of exact exchange. The most commonly used form, due to Stephens *et al.*[47] is

$$E_{\mathrm{XC}} = (1 - a_0)E_{\mathrm{X}}^{\mathrm{LDA}} + a_0 E_{\mathrm{X}} + a_{\mathrm{X}}\Delta E_{\mathrm{X}}^{B88} + a_{\mathrm{C}}E_{\mathrm{C}}^{\mathrm{VWN}} + (1 - a_{\mathrm{C}})\Delta E_{\mathrm{C}}^{\mathrm{LYP}}. \qquad (2.42)$$

The local terms for exchange and correlation come from the LDA. Becke's 1988 gradient correction is used for the exchange and the correlation is gradient corrected as in the work of Lee, Yang and Parr. The value of a_0 is set to 0.2 so the functional contains 20% exact exchange. Other common hybrid exchange-correlation functionals include the PBE0 functional[48,49] and the B97-1 functional[50,51] which incorporate 25% and 21% exact exchange, respectively.

2.5 Theory of particular relevance to this work

Remaining relevant background theory will be discussed throughout the thesis when it is most pertinent for it to be considered. However, there are certain aspects of modern DFT which require a detailed outlining prior to any further discussion, given their relevance to the majority of the work. Firstly, the discussion will be of long-range corrected functionals, and the specific case of CAM-B3LYP[52] whose performance is central to this thesis. Secondly, an outline of the theory of time-dependent density functional theory (TDDFT) and its application to the determination of excited states is given. This is followed by an examination of the failure and correction of TDDFT results, which is also of central importance to this thesis. Each section involves a discussion of the initial theory, its shortcomings, the improvements that have been made and finally, how they relate to the work that will be presented.

2.5.1 Long-range corrected functionals

Hybrid functionals, particularly B3LYP, have become hugely popular for determining a wide range of chemical properties. However, their performance suffers in cases where the inter-electron distance becomes large. The most pertinent of these failures is in the description of charge-transfer (CT) excitation energies (see section 2.5.2). The long-range problem can be traced to insufficient exact exchange at large r_{12}. To improve this situation, the electron-electron term can be split as[53,54]

$$\frac{1}{r_{12}} = \frac{1-\mathrm{erf}(\mu r_{12})}{r_{12}} + \frac{\mathrm{erf}(\mu r_{12})}{r_{12}}. \tag{2.43}$$

Through this, it is possible to treat the long-range and short-range exchange in different ways. The first term in equation (2.43) accounts for the short-range part and is treated using DFT exchange. This is appropriate given the generally acceptable performance of DFT functionals for short-range dependent properties. The form of the exchange for this part is based on the 1-particle density matrix

$$E_{\mathrm{X}}[\rho] = -\frac{1}{4}\iint \frac{1}{r_{12}}\rho_1^2(\mathbf{r}_1,\mathbf{r}_2)d\mathbf{r}_1 d\mathbf{r}_2. \tag{2.44}$$

By assuming the LDA, this can be expressed more conveniently in terms of the density[53,55,56]

$$E_{\mathrm{X}}^{\mathrm{LDA}} = -\sum_{\sigma}\frac{1}{2}K_{\sigma}^{\mathrm{LDA}}\int \rho_{\sigma}^{\frac{4}{3}}(\mathbf{r})d\mathbf{r} \tag{2.45}$$

where $K_{\sigma}^{\mathrm{LDA}} = 2(3/\pi)^{\frac{1}{3}}3/4$, which may be related to the Fermi momentum,

$$k_{\sigma}^{\mathrm{LDA}} = \left(\frac{9\pi}{K_{\sigma}^{\mathrm{LDA}}}\right)^{\frac{1}{2}}\rho_{\sigma}^{\frac{1}{3}}. \tag{2.46}$$

The expression for the exchange energy (equation (2.45)) has been extended to allow for the use of GGA exchange functionals[57,58] by assuming that the one particle GGA density matrix can be obtained by evaluating the LDA matrix with the modified momentum

$$k_{\sigma}^{\mathrm{GGA}} = \left(\frac{9\pi}{K_{\sigma}^{\mathrm{GGA}}}\right)^{\frac{1}{2}}\rho_{\sigma}^{\frac{1}{3}}. \tag{2.47}$$

The second term of equation (2.43) concerns the long-range interaction and is treated through exact orbital exchange.

$$E_{\mathrm{X}}^{\mathrm{LR}} = -\frac{1}{2}\sum_{i,j}\psi_i(\mathbf{r}_1)\psi_j(\mathbf{r}_2)\frac{\mathrm{erf}(\mu r_{12})}{r_{12}}\psi_j(\mathbf{r}_1)\psi_i(\mathbf{r}_2)\,d\mathbf{r}_1\,d\mathbf{r}_2. \tag{2.48}$$

The parameter μ determines the rate at which the treatment of exchange 'switches' between short-range DFT exchange and long-range exact orbital exchange. Consequently, a value of $\mu = 0$ would give no exact exchange, resulting in a pure GGA functional. Conversely, $\mu = \infty$ would give a Hartree-Fock treatment of exchange at all distances. Tawada *et al.*[58] determined a value of $\mu = 0.33$ a_0^{-1}. The resulting approach was successful in the treatment of van der Waals interactions,[59] charge-transfer excitations[58] and polarizabilities in extended π-systems.[57] However, the performance of functionals based on this long-range correction is poor for properties such as atomisation energies, which were treated well with conventional hybrid functionals. This can be traced to the treatment of exact exchange within the long-range correction. The parameter μ controls the proportion of exact exchange by taking values between zero and one as the inter-electron distance increases. The result is a short-range region where there is little or no exact exchange incorporated into the calculation. In this case, the performance of the functional will reflect that of a pure GGA, rather than a hybrid functional. The benefits exhibited by functionals such as B3LYP as a result of adding exact exchange have been lost.

CAM-B3LYP

To resolve the issue with inappropriate amounts of exact exchange at short and long distance, Yanai *et al.*[52] introduced additional parameters to the partitioning in (2.43) to increase the flexibility of the exchange term,

$$\frac{1}{r_{12}} = \frac{1-[\alpha+\beta\mathrm{erf}(\mu r_{12})]}{r_{12}} + \frac{\alpha+\beta\mathrm{erf}(\mu r_{12})}{r_{12}}. \tag{2.49}$$

The authors named this approach as the "Coulomb-attenuating method" and outlined the details for a version of B3LYP called CAM-B3LYP. For this functional, the short-

range exchange is governed by the first term in equation (2.49) and has the form,

$$E_{\mathrm{X}}^{\mathrm{SR}} = -\frac{1}{2}\sum_{\sigma}\int \rho_{\sigma}^{\frac{4}{3}}(\mathbf{r})K_{\sigma}^{\mathrm{GGA}} \times \left[(1-\alpha) - \beta\left(\frac{8}{3}a_{\sigma}[\sqrt{\pi}\mathrm{erf}\left(\frac{1}{2a_{\sigma}}\right) + 2a_{\sigma}(b_{\sigma} - c_{\sigma})]\right)\right] \tag{2.50}$$

where

$$a_{\sigma} = \frac{\mu}{2k_{\sigma}^{\mathrm{GGA}}} \tag{2.51}$$

$$b_{\sigma} = \exp\left(-\frac{1}{4a_{\sigma}^2}\right) \tag{2.52}$$

$$c_{\sigma} = 2a_{\sigma}^2 b_{\sigma} + \frac{1}{2} \tag{2.53}$$

and $K_{\sigma}^{\mathrm{GGA}}$ is defined as in the Becke 1988 gradient corrected exchange functional,

$$K_{\sigma}^{\mathrm{GGA}} = K_{\sigma}^{\mathrm{LDA}} + \frac{2\beta_B x_{\sigma}^2}{1 + 6\beta_B x_{\sigma}\mathrm{arcsinh}x_{\sigma}} \tag{2.54}$$

where $\beta_B = 0.0042$.

Correspondingly, the long-range exchange is governed by the second term in equation (2.49) and has the form

$$E_{\mathrm{X}}^{\mathrm{LR}} = \alpha E_{\mathrm{X}} - \frac{\beta}{2}\sum_{\sigma}\sum_{ij}\phi_i(\mathbf{r}_1)\phi_j(\mathbf{r}_2)\frac{\mathrm{erf}(\mu r_{12})}{r_{12}}\phi_j(\mathbf{r}_1)\phi_i(\mathbf{r}_2)\, d\mathbf{r}_1\, d\mathbf{r}_2. \tag{2.55}$$

The authors found that using the same μ value as Tawada *et al.* and values of $\alpha = 0.19$ and $\beta = 0.46$ gave atomisation energies, ionization potentials and total atomic energies in good agreement with B3LYP. They also found that the performance for charge-transfer excitations was greatly improved compared to B3LYP.

2.5.2 Time-dependent density functional theory (TDDFT)

Given the reliance on the variational principle, DFT cannot be applied to arbitrary electronic states. It is only valid to apply it to the lowest state of a particular space-spin symmetry. The development of time-dependent density functional theory (TDDFT) has allowed such excited states to be probed. Through the linear response formalism, which is outlined below, it is possible to determine vertical electronic excitation energies from

the ground state to any excited state—the difference between the energies of the excited state surface and the ground state surface, at a given geometry. Following an outline of the theory, a discussion of failures within TDDFT will be given, along with potential solutions.

In a similar fashion to the treatment by Hohenberg and Kohn, the Runge-Gross theorem[60] establishes the basis of a time-dependent density functional theory (TDDFT) by considering a time-dependent non-interacting reference system whose electron density exactly matches that of the real, interacting system. Analogous to the first and second Hohenberg-Kohn theorems, the time-dependent density determines the time-dependent external potential and a variational principle can be established. To derive an expression for the excitation energy, we can start from the time-dependent Kohn-Sham (TDKS) equations

$$i\frac{\partial}{\partial t}\psi_i(\mathbf{r},t) = \hat{F}\psi_i(\mathbf{r},t) \tag{2.56}$$

where $\hat{F}^{\mathrm{KS}}$ is the time-dependent KS operator. Although TDKS theory is formally exact, the form of the time-dependent exchange-correlation functional is unknown. The adiabatic local density approximation,[61–63] based on the assumption that the density varies only slowly with time, allows us to use the time-independent ground state exchange-correlation functional rather than a time-dependent one.

The formulation of TDDFT with which we will be concerned is based on linear-response theory.[62–65] The response of the ground state density to a time-dependent electric field will give the excitation energies. By expanding the time-dependent Kohn-Sham equations in a basis of time-independent single-particle wavefunctions we have

$$\sum_q F_{pq}P_{qr} - P_{pq}F_{qr} = i\frac{\partial}{\partial t}P_{pr} \tag{2.57}$$

where F_{pq} and P_{pq} are the KS operator matrix and the density matrix, respectively and the indices $p, q \ldots$ denote general orbitals. Note that if we were to consider the ground state, which does not vary with time, the left hand side of equation (2.57) would be equal to zero.

An oscillating, time-dependent electric field is applied to the system causing a per-

turbation

$$P_{pq} = P^0_{pq} + P^1_{pq} \tag{2.58}$$

$$F_{pq} = F^0_{pq} + F^1_{pq}. \tag{2.59}$$

The perturbation to the KS Hamiltonian consists of two terms

$$F^1_{pq} = g_{pq} + \Delta F^0_{pq}. \tag{2.60}$$

The first of these corresponds to the applied perturbation, the time-dependent electric field of frequency ω

$$g_{pq} = \frac{1}{2}(f_{pq}e^{-i\omega t} + f^*_{pq}e^{i\omega t}) \tag{2.61}$$

where the one-electron operator f_{pq} describes the applied perturbation. The second term,

$$\Delta F^0_{pq} = \sum_{st} \frac{\partial F^0_{pq}}{\partial P_{st}} P^1_{st}, \tag{2.62}$$

gives the change in the KS operator due to the change in the density. The perturbation to the density matrix is written in terms of perturbation densities, d_{pq}, as

$$P^1_{pq} = \frac{1}{2}[d_{pq}e^{-i\omega t} + d^*_{qp}e^{i\omega t}]. \tag{2.63}$$

Inserting equations (2.58) and (2.59) into equation (2.57) and considering only the first-order perturbation on the TDKS equation (2.57) we have

$$\sum_q (F^0_{pq}P^1_{qr} - P^1_{pq}F^0_{qr} + F^1_{pq}P^0_{qr} - P^0_{pq}F^1_{qr}) = i\frac{\partial}{\partial t}P^1_{pr}. \tag{2.64}$$

Inserting equations (2.60) and (2.63) into (2.64) gives

$$\sum_q \left[F^0_{pq}d_{qr} - d_{pq}F^0_{qr} + \left(f_{pq} + \sum_{st} \frac{\partial F^0_{pq}}{\partial P_{st}} d_{st} \right) P^0_{qr} - P^0_{pq} \left(f_{qr} + \sum_{st} \frac{\partial F^0_{qr}}{\partial P_{st}} d_{st} \right) \right] = \omega d_{pr}. \tag{2.65}$$

Terms multiplied by $e^{i\omega t}$ give the complex conjugate of equation (2.65). The idempotency condition

$$\sum_q (P^0_{pq}P^1_{qr} + P^1_{pq}P^0_{qr}) = P^1_{pr} \tag{2.66}$$

restricts the form of d_{pq} such that only occupied-virtual and virtual-occupied pairs are non-zero. The unperturbed Fock matrix is diagonal, so only occupied-occupied and virtual-virtual pairs will contribute. If we set $x_{ai} = d_{ai}$ and $y_{ai} = d_{ia}$, where *a,b,c...* and *i,j,k...* denote unoccupied and occupied orbitals respectively, we obtain the following pair of equations,

$$F^0_{aa}x_{ai} - x_{ai}F^0_{ii} + \left[f_{ai} + \sum_{bj}\left(\frac{\partial F_{ai}}{\partial P_{bj}}x_{bj} + \frac{\partial F_{ai}}{\partial P_{jb}}y_{bj}\right)\right]P^0_{ii} = \omega x_{ai} \tag{2.67}$$

$$F^0_{ii}y_{ai} - y_{ai}F^0_{aa} - P^0_{ii}\left[f_{ia} + \sum_{bj}\left(\frac{\partial F_{ia}}{\partial P_{bj}}x_{bj} + \frac{\partial F_{ia}}{\partial P_{jb}}y_{bj}\right)\right] = \omega y_{ai} \tag{2.68}$$

The elements of the time-dependent Kohn-Sham matrix are given by

$$F_{pq} = \int \psi_p(\mathbf{r})\hat{F}\psi_q(\mathbf{r})d\mathbf{r} \tag{2.69}$$

$$= \int \psi_p(\mathbf{r})\left(-\frac{1}{2}\nabla^2 + v_{\text{ext}}(\mathbf{r}) + \int \frac{\rho(\mathbf{r}')}{|\mathbf{r}-\mathbf{r}'|}d\mathbf{r}' + \frac{\delta E_{\text{XC}}[\rho(\mathbf{r})]}{\delta\rho(\mathbf{r})}\right)\psi_q(\mathbf{r})d\mathbf{r}. \tag{2.70}$$

Given that

$$\frac{\partial\rho(\mathbf{r}')}{\partial P_{rs}} = \psi_r(\mathbf{r}')\psi_s(\mathbf{r}') \tag{2.71}$$

it follows that

$$\frac{\partial F_{pq}}{\partial P_{rs}} = \iint \frac{1}{|\mathbf{r}-\mathbf{r}'|}\psi_p(\mathbf{r})\psi_q(\mathbf{r})\psi_r(\mathbf{r}')\psi_s(\mathbf{r}')\,d\mathbf{r}d\mathbf{r}' + \int \frac{\partial^2 E_{\text{XC}}}{\partial\rho(\mathbf{r})\rho(\mathbf{r}')}\psi_p(\mathbf{r})\psi_q(\mathbf{r})\psi_r(\mathbf{r}')\psi_s(\mathbf{r}')\,d\mathbf{r} \tag{2.72}$$

$$= (pq|rs) + (pq|\hat{f}_{\text{XC}}|rs). \tag{2.73}$$

Making use of the following relations

$$F^0_{pp} = \varepsilon_p \tag{2.74}$$

$$P^0_{pp} = 1 \tag{2.75}$$

we arrive at the TDDFT equations

$$\begin{pmatrix} \mathbf{A} & \mathbf{B} \\ \mathbf{B}^* & \mathbf{A}^* \end{pmatrix} \begin{pmatrix} \mathbf{X} \\ \mathbf{Y} \end{pmatrix} = \omega \begin{pmatrix} 1 & 0 \\ 0 & -1 \end{pmatrix} \begin{pmatrix} \mathbf{X} \\ \mathbf{Y} \end{pmatrix} \tag{2.76}$$

where the elements of matrices **A** and **B** are

$$A_{ia,jb} = \delta_{ij}\delta_{ab}(\varepsilon_a - \varepsilon_i) + (ai|bj) + (ai|\hat{f}_{\mathrm{XC}}|bj) \tag{2.77}$$

$$B_{ia,jb} = (ai|jb) + (ai|\hat{f}_{\mathrm{XC}}|jb). \tag{2.78}$$

The TDDFT equations are solved to give the excitation energies ω. The derivation shown is applicable to all forms of exchange-correlation functional but the form of the elements of matrices **A** and **B** given in equations (2.77) and (2.78) are valid only for local or GGA functionals. In order to accommodate hybrid functionals, it is necessary to account for the additional term in the KS Fock operator originating from exact orbital exchange. For a hybrid functional, the form of the matrices **A** and **B** is

$$A_{ia,jb} = \delta_{ij}\delta_{ab}(\varepsilon_a - \varepsilon_i) + (ia|jb) + (1 - c_{\mathrm{HF}})(ia|\hat{f}_{\mathrm{xc}}|jb) + c_{\mathrm{HF}}(ij|ab) \tag{2.79}$$

$$B_{ia,jb} = (ia|bj) + (ia|\hat{f}_{\mathrm{XC}}|bj) + c_{\mathrm{HF}}(ia|bj), \tag{2.80}$$

where c_{HF} denotes the proportion of exact exchange included.

Failures within TDDFT

The most notable failures of GGA and hybrid functionals for calculating excitation energies are those that are Rydberg or charge-transfer in character. Firstly, the failure to describe Rydberg transitions will be discussed, as well as a scheme for solving this problem. Secondly, the charge-transfer failure will be discussed and the role of exact orbital exchange in resolving this issue will be considered.

As the number of electrons of a system passes through an integer number, the exchange-correlation potential exhibits a discontinuity.[66] On the electron deficient side, the potential approaches zero asymptotically while on the electron abundant side, the potential approaches a limiting value of Δ_{XC}.[67] In both cases, the potential exhibits a $-1/r$ dependence. GGA functionals do not exhibit any discontinuity and can therefore, at best, average over it. In regions of non-negligible electron density they are known to approximately average over the discontinuity[68] and should therefore approach a limiting value of $\Delta_{\mathrm{XC}}/2$.[69,70] The result of this is that occupied orbital energies are shifted up in energy. For example, in exact DFT it is known that the energy of the HOMO orbital is equal to the negative of the ionisation potential. However, in a GGA, this becomes

$$\epsilon_{\mathrm{HOMO}} \approx -I + \frac{\Delta_{\mathrm{XC}}}{2}. \tag{2.81}$$

Asymptotically, the GGA potential does not approach $\Delta_{\mathrm{XC}}/2$ but decays rapidly to zero. The result is that the potential is insufficiently deep to bind orbitals that would otherwise be bound in the real system. Excitations to these orbitals, now lying in the continuum, are significantly underestimated. This has significant consequences for the description of Rydberg excitations. To solve this problem, the long-range form of the potential can be forced to decay with the correct $-1/r$ behaviour to the correct limiting value[71]

$$\lim_{r\to\infty} v_{\mathrm{XC}}(\mathbf{r}) = -\frac{1}{r} + \frac{\Delta_{\mathrm{XC}}}{2}, \tag{2.82}$$

where $\Delta_{\mathrm{XC}}/2$ is approximated asymptotically as the sum of the ionisation potential and the energy of the HOMO. While fixing the asymptotic behaviour of the potential in this manner fixes errors in Rydberg excitations, it does not address the problem of charge-transfer excitations.

It has been shown that conventional functionals frequently underestimate the energies of charge-transfer excitations.[72–76] The origin of this failure has been discussed[77–79] and is illustrated here by considering the case of an electron moving from an occupied orbital i on a donor molecule (D) to a virtual orbital a on an acceptor molecule (A) which are spatially well separated by a distance R. In such a case, the exact excitation

energy is

$$\omega^{\text{exact}} = \text{IP}^{\text{D}} - \text{EA}^{\text{A}} - \frac{1}{R} \tag{2.83}$$

where IP and EA stand for the ionisation potential and electron affinity, respectively. The $-1/R$ dependence arises from the Coulomb attraction between the resultant charged species. For GGA functionals, when the donor and acceptor molecules are sufficiently separated, all two-electron integrals in the matrices $\mathbf{A}$ and $\mathbf{B}$ will approach zero and the TDDFT equation reduces to an orbital energy difference

$$\omega_{\text{GGA}}^{\text{TDDFT}} = \varepsilon_a^{\text{A}} - \varepsilon_i^{\text{D}}. \tag{2.84}$$

The error in the charge-transfer excitation will therefore be

$$\omega^{\text{TDDFT}} - \omega^{\text{exact}} = \varepsilon_a^{\text{A}} - \varepsilon_i^{\text{D}} - (\text{IP}^{\text{D}} - \text{EA}^{\text{A}}), \tag{2.85}$$

which is approximately equal to the average of the integer discontinuities of the donor and acceptor molecules.[78] It can be seen that the closer the orbital energy values are to the ionisation potential and the electron affinity, the lower the error in the charge-transfer excitation energy will be. By augmenting GGA functionals with exact orbital exchange, the quality of HOMO and LUMO orbital energies is improved and therefore, the excitation energies are better.

For such hybrid functionals, the two-electron integrals in $\mathbf{A}$ corresponding to exact Hartree-Fock exchange are non-zero. Again, all integrals in $\mathbf{B}$ approach zero. The excitation energy is therefore

$$\omega_{\text{hybrid}}^{\text{TDDFT}} = \epsilon_i^{\text{D}} - \epsilon_a^{\text{A}} - \frac{c_{\text{HF}}}{R}. \tag{2.86}$$

It is clear that at large separation, excitation energies from GGA functionals have no R dependence and excitation energies from hybrid functionals have the incorrect R dependence. It should be noted that at infinite separation, the expression for the excitation energy from a hybrid functional reduces to the one for a GGA. This analysis clearly shows that for the correct description of charge-transfer excitations it is nec-

essary for an exchange-correlation functional to incorporate some exact Hartree-Fock exchange, as it is this term which introduces the required $1/R$ dependence. The correct R dependence can only be achieved with 100% exact exchange. By incorporating exact orbital exchange to fix the quality of the charge-transfer excitations, the correct asymptotic form of the potential is also achieved, meaning this approach not only corrects charge-transfer underestimation but also Rydberg excitations. Accurate predictions for charge-transfer excitations have been reported when using CAM-B3LYP[80–83] (despite it not having 100% long-range exact-exchange).

Predicting charge-transfer failures

As shown in the preceding section, the failure of conventional functionals to predict charge-transfer excitation energies within TDDFT is a major problem. In order to address this, Peach *et al.*[84] introduced a diagnostic tool for predicting the likelihood of underestimation of excitation energies with different classes of exchange correlation functionals. They based this tool on the quantity

$$O_{ia} = \langle |\phi_i| \, | \, |\phi_a| \rangle \tag{2.87}$$

which measures the extent of spatial overlap between any occupied-unoccupied orbital pairs involved in a given excitation. The moduli in equation (2.87) prevents orthogonal orbital pairs giving zero overlap. Each overlap is weighted by

$$\kappa_{ia} = X_{ia} + Y_{ia}, \tag{2.88}$$

where X_{ia} and Y_{ia} are solutions to the TDDFT equations (2.76). The resulting diagnostic quantity is

$$\Lambda = \frac{\sum_{ia} \kappa_{ia}^2 O_{ia}}{\sum_{ia} \kappa_{ia}^2}, \tag{2.89}$$

normalised such that it takes values of $0 \leq \Lambda \leq 1$. A value of $\Lambda = 0$ signifies a transition between two orbitals which are infinitely separated. A value of $\Lambda = 1$ signifies a transition between two orbital which are spatially identical. The study by Peach *et al.* found that for GGA functionals, an excitation energy with a value of $\Lambda < 0.4$ is likely

to be significantly underestimated. For hybrid functionals, the performance is slightly better and values of $\Lambda < 0.3$ indicate excitation energies which are likely to be incorrect. The nature of this diagnostic tool is such that a value above the given threshold does not guarantee an accurate description of the relevant excitation energy. Indeed, the same workers found just such a case in a subsequent paper.[85]

Chapter 3

Dispersion, fractional spins and fractional charges

The errors arising due to dispersion, fractional spins and fractional charges are considered through two prototypical examples, H_2 and H_2^+. These examples are considered from the standard viewpoint of the energy and also the non-conventional viewpoint of the *force*. It is shown how the variation of the force is determined by the degree to which the density of each system is distorted through the electrostatic theorem of Feynman. For both fractional spins (illustrated by H_2) and fractional charges (illustrated by H_2^+), the proportion of exact exchange incorporated into exchange-correlation functionals has a significant effect on the quality of the results. In the former, functionals with large quantities of exact exchange—including CAM-B3LYP—perform poorly whereas in the latter they provide an improved description over conventional local functionals and hybrid functionals with smaller quantities of exact exchange. Errors in forces and density distortions are related to erroneous terms in the Kohn-Sham equation.

Three areas where exchange-correlation functionals in modern DFT are particularly susceptible to failure is in the accurate description of dispersion, fractional spins and fractional charges.[86–88] The associated errors manifest themselves in poor descriptions of the dissociation of molecules (present chapter), weakly-bound complexes (see chapter 4) and charge-transfer excitation energies (see chapters 5, 6 and 7) among others.[89–91] The dispersion problem refers to the lack of a long-range C_6R^{-6} interaction energy in non-overlapping systems (a more detailed discussion is provided in section 4.1). Systems with (locally) fractional spins tend to suffer from an overestimation of the energy and

this is investigated through stretched H_2, which consists of two atoms, each with half an alpha and half a beta electron. Systems with fractional charges tend to suffer from an underestimation of the energy and this is investigated through stretched H_2^+, consisting of two atoms, each with half an electron. To facilitate the analysis, the internuclear forces, potential energy curves and density distortions are employed to build up a picture of each molecule at large internuclear separations. The errors which arise are interpreted in terms of both the energy and the force. The electrostatic theorem of Feynman is used to relate the forces and the density distortions, which can then be related to errors in the Kohn-Sham orbital equations.

Nuclear forces are determined using conventional analytic gradient techniques—i.e. the true energy derivative,

$$F_{\mathrm{A}} = -\frac{\partial E}{\partial z_{\mathrm{A}}}, \tag{3.1}$$

where, for a diatomic system consisting of two nuclei A and B, the force on nucleus A (F_{A}) is a function of the z component of the nuclear coordinate of A and the electronic energy is E. Nuclear forces are also determined using the electrostatic theorem.[43,44] The electrostatic theorem states that the force arises due to the classical interaction with other nuclei and the electron density,

$$F_{\mathrm{A}}^{\mathrm{el}} = -\frac{Z_{\mathrm{A}} Z_{\mathrm{B}}}{R^2} - Z_{\mathrm{A}} \int \frac{\rho(\mathbf{r}_1) z_{1\mathrm{A}}}{r_{1\mathrm{A}}^3}\, d\mathbf{r}_1, \tag{3.2}$$

where $r_{1\mathrm{A}}$ is the distance from nucleus A to electron coordinate $\mathbf{r}_1$, of which the z-component is $z_{1\mathrm{A}}$ and Z_{A} is the nuclear charge of A. By calculating forces in this manner, it is possible to obtain physical insight by understanding the forces in terms of the electron density. When considering nucleus A, a positive force corresponds to an attractive interaction. The electrostatic theorem is formally exact, but breaks down for non-variational methodologies and/or finite basis sets. It is therefore necessary to consider only variational methods (full CI, Hartree-Fock and DFT) and extensive basis sets to minimise any associated errors.

There have been few previous studies where the force has been of central interest in the same way in which it is here. One such study was conducted by Allen and Tozer[92]

Table 3.1: Electrostatic forces (a.u.) and associated BSSE corrections for He_2 calculated with BD(T)/Dc147 with f-functions removed. F_{SAPT} acts as a reference.

R/a_0	F^{el}	BSSE Correction	Corrected F^{el}	F_{SAPT}
8.0	4.66	0.18	4.84	5.10
8.5	3.13	0.13	3.20	3.30
9.0	2.04	0.08	2.12	2.20

and concerned the forces in stretched He_2 as calculated using the coupled cluster based approach of Brueckner doubles with perturbative triples (BD(T))[93–95] and the Dc147 basis set.[96] The results obtained in that study have been reproduced and are shown in table 3.1. It can be seen that, due to the incompleteness of the Dc147 basis set, the application of a basis set superposition error (BSSE) correction was necessary. A detailed discussion of BSSE is provided in the next chapter (section 4.2). However, its effect can be understood as the overlapping of basis functions causing an artificial lowering of the energy. In this case, as the basis functions overlap in the region between the two helium atoms, this lowering of energy is accompanied by an artificial increase in the force experienced between the two nuclei. It should therefore be expected that the application of a BSSE correction will not only increase the energy, but also reduce the internuclear force. However, as can be seen from the data in table 3.1, the correction to the force in fact increases its magnitude. The improvement of the force is therefore due to a fortuitous inaccuracy in the BSSE correction which arises from the incompleteness of the basis set. By reintroducing the f-functions which were omitted in the study of Allen and Tozer, it is possible to generate new data, closer to the basis set limit, which is shown in table 3.2. The BSSE correction now, correctly, reduces the force. It is now the case that the uncorrected forces which initially appeared good, are worsened. The reference values here are the same as those used by Allen and Tozer and are based on accurate SAPT interaction energies fitted to an interatomic potential.

The inaccuracy of the electrostatic force lies in the quality of the electron density used. To improve the accuracy of the electrostatic force, two approaches can be used: increasing the basis set size and increasing the internuclear distance. Both are equivalent to decreasing the required correction due to BSSE and thus improving the accuracy of the electron density. It is clear from this analysis that extremely accurate densities are

Table 3.2: Electrostatic forces (a.u.) and associated BSSE corrections for He_2 calculated with BD(T)/Dc147 with f-functions included. F_{SAPT} acts as a reference.

R	F^{el}	BSSE Correction	Corrected F^{el}	F_{SAPT}
8.0	4.85	−0.52	4.33	5.10
8.5	3.14	−0.33	2.81	3.30
9.0	2.08	−0.20	1.88	2.20

required to draw meaningful conclusions from the electrostatic theorem. This is more achievable with H_2 and H_2^+ given the simplicity of these systems. To guarantee densities of high accuracy, an extensive basis set is employed throughout. Given the size of this basis set, the errors arising from basis set overlap are below the precision quoted and therefore, BSSE corrections need not be considered.

We now turn to the question of what can be learnt from the evaluation of H_2 and H_2^+ at large internuclear separations, employing a variety of electronic structure methods. For H_2 and H_2^+, the force from the electrostatic theorem (equation (3.2)) reduces to

$$F_{\mathrm{A}}^{\mathrm{el}} = -\frac{1}{R^2} - \int \frac{\rho(\mathbf{r}_1) z_{1\mathrm{A}}}{r_{1\mathrm{A}}^3}\, d\mathbf{r}_1. \tag{3.3}$$

The first term in equation (3.3) is the force due to the nucleus B, whilst the second term is the force due to the total electron density. For large internuclear separations, it is appropriate to partition space into two regions. The force on nucleus A can then be defined in terms of the electron density around each individual nucleus

$$F_{\mathrm{A}}^{\mathrm{el}} = -\frac{1}{R^2} - \int \frac{\rho_{\mathrm{A}}(\mathbf{r}_1) z_{1\mathrm{A}}}{r_{1\mathrm{A}}^3}\, d\mathbf{r}_1 - \int \frac{\rho_{\mathrm{B}}(\mathbf{r}_1) z_{1\mathrm{A}}}{r_{1\mathrm{A}}^3}\, d\mathbf{r}_1 \tag{3.4}$$

$$= -\frac{1}{R^2} + F_{\mathrm{A}}^{\mathrm{el},\rho_{\mathrm{A}}} + F_{\mathrm{A}}^{\mathrm{el},\rho_{\mathrm{B}}} \tag{3.5}$$

where $\rho_{\mathrm{A}}(\mathbf{r}_1)$ and $\rho_{\mathrm{B}}(\mathbf{r}_1)$ are electron densities obtained by partitioning space into two equal regions either side of the bond midplane. The forces $F_{\mathrm{A}}^{\mathrm{el},\rho_{\mathrm{A}}}$ and $F_{\mathrm{A}}^{\mathrm{el},\rho_{\mathrm{B}}}$ are the classical attraction of the nucleus A towards the electron density of fragments A and B, respectively. These forces can be determined numerically using the standard numerical integration schemes in DFT programs—extensive testing has been performed to confirm the numerical integration grid is sufficiently large to give numerical forces from the electrostatic theorem which are indistinguishable from the analytically determined

equivalent. Calculations are performed with the Cadpac[97] and Dalton[98] programs, using a restricted and unrestricted formalism for H_2 and H_2^+, respectively. A range of functionals, with varying amounts of exact exchange are chosen: BLYP (GGA, 0% exchange), B3LYP (hybrid, 20% exchange), CAM-B3LYP (coulomb-attenuated, 19% increasing to 65% exchange) and CAM-B3LYP ($\alpha + \beta = 1$) (coulomb-attenuated, 20% increasing to 100% exchange). For H_2^+, only the exchange components of the functionals are considered and the results are denoted B, B3, CAM-B3 and CAM-B3 ($\alpha+\beta = 1$), respectively. Full CI results are also presented which are exact (within the basis set) and correspond to CCSD calculations for H_2 and Hartree-Fock for H_2^+. All calculations are performed with the d-aug-cc-pV6Z basis set where g and h functions have been removed for technical reasons and, given the preceding discussion, BSSE corrections are not required.

Figures 3.1 and 3.2 show the full potential energy curves for H_2 and H_2^+, respectively. From this viewpoint of the energy it is clear to see the fractional spin error causes an overestimation in the energy whereas the fractional charge error causes an underestimation. As the amount of exchange increases from BLYP to B3LYP to CAM-B3LYP to CAM-B3LYP ($\alpha + \beta = 1$), the fractional spin error increases whereas the fractional charge error decreases. The origin of these errors will now be investigated using the definitions outlined above for the exact force (F_A), the full electrostatic force (F_A^el) and the electrostatic force due to the electron density around one nucleus ($F_\mathrm{A}^{\mathrm{el},\rho_\mathrm{A}}$).

3.1 Dispersion and Fractional spins: H_2

For H_2, the comparison of the force (F_A), the electrostatic force (F_A^el) and the electrostatic force due to the electron density around nucleus A ($F_\mathrm{A}^{\mathrm{el},\rho_\mathrm{A}}$) at $R = 13$ $\mathrm{a_0}$ is shown in table 3.3. For all methods considered, the electrostatic force is almost exactly equal to the exact force, confirming the validity of the electrostatic theorem. The F_A values correspond to the slopes of the potential energy curves at $R = 13$ $\mathrm{a_0}$.

At large values of R, the density around nucleus B, $\rho_\mathrm{B}(\mathbf{r})$, contains one localised electron, thus the attraction of nucleus A to this electron and the repulsion from nucleus B approximately cancel

$$F_\mathrm{A}^{\mathrm{el},\rho_\mathrm{B}} \approx \frac{1}{R^2} \tag{3.6}$$

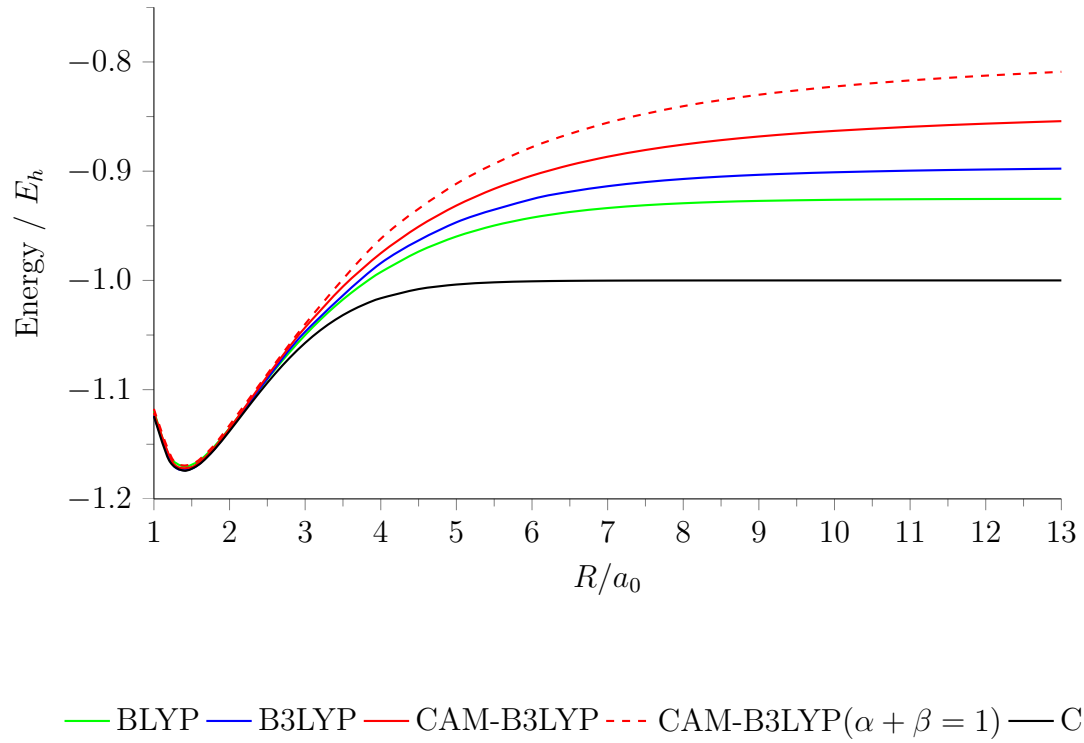

Figure 3.1: Potential Energy Curves for H_2 (using d-aug-cc-pV6Z).

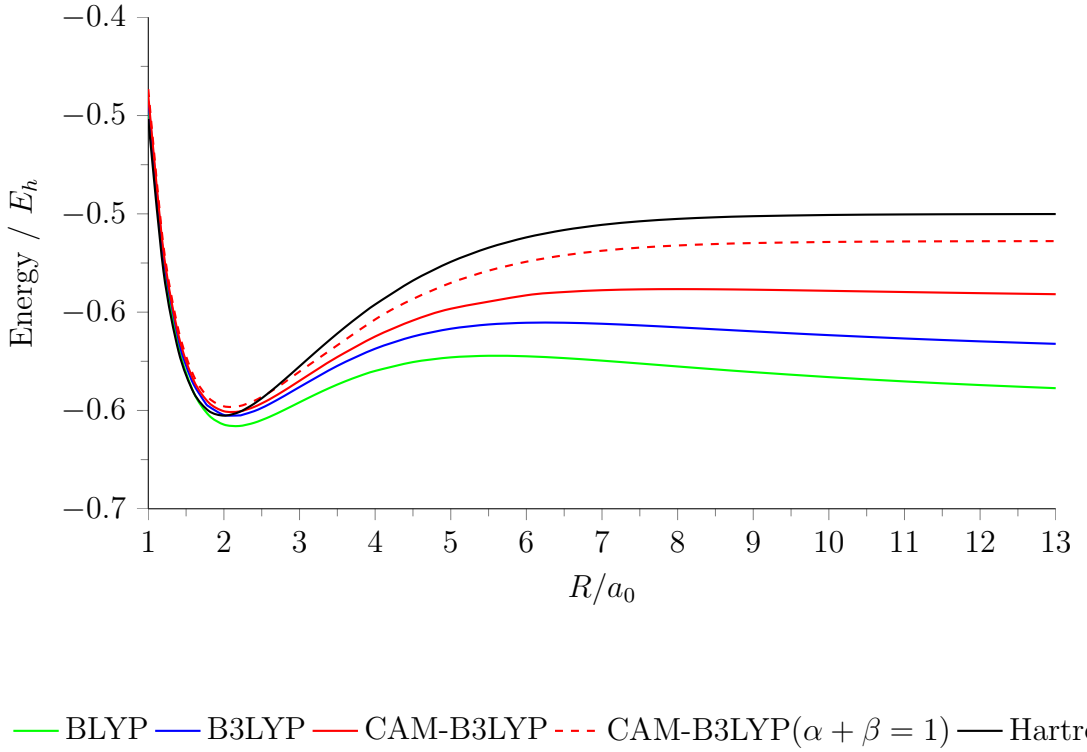

Figure 3.2: Potential Energy Curves for H_2^+ (using d-aug-cc-pV6Z).

Table 3.3: H_2 Forces (a.u.) at 13 a_0.

Method	F_{A}	$F_{\mathrm{A}}^{\mathrm{el}}$	$F_{\mathrm{A}}^{\mathrm{el},\rho_{\mathrm{A}}}$
CCSD (Exact)	7.37×10^{-7}	7.34×10^{-7}	7.69×10^{-7}
BLYP	7.65×10^{-5}	7.64×10^{-5}	7.24×10^{-5}
B3LYP	7.00×10^{-4}	6.99×10^{-4}	6.89×10^{-4}
CAM-B3LYP	2.07×10^{-3}	2.07×10^{-3}	2.05×10^{-3}
CAM-B3LYP($\alpha + \beta = 1$)	3.21×10^{-3}	3.21×10^{-3}	3.16×10^{-3}

yielding

$$F_{\mathrm{A}} \approx F_{\mathrm{A}}^{\mathrm{el}} \approx F_{\mathrm{A}}^{\mathrm{el},\rho_{\mathrm{A}}}. \tag{3.7}$$

The net force exerted on nucleus A must therefore arise due to a *distortion* of the electron density around A away from spherical. There is a generally good agreement between F_A^{el} and F_A^{el,ρ_A}—confirming that the force on nucleus A is arising from a distortion of the electron density around that nucleus. In order to illustrate this distortion it is useful to consider not the density, but rather the density difference, defined as

$$\Delta\rho(\mathbf{r}) = \rho_{\mathrm{AB}}(\mathbf{r}) - \rho_{\mathrm{A}}(\mathbf{r}) - \rho_{\mathrm{B}}(\mathbf{r}), \tag{3.8}$$

where $\rho_{\mathrm{AB}}(\mathbf{r})$ is the density of the diatomic and $\rho_{\mathrm{A}}(\mathbf{r})$ and $\rho_{\mathrm{B}}(\mathbf{r})$ are spherical, atomic densities associated with nuclei A and B, respectively. These latter two densities are determined from calculations on the diatomic at $R = 10^7$ a_0.

The force calculated using CCSD—which is exact for H_2—is 7.37×10^{-7}au at $R = 13$ a_0. At this distance the only interaction is due to dispersion. The exact dispersion force can be calculated using experimental dispersion coefficients,[99]

$$F_{\mathrm{A}}^{\mathrm{disp}}(R = 13a_0) = 6C_6R^{-7} + 8C_8R^{-9} + \cdots = 7.38 \times 10^{-7}\text{a.u.}, \tag{3.9}$$

showing excellent agreement with CCSD. The non-zero force exerted on nucleus A is the result of the distortion of the density which can be observed in figure 3.3. Feynman conjectured[44] that the only source of the R^{-7} component of the dispersion interaction is the attraction of the nucleus to the distorted electron density that surrounds it,

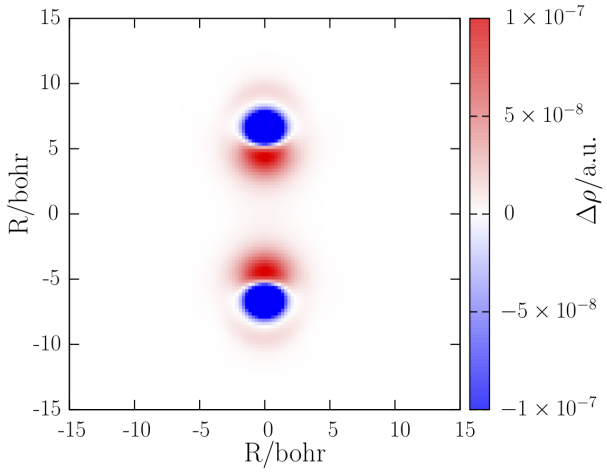

Figure 3.3: H_2 CCSD density distortion

which has been verified for H_2 by Hirschfelder and Eliason.[100] Note that all subsequent density difference plots for H_2 will be plotted on a different scale, which is two orders of magnitude larger than that used for the CCSD case in figure 3.3. This is required due to the significantly larger distortion observed when less accurate electronic structure methods are used. For comparison, the CCSD density difference is replotted on the new scale in figure 3.4(a), where it can be seen that the distortion is barely visible.

From the results in table 3.3, it can be seen that when employing DFT methods, the force becomes increasingly overestimated (too attractive) with increasing amounts of exact exchange. This is reflected in the increased gradients of the potential energy curves plotted in figure 3.1. At $R = 13$ a_0, the CCSD curve is essentially flat, corresponding to isolated atoms whereas—at the other extreme—CAM-B3LYP($\alpha + \beta = 1$) still exhibits a noticeable slope. The origin of this trend in increasing force is evident from the density difference plots of figure 3.4 where it can be seen that there is an increasing degree of distortion of the density. The fractional spin error manifests itself as an overestimated force due to an exaggerated density distortion.

In the vicinity of nucleus A, the exact potential experienced by an electron should be $-\frac{1}{r_A}$, given the molecule is essentially dissociated. For the DFT functionals considered, there is an additional erroneous term equal to $-\frac{\xi}{2r_B}$, where ξ is the amount of long-range exact exchange. The result of this additional term is that an electron near nucleus A is attracted to a fractional positive charge on atom B equal to $1 - \frac{\xi}{2}$, which causes the exaggerated distortion of the electron density. For both Hartree-Fock and CAM-B3LYP

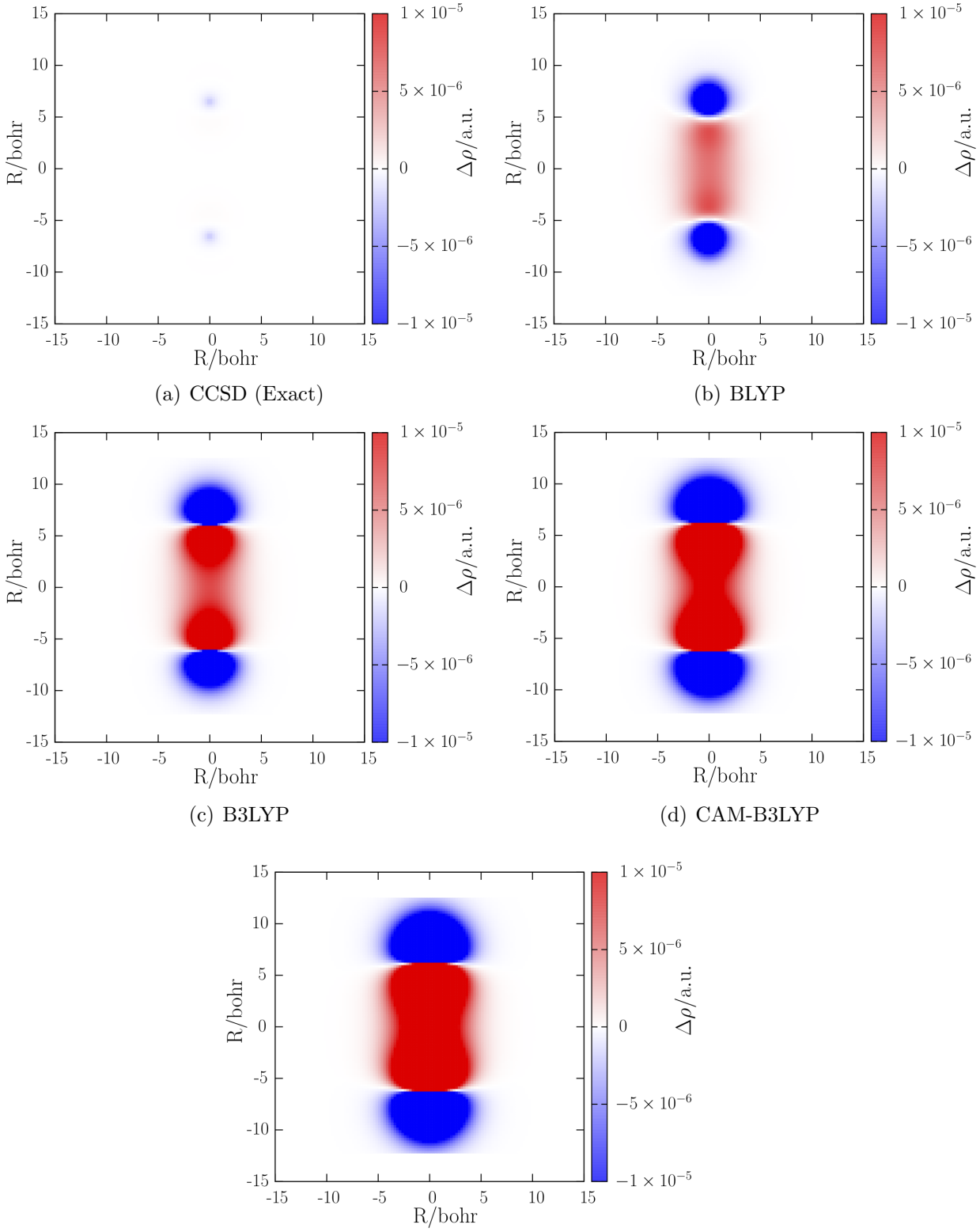

(a) CCSD (Exact)

(b) BLYP

(c) B3LYP

(d) CAM-B3LYP

(e) CAM-B3LYP ($\alpha + \beta = 1$)

Figure 3.4: H_2 $\Delta\rho$ plots illustrating the density distortion.

($\alpha+\beta=1$), which both correspond to 100% exact exchange at this distance, this results in attraction to a 0.5 positive charge on atom B, reflecting the standard explanation that the wavefunction incorrectly contains 50% ionic character. For these two methods, the forces in table 3.3 are essentially equal to $-\frac{0.5}{R^2}$.

The fractional spin error outweighs any error due the functionals missing the dispersion interaction. DFT calculations on He_2, which does not exhibit a fractional spin error, would yield a density distortion much smaller than the exact distortion and hence, no R^{-7} dispersion force. This was explicitly illustrated in Ref 92 in the context of Hartree-Fock-Kohn-Sham calculations.

3.2 Fractional charges: H_2^+

From the values in table 3.4, the similarity between F_A and F_A^{el} for H_2^+ again confirms the validity of the electrostatic theorem. However, there is now a significant difference in F_A^{el,ρ_A}. As there is only one electron, the density around nucleus B only contains half an electron. As a result, the repulsion of nucleus B is no longer approximately cancelled by the density around B but rather

$$F_A^{el,\rho_B} \approx \frac{1}{2R^2} \tag{3.10}$$

and so there is a net force exerted on nucleus A of

$$F_A \approx -\frac{1}{2R^2} + F_A^{el,\rho_A}. \tag{3.11}$$

The force on nucleus A can no longer be attributed just to the electron density around A. In the exact case (now Hartree-Fock), close to dissociation at $R = 13$ a_0, the force exerted on each nucleus is close to zero (see table 3.4). In order to produce a total force near zero, the force due to the density around nucleus A must almost exactly cancel the repulsive $-1/2R^2$ term arising from the proton/half-electron system at B. Indeed, the Hartree-Fock value of $F_A^{el,\rho_A} = -2.99 \times 10^{-3} \approx 1/2R^2$ and the significant density distortion in figure 3.5(a) reflects this. The significant distortion in this case is simply a result of the attraction to nucleus B which is now shielded by only half an electron. This distortion is necessary to counteract the repulsive force experienced between the

Table 3.4: H_2^+ Forces (a.u.) at 13 a_0 (using d-aug-cc-pV6Z)

Method	F_A	F_A^{el}	F_A^{el,ρ_A}
Hartree-Fock (Exact)	4.59×10^{-5}	4.41×10^{-5}	2.99×10^{-3}
BLYP	-1.47×10^{-3}	-1.48×10^{-3}	1.48×10^{-3}
B3LYP	-1.17×10^{-3}	-1.17×10^{-3}	1.78×10^{-3}
CAM-B3LYP	-4.91×10^{-4}	-4.93×10^{-4}	2.46×10^{-3}
CAM-B3LYP($\alpha + \beta = 1$)	4.20×10^{-5}	3.98×10^{-5}	2.99×10^{-3}

two positively charged nuclei.

From the results in table 3.4 it can be seen that for the BLYP GGA functional, the net force is $F_A = -1.47 \times 10^{-3}$a.u., which represents a *repulsive* force of essentially $-\frac{1}{4R^2}$ (as would arise from the interaction of two half-plus fragments). The force on nucleus A due to the density surrounding it is therefore $F_A^{el,\rho_A} \approx \frac{1}{4R^2}$. The density does therefore distort towards nucleus B as shown in figure 3.5, but not sufficiently to overcome the repulsion from fragment B, giving a net repulsive interaction. Interestingly, the use of LDAX and other GGA exchange functionals yield identical forces and density distortions.

Increasing the amount of exact orbital exchange causes the forces to become less repulsive and then attractive. The CAM-B3LYP ($\alpha + \beta = 1$) forces are in excellent agreement with the exact Hartree-Fock values. This increase in force is a result of the increased density distortion, as shown in figure 3.5. The fractional charge error therefore manifests itself as an underestimated force due to an underestimated density distortion. In the vicinity of nucleus A, an electron should experience an effective potential of $-\frac{1}{r_A} - \frac{1}{r_B}$, the latter term being responsible for the distortion of the density. The Kohn-Sham operator, in this case, contains an additional erroneous term of $-\frac{1}{2r_B}(\xi - 1)$. For small ξ, the $-\frac{1}{r_B}$ term is partly cancelled, reducing the distortion. As ξ increases, this term vanishes and the correct, larger distortion is obtained.

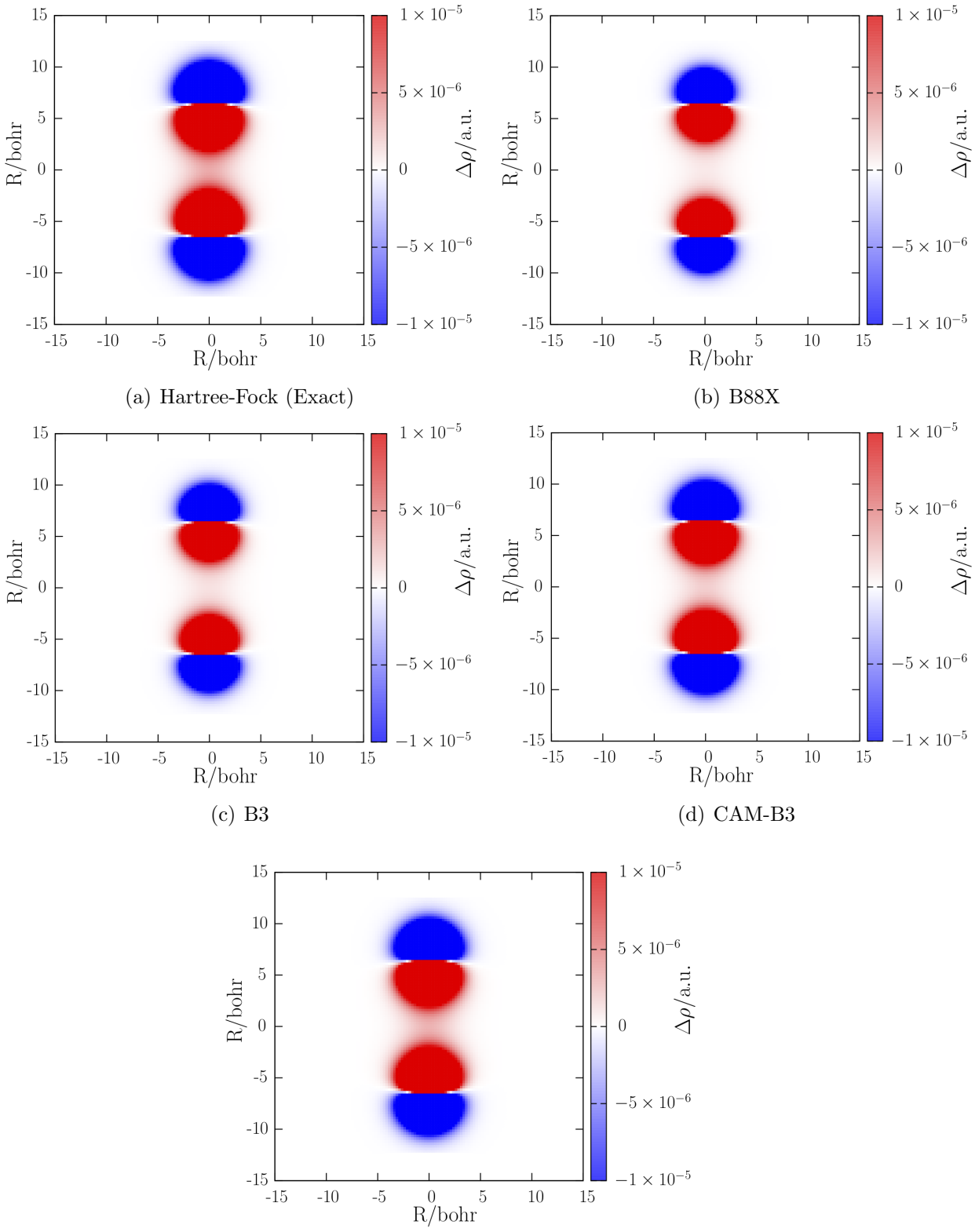

(a) Hartree-Fock (Exact)

(b) B88X

(c) B3

(d) CAM-B3

(e) CAM-B3 ($\alpha + \beta = 1$)

Figure 3.5: H_2^+ $\Delta\rho$ plots illustrating the density distortion.

Summary

The key problems of dispersion, fractional spins and fractional charges have been considered from the viewpoint of the force. Through the use of the electrostatic theorem, these forces have been related to distortions of the density. The example of H_2 shows how the dispersion force arises from a distortion of the density—the sometimes overlooked interpretation of Feynman. H_2 was also used to illustrate the fractional spin error which, in the case of DFT functionals containing long-range exact exchange, results in an overestimation of the force due to an exaggerated density distortion. Conversely, the example of H_2^+ shows how long-range exact exchange is necessary for systems with fractional charges where the force is underestimated due to an underestimated density distortion. The fact that exact exchange is detrimental in the former case yet necessary in the latter case presents a challenging problem which, through a consideration of the force and density distortion, has been provided with new physical insight.

Chapter 4

C_6 coefficients from DFT and the DFT-D approach

Continuing the theme of weak interactions, this chapter considers the performance of a variety of functionals in determining the C_6 dispersion coefficient, with CAM-B3LYP providing greater accuracy than conventional GGA and hybrid functionals. The potential energy surfaces of rare-gas diatomics are constructed using DFT with an empirical dispersion correction based on the C_6 dispersion coefficient. Dispersion corrected interaction energies of biologically relevant systems are also determined. CAM-B3LYP shows a performance of comparable accuracy to other long-range corrected functionals for determining dispersion corrected interaction energies. The role of the attenuation parameters within CAM-B3LYP for the accurate treatment of the dispersion interaction is illustrated. The need for flexibility in the form of the dispersion correction is highlighted.

4.1 Calculating C_6 coefficients

The weak non-electrostatic interactions between atoms and molecules are covered by the 'van der Waals' label. The attractive component of this interaction is the ubiquitous dispersion or London interaction. Traditionally, this interaction is considered as arising from the interaction of induced dipole moments; instantaneous fluctuations in electron density on one species gives rise to a dipole moment which then induces a dipole moment on a neighbouring species.[101,102] This attractive interaction is present between well-separated molecules, even in the absence of permanent multipole moments.[103] The

dispersion energy can be defined in terms of an interatomic or intermolecular distance R and a dispersion coefficient C_{2n} as

$$E_{\text{disp}} = -\sum_{n=3} C_{2n} R^{-2n}. \tag{4.1}$$

For intermolecular systems, this assumes a C_{2n} coefficient for an entire molecule. It is possible to consider the intermolecular interaction as a sum of interatomic interactions and this is discussed in section 4.2. It is common to truncate this expression at the first term, requiring only one dispersion coefficient, C_6. This is the only coefficient that will be considered in the present work. Other terms contribute less because of higher-order distance dependence so neglecting them is not significant in many cases.

The role of the dispersion interaction in chemistry must not be understated. It is responsible for crucial biological[104–107] self-assembly. The structure of proteins and the stacking of DNA base pairs are just two examples of where the dispersion interaction plays a significant role in conferring conformation and stability. The dispersion interaction is also responsible for the condensation of and binding between noble gas atoms—examples of which will be considered here.

Although a number of routes exist to the determination of C_6 coefficients,[108–110] they are determined here through the Casimir-Polder identity[111]

$$C_6^{ij} = \frac{3}{\pi} \int \alpha^i(\mathrm{i}\omega)\alpha^j(\mathrm{i}\omega) d\omega, \tag{4.2}$$

where i and j denote the species that the dispersion interaction is between. The frequency dependent polarisability $\alpha(\mathrm{i}\omega)$ at imaginary frequency ω is calculated in terms of Cauchy coefficients S_{-2l} using the Cauchy expansion,

$$\alpha(\mathrm{i}\omega) = \sum_{l=1}^{\infty} S_{-2l} \mathrm{i}\omega^{2(l-1)}. \tag{4.3}$$

Since the C_6 coefficients considered are isotropic they can be calculated from isotropic polarisabilities,

$$\alpha = \frac{1}{3}(\alpha_{xx} + \alpha_{yy} + \alpha_{zz}). \tag{4.4}$$

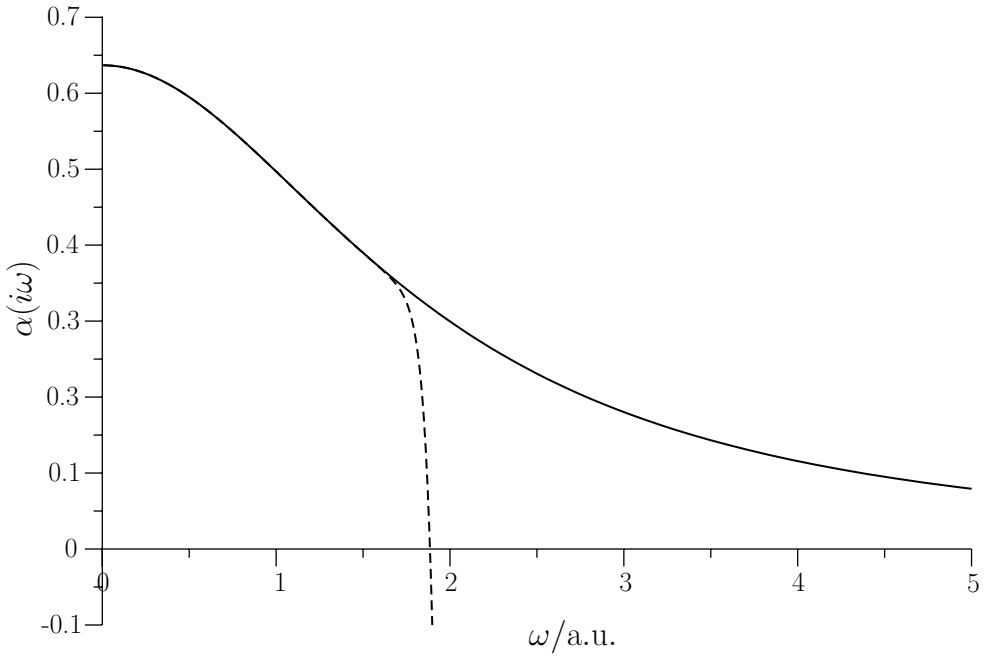

Figure 4.1: The B3LYP frequency dependent polarisability of helium determined using the Cauchy expansion (dashed) and computed directly (solid).

The Cadpac programme provides C_6 coefficients as standard output and was therefore used in the preliminary calculations. As there was no implementation of CAM-B3LYP in Cadpac available, we then used Dalton and equation (4.3) to determine C_6 coefficients. However, the Cauchy expansion only holds up to the value of the first excitation energy with non-zero oscillator strength.[112] This breakdown is illustrated in figure 4.1. The result is that the frequency dependent polarisabilities and C_6 coefficients could not be accurately calculated in this manner. The Dalton code was therefore modified to print the frequency dependent polarisability on a predetermined Gauss-Legendre quadrature grid and the C_6 coefficients were accurately obtained using equation (4.2) and the relevant 16-point quadrature scheme similar to that used by Amos *et al.*[113]

Once the required tests and modifications to confirm consistency in the calculation of C_6 coefficients had been successfully completed, the performance of CAM-B3LYP was examined. This functional has not previously been used to determine C_6 coefficients. Although the comparison of most significance is that of CAM-B3LYP with the original B3LYP functional, a number of other functionals are also tested for a broader comparison. The functionals of Keal and Tozer[114,115] are employed given the recent good performance of KT1 in modelling $\pi - \pi$ stacking,[116] and also the B971 functional,[51]

Table 4.1: Static polarisabilities for the S1 set. All values in a.u.

	B3LYP[a]	B3LYP[b]	CAM-B3LYP[b]	DOSD[a]
He	1.51	1.51	1.53	1.38
Ne	2.87	2.88	2.87	2.67
Ar	11.60	11.61	11.48	11.07
H_2	5.55	5.55	5.59	5.43
CO	13.70	13.29	13.21	13.08
CO_2	17.34	17.41	17.32	17.51
N_2	12.04	12.04	12.01	11.74
HCl	18.59	17.98	17.71	17.39
HF	6.23	5.88	5.82	5.60
H_2O	10.14	10.01	9.82	9.64

[a] Ref. 118.
[b]This work

given its performance for van der Waals interactions.[117] All calculations use the d-aug-cc-pVTZ basis set. A C_6 coefficient must, by definition, exist between a pair of atoms or molecules; when a C_6 coefficient is reported for an atom, we assume this refers to the homo nuclear dimer i.e. $i = j$ in equation (4.2). The initial test deals with such homogeneous coefficients while the latter two sets will see the inclusion of mixed pairs.

4.1.1 The S1 set

As a preliminary test the B3LYP/pVTZ+ results presented by Ioannou *et al.*[118] for static isotropic polarisabilities, S_{-4} Cauchy coefficients and C_6 coefficients were reproduced. The results of Ioannou *et al.* are for a set of molecules denoted S1 and consisting of He, Ne, Ar, H_2, CO, CO_2, N_2, HCl, HF and H_2O at near exact geometries (diatomics from Ref. 119, CO_2 and H_2O from Refs. 120 and 121, respectively). Given the confirmation of consistency with the available results, all further calculations employ the d-aug-cc-pVTZ basis set. The verification of the B3LYP results as well as a comparison with CAM-B3LYP is shown in tables 4.1, 4.2 and 4.3. Total errors for C_6 coefficients for each functional are shown in table 4.4. The errors presented are the mean error (d), mean percentage error ($\%d$), mean absolute error ($|d|$) and mean absolute percentage error ($|\%d|$). These errors are determined relative to reference data determined from dipole oscillator strength distribution (DOSD) calculations.[118]

The S1 set is small but balanced. The inclusion of He presents a problem with error

Table 4.2: Cauchy Coefficients (S_{-2l}, $l = 2$) for the S1 set. All values in a.u.

	B3LYP[a]	B3LYP[b]	CAM-B3LYP[b]	DOSD[a]
He	2.0	2.0	2.0	1.6
Ne	3.6	3.7	3.7	3.0
Ar	32.7	32.7	31.5	28.8
H_2	21.7	21.7	21.8	20.0
CO	52.2	51.9	50.6	46.3
CO_2	49.2	49.3	48.5	51.0
N_2	32.5	32.3	31.8	30.1
HCl	79.7	78.3	73.9	67.1
HF	15.2	15.1	14.5	14.4
H_2O	42.0	40.9	38.0	35.4

[a] Ref. 118.
[b]This work

Table 4.3: C_6 coefficients for the S1 set. All values in a.u.

	B3LYP[a]	B3LYP[b]	CAM-B3LYP[b]	DOSD[a]
He	1.63	1.63	1.66	1.46
Ne	6.89	6.90	6.90	6.38
Ar	67.94	68.03	67.20	64.30
H_2	12.37	12.38	12.53	12.09
CO	80.87	81.14	80.69	81.31
CO_2	156.10	157.09	156.28	158.70
N_2	75.24	75.43	75.30	73.43
HCl	132.90	132.38	130.20	130.40
HF	20.36	20.41	20.20	19.00
H_2O	48.14	47.16	46.30	45.37

[a] Ref. 118.
[b]This work

Table 4.4: Mean error (d), mean absolute error ($|d|$), mean percentage error ($\%d$) and mean absolute percentage error ($|\%d|$) in C_6 coefficients for S1 set (a.u.).

System	HF	BLYP	B3LYP	CAM-B3LYP	KT1	KT2	KT3	B97-1
d	−4.36	3.66	1.01	0.48	4.9	2.38	0.73	0.44
$\|d\|$	4.36	3.66	1.37	1.13	4.9	2.38	1.13	1.11
$\%d$	−7.78	9.84	4.23	3.82	10.5	5.59	3.19	3.01
$\|\%d\|$	7.78	9.84	4.48	4.31	10.5	5.59	3.65	3.52

measurement. As there are two orders of magnitude difference in the C_6 values of He and CO_2 the mean absolute error is inappropriate, as information from He (as well as other smaller systems) can be lost. However, if percentage errors are used, small discrepancies in the He value will be distorted. This is of particular relevance given the significantly better performance for all the rare-gas atoms by the KT3 functional (table 4.4). The best performing methods are B3LYP, CAM-B3LYP, KT3 and B97-1, with CAM-B3LYP showing a clear improvement over B3LYP. The high performance of the KT3 functional is surprising, while that of B97-1 is to be expected.[51] These two functionals were therefore employed in further testing alongside B3LYP and CAM-B3LYP.

4.1.2 The S2 set

66 atomic and molecular pairs were chosen from the large dataset compiled by Johnson and Becke.[122] These authors present accurate C_6 coefficients for 178 pairs, but all pairs containing open-shell species were discarded for technical reasons with the remaining closed-shell pairs being sufficient for this study. Any pairs containing the heavier rare-gas diatomics Krypton and Xenon as well as alkanes and alkenes above C_3H_6 were also omitted as it was felt that the smaller analogues captured the essential chemistry without being too computationally demanding. The resulting set is denoted the S2 set (see table 4.5) and is significantly larger than the S1 set. Although it is larger, and therefore likely to be a fairer test of functional quality, the set is somewhat unbalanced due to the frequent occurrence of SiH_4, SiF_4, CCl_4 and Cl_2. Successful performance with the S2 set is, to some extent, based on the performance for these four molecules. All molecular geometries were optimised at the B3LYP/6-31G(2df,p) and CCSD/aug-cc-pVTZ levels to probe the influence of structure on the accuracy of the C_6 coefficients, which were

Table 4.5: Atom and molecule combinations in the S2 set and the associated reference C_6 coefficients (a.u.).

A	B	C_6	A	B	C_6	A	B	C_6
H_2	H_2	12.11	SiH_4	SiH_4	343.9	CCl_4	C_2H_2	642.4
CH_4	CH_4	129.6	SiH_4	Cl_2	363.6	CCl_4	C_2H_4	779.7
CH_4	C_2H_2	162.5	SiH_4	Ar	145.3	CCl_4	C_2H_6	879.0
C_2H_2	C_2H_2	204.1	SiF_4	H	43.28	CCl_4	N_2	382.7
C_2H_4	C_2H_2	247.7	SiF_4	H_2	61.19	CCl_4	CO_2	563.1
C_2H_4	C_2H_4	300.5	SiF_4	He	21.90	CCl_4	Ne	106.3
C_2H_6	C_2H_2	278.9	SiF_4	CH_4	202.3	CCl_4	SiH_4	828.6
C_2H_6	C_2H_6	381.8	SiF_4	C_2H_2	251.9	CCl_4	Cl_2	2024
N_2	N_2	73.39	SiF_4	C_2H_4	306.2	CCl_4	Cl_2	887.5
CO_2	CH_4	142.6	SiF_4	C_2H_6	347.4	CCl_4	Ar	359.1
CO_2	C_2H_2	178.2	SiF_4	N_2	154.8	Cl_2	H	49.76
CO_2	CO_2	158.7	SiF_4	CO_2	227.7	Cl_2	H_2	68.58
SiH_4	H	47.25	SiF_4	Ne	45.40	Cl_2	He	22.93
SiH_4	H_2	64.24	SiF_4	SiH_4	318.7	Cl_2	CH_4	224.6
SiH_4	He	20.78	SiF_4	SiF_4	330.2	Cl_2	C_2H_2	281.7
SiH_4	CH_4	209.4	SiF_4	CCl_4	798.2	Cl_2	C_2H_4	341.9
SiH_4	C_2H_2	264.0	SiF_4	Cl_2	349.5	Cl_2	C_2H_6	385.4
SiH_4	C_2H_4	320.0	SiF_4	Ar	144.6	Cl_2	N_2	167.7
SiH_4	C_2H_6	359.3	CCl_4	H	113.4	Cl_2	CO_2	246.7
SiH_4	N_2	154.6	CCl_4	H_2	156.4	Cl_2	Ne	46.50
SiH_4	CO_2	227.6	CCl_4	He	52.39	Cl_2	Cl_2	389.2
SiH_4	Ne	41.77	CCl_4	CH_4	512.2	Cl_2	Ar	157.4

determined using the established d-aug-cc-pVTZ basis set.

The mean absolute error and the mean absolute percentage errors for the S2 set are reported in table 4.6. CAM-B3LYP again shows a clear improvement over B3LYP. It also benefits from the increased size of the test set by now outperforming both KT3 and B971. The same ordering of functional performance is seen for both sets of geometries, while there is little conclusive evidence for a quantitative improvement when using more accurate geometries.

4.1.3 The S3 set

A final set of atomic and molecular pairs is considered for which experimental geometries and C_6 coefficients are available. All of the dimers of the S1 set are included as well as all combinations of the first 3 rare-gas atoms, together with $(CH_4)_2$, $(Cl_2)_2$, CO_2—

Table 4.6: Mean absolute errors ($|d|$) and mean absolute percentage errors ($|\%d|$) in C_6 coefficients for S2 set. All values in a.u.

		B3LYP	CAM-B3LYP	KT3	B97-1
B3LYP Geometry	$\|d\|$	7.07	5.15	7.75	6.14
	$\|\%d\|$	3.68	2.56	4.28	3.14
CCSD Geometry	$\|d\|$	6.27	6.38	6.70	5.84
	$\|\%d\|$	3.57	2.76	4.10	3.17

CH_4, Cl_2—H_2, Cl_2—CH_4, Cl_2—N_2, Cl_2—CO_2, Cl_2—He, Cl_2—Ne and Cl_2—Ar. The geometries of Cl_2 and CO_2 are taken from Ref. 123. The errors in the C_6 coefficients for this set are shown in table 4.7, where the d-aug-cc-pVTZ basis set has again been used. The strong performance of KT3 for this set can be attributed to the bias of the set towards Cl_2 for which KT3 performs well. CAM-B3LYP again outperforms B3LYP. Over all three test sets, it cannot be said that any functional consistently or significantly outperforms the others, although it can be concluded that CAM-B3LYP generally shows good performance and certainly provides a significant improvement over B3LYP. The lack of a large, well balanced test set for the determination of C_6 coefficients remains a problem.

Table 4.7: Total errors in C_6 coefficients for S3 set. All values in a.u.

	B3LYP	CAM-B3LYP	KT3	B97-1
$\|d\|$	2.40	2.04	1.54	1.95
$\|\%d\|$	4.50	4.38	3.15	3.64

4.1.4 The role of the attenuation parameters in CAM-B3LYP when determining C_6 coefficients

Following the approach of Peach *et al.*,[124] the attenuation parameters in CAM-B3LYP were then varied to find the optimal functional for the determination of C_6 coefficients. For this, the general exchange-correlation functional detailed by Peach *et al.* is used,

$$E_{\mathrm{XC}} = E_{\mathrm{X}}^{\mathrm{SR}} + E_{\mathrm{X}}^{\mathrm{LR}} + E_{\mathrm{C}}^{\mathrm{LYP}}. \tag{4.5}$$

This differs from the original CAM-B3LYP form in that the B3LYP correlation component has been replaced with LYP correlation,

$$E_{\mathrm{XC}}^{\text{CAM-B3LYP}} = E_{\mathrm{X}}^{\mathrm{SR}} + E_{\mathrm{X}}^{\mathrm{LR}} + E_{\mathrm{C}}^{\text{B3LYP}} \tag{4.6}$$

$$E_{\mathrm{C}}^{\text{B3LYP}} = 0.81E_{\mathrm{C}}^{\mathrm{LYP}} + 0.19E_{\mathrm{C}}^{\mathrm{VWN}}. \tag{4.7}$$

The motivation for this change is that, even when the attenuation parameter α (see equation (2.49)) is set to 0.2, the exact functional form of B3LYP cannot be reproduced due to the differing prefactors for the gradient corrected exchange term. Therefore, the justification for using the B3LYP correlation form is lost and it is found[124] that the inclusion of VWN correlation produces poorer performance for atomisation energies. The α and μ parameters are varied in the ranges: $0 \leqslant \alpha \leqslant 0.4$ and $0 \leqslant \mu \leqslant 1$. As well as the original CAM-B3LYP form where $\alpha + \beta = 0.65$, an additional functional form where the exact long-range condition $\alpha + \beta = 1$ is met, is also considered.

The α and μ values are incremented within their ranges by 0.04 and 0.1, respectively. The S1 set is used for this analysis and the same d-aug-cc-pVTZ basis is employed. Mean absolute errors and mean absolute percentage errors are found to give similar outcomes in terms of functional performance. The S1 set is also considered without the inclusion of helium to ensure that its unequal influence does not affect the resulting optimal parameters. The mean absolute error in the C_6 coefficients for the full S1 set as a function of both α and μ for $\alpha + \beta = 0.65$ and $\alpha + \beta = 1$ is shown in figures 4.2(a) and 4.2(b), respectively.

For $\alpha + \beta = 0.65$, the optimal parameters are $\alpha = 0.32$ and $\mu = 0.1\,\mathrm{a}_0^{-1}$, which give a mean absolute error of 1.10 a.u. For $\alpha + \beta = 1$, the optimal parameters are $\alpha = 0.32$ and $\mu = 0\,\mathrm{a}_0^{-1}$, which give a mean absolute error of 1.12 a.u. The error for the standard CAM-B3LYP functional is 1.13 a.u. The optimisation of the attenuating parameters therefore leads to a negligible change in performance.

It is clear from the optimal values of μ that an increase in exchange at long-range is of little importance. Adherence to the exact long-range condition is therefore of little relevance in this case. A higher amount of exact exchange than is included in B3LYP is preferable however, with $\alpha = 0.32$ providing the best results. For both long range conditions shown in figure 4.2, the parameters corresponding to CAM-B3LYP, $\alpha = 0.19$

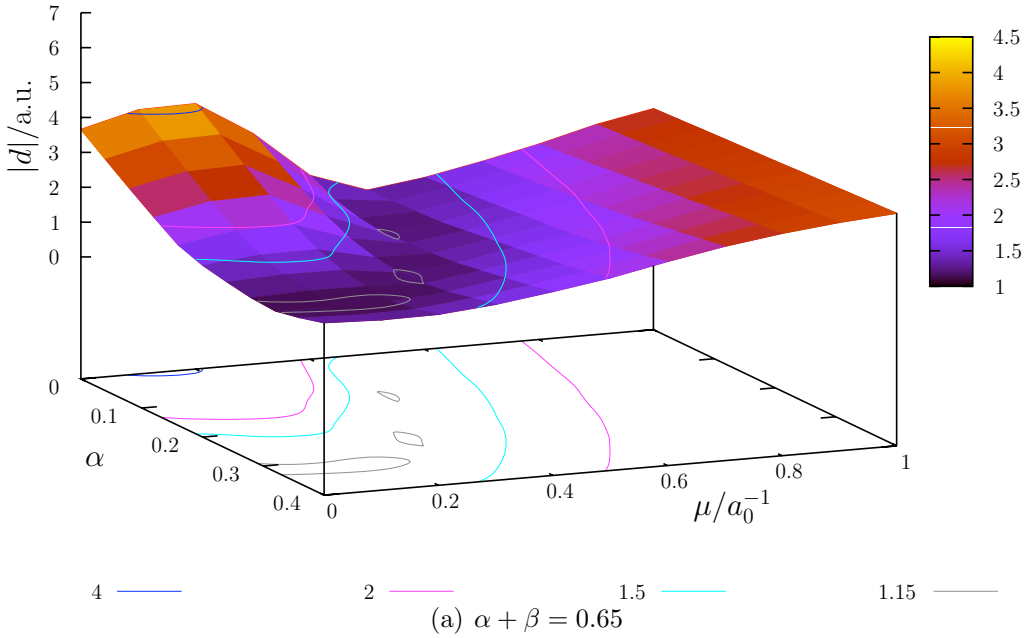

(a) $\alpha + \beta = 0.65$

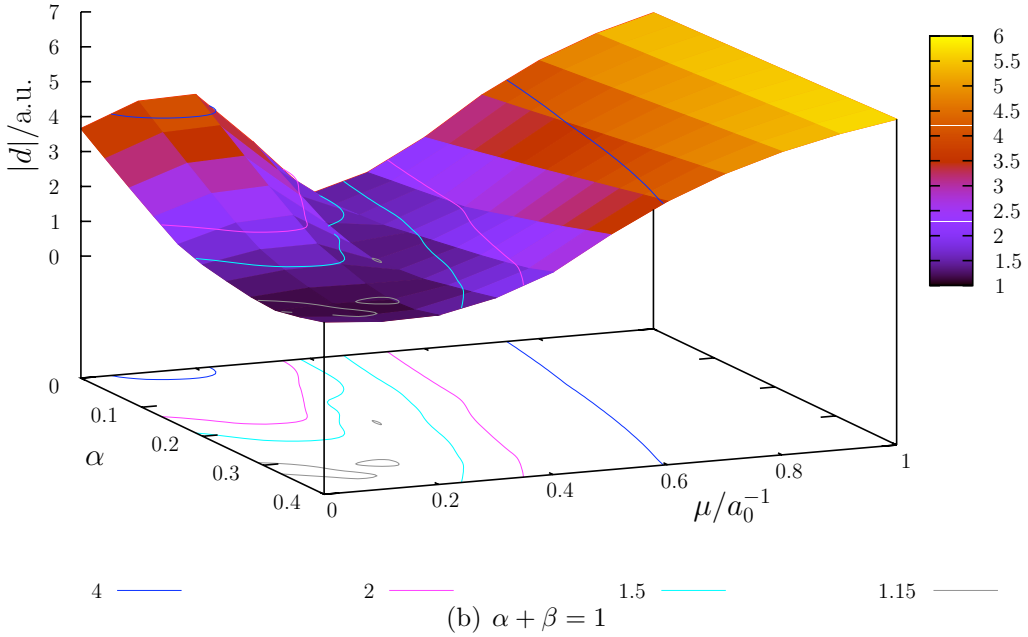

(b) $\alpha + \beta = 1$

Figure 4.2: Mean absolute error in C_6 coefficient for the S1 set.

and $\mu = 0.33\,\mathrm{a}_0^{-1}$ lie within the 'valley' of minimum error results. Large errors for low α values (when μ is also low) reflect the poor performance of local functionals while large errors for high μ values reflect the poor performance of Hartree-Fock.

4.2 Application of DFT to dispersion bound systems: DFT-D

The physics of dispersion, encapsulated in the form of equation (4.1) is not present in local DFT exchange-correlation functionals. We now consider the explicit application of C_6 coefficients to the calculation of dispersion interactions. Specifically, we are interested in the performance of CAM-B3LYP, which has now been shown to produce good C_6 coefficients. Several attempts have been made to rigorously incorporate the form of the dispersion interaction into density functionals.[125–130] The focus of this work is on post-SCF corrections to the DFT energy. Ahlrichs *et al.*[131] supplemented their Hartree-Fock calculations with an explicit dispersion interaction calculated from C_6, C_8 and C_{10} coefficients. This approach of adding a dispersion correction to electronic structure methods was adopted in a QM/MM study of protein structure[132] and an *ab initio* study of methanol dimers.[133] Explicit corrections were added to DFT methods by Elstner *et al.*[134] and Wu *et al.*[135] This latter approach is now widespread and has been termed DFT-D. Of particular importance in this area is the extensive work of Grimme.[103,108,136–142] In the last 10 years there have been numerous investigations which incorporate an explicit post-SCF dispersion correction (DFT-D), many of which[143–146] employ C_6 coefficients determined using the exchange-hole dipole moment method of Becke and Johnson.[109,110,122,147–149] The van der Waals functional of Andersson *et al.*[128] has been combined with long-range corrected functionals[59,150] while Wu and Yang[151] have used a DFT-D method which combines B3LYP and PW91 with dispersion corrections based on experimentally determined C_6 coefficients. Given that the dispersion correction is applied to completed DFT calculations and that the correction itself varies with the internuclear distance R, the DFT-D energy is defined as a function of R as,

$$E_{\text{DFT-D}}(R) = E_{\text{DFT}}(R) + E_{\text{disp}}(R) = E_{\text{DFT}}(R) - C_6 R^{-6} f_{\text{d}}(R). \tag{4.8}$$

This definition is applicable to systems where there is a C_6 coefficient for each entire fragment in the complex. In the case of a rare-gas diatomic the atomic dispersion coefficients are used. For molecular complexes such as the water dimer, a C_6 coefficient for the entire water molecule is required. The damping function $f_{\mathrm{d}}(R)$ is necessary to prevent $E_{\mathrm{disp}} \to \infty$ as $R \to 0$. It therefore acts as a 'switch' between 0 and 1; turning the correction off at short distances to prevent the dispersion correction dominating the intermolecular potential. The form of the damping function plays a critical role in the effect of the dispersion correction; the distance at which it switches between 0 and 1 is important, as well as the rate at which it does so. If the correction is switched on at too short a distance, non-dispersion type bonding will be affected. Two types of damping function are considered. Firstly, the damping function of Mooij *et al.*[131,133] (function I)

$$f_{\mathrm{d}}(R) = \left(1 - \exp\left[-c\left(\frac{R}{R_{\mathrm{m}}}\right)^3\right]\right)^2 \tag{4.9}$$

and secondly a Fermi function[151] (function II)

$$f_{\mathrm{d}}(R) = \frac{1}{1 + \exp\left[-\beta\left(\frac{R}{R_{\mathrm{m}}} - 1\right)\right]}. \tag{4.10}$$

The empirical parameters c and β are determined according to experimental data while R_{m} is the sum of atomic van der Waals radii for the two atoms involved in the interaction. This value is usually taken from the work of Bondi.[152] The difference in the rate of onset and the separation at which this occurs between these two damping functions is illustrated in figure 4.3. Comparison between each of these functions will be employed throughout this chapter.

Much of the following work is concerned with the determination of interaction energies. Basis set superposition error (BSSE) is a problem that arises when calculating interaction energies and is entirely due to the use of a finite basis set. When mapping a potential energy surface, the energy of a diatomic (or more generally, any dimer) is calculated relative to the energy of the two individual, isolated components

$$\Delta E_{\mathrm{AB}} = E_{\mathrm{AB}} - E_{\mathrm{A}} - E_{\mathrm{B}}. \tag{4.11}$$

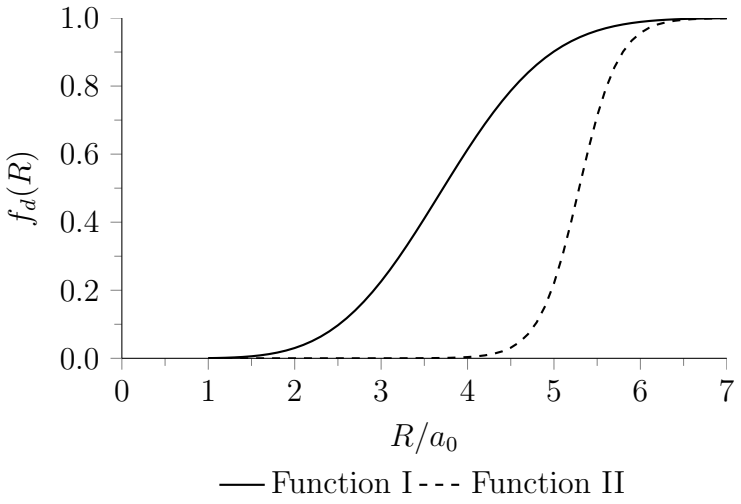

Figure 4.3: A comparison of the shape of the damping functions for the helium atom.

However, this expression omits any information about the basis sets which have been employed. It is illustrative to include them in the expression,

$$\Delta E_{\mathrm{AB}} = E_{\mathrm{AB}}^{\mathrm{ab}} - E_{\mathrm{A}}^{\mathrm{a}} - E_{\mathrm{B}}^{\mathrm{b}} \tag{4.12}$$

where the superscripts refer to the basis set. So, the energy of fragment A is calculated in the basis set 'a', the energy of B in the basis set 'b' and the dimer AB in the joint basis set 'ab', which is a mixture of the two individual basis sets. When calculating the dimer in the joint basis set, the functions of the basis set overlap. Each fragment within the joint basis set therefore benefits from additional basis functions contributed from the overlapping basis set. In other words, the fragment A, within the dimer, experiences a larger basis set than when isolated. Therefore, the energy of the dimer is artificially lowered.

BSSE can be addressed by simply calculating the energy of each fragment in the same combined basis set that is used for the dimer. For atom A, this would be done by placing a *ghost* atom at the position of B, so the basis functions are there, but the atom itself is not. The energy is then

$$\Delta E_{\mathrm{AB}} = E_{\mathrm{AB}}^{\mathrm{ab}} - E_{\mathrm{A}}^{\mathrm{ab}} - E_{\mathrm{B}}^{\mathrm{ab}}. \tag{4.13}$$

Equivalently, a correction term can be added to equation (4.12) which is known as the

counterpoise correction,[153]

$$E_{\mathrm{corr}}^{\mathrm{CP}} = (E_{\mathrm{A}}^{\mathrm{a}} - E_{\mathrm{A}}^{\mathrm{ab}}) + (E_{\mathrm{B}}^{\mathrm{b}} - E_{\mathrm{B}}^{\mathrm{ab}}). \tag{4.14}$$

The application of this correction is equivalent to subtracting out that part of the energy which results from the overlapping of basis functions.

4.2.1 Rare-gas dimers

The diatomic molecules of the rare-gases have been a fertile testing ground for the performance of DFT functionals. Indeed, early efforts to determine whether or not DFT could successfully reproduce dispersion interactions were conducted on diatomics of the rare-gas atoms.[154,155] The dispersion interaction arises from correlation effects: Hartree-Fock gives purely repulsive potentials. Functionals based on the LDA were found to be significantly overbound.[156–159] GGA functionals were found to offer no binding at all. Perez-Jorda and co-workers considered the performance of the LDA, GGA and hybrid functionals[154] as well as a formalism involving a post-HF correlation correction[160] in determining the potential energy curves of rare-gas diatomics.

An appealing aspect of using the rare-gas dimers as a testing ground for the description of the dispersion interaction is the readily available high accuracy reference data. For more than 30 years, accurate C_6 coefficients have been known—largely due to the work of Tang, Toennies and others.[161–164] Also available are highly accurate potential energy curves from the work of Ogilvie and Wang[165,166] and the symmetry-adapted perturbation theory study of Korona *et al.*[96] However, it has recently been suggested[167] that reference data should be taken from the more recent work of Tang and Toennies.[163]

We calculate the interatomic potential energy curves of rare-gas diatomics by following the approach of Wu and Yang, employing equation (4.8) with the damping functions I (equation (4.9)) and II (equation (4.10)). The damping function parameters used are the same as those used by Wu and Yang, namely $c = 3.54$ and $\beta = 23$ and the van der Waals radii of Bondi[152] are used. The potential energies and C_6 coefficients were determined in each case using the d-aug-cc-pV6Z basis set whose extensive size precludes the need to consider basis set superposition error. The resulting DFT-D potential energy curves for B3LYP, CAM-B3LYP, B97-1 and KT3 for each diatomic of the first three

rare gases are presented in figures 4.4 and 4.5.

The more slowly decaying damping function I samples more of the dispersion correction for a larger range of internuclear separation. The resulting potential energy surfaces (figure 4.4) show that the equilibrium bond length is shortened and the dissociation energy is larger, relative to the reference data.[165,166] This behaviour is beneficial for functionals which underbind or offer no binding interaction at all but is likely to over compensate for the dispersion interaction where there is an interaction. With the exception of B3LYP, all functionals with the correction using damping function I underestimate the equilibrium bond length and overestimate the dissociation energy. B3LYP, while giving minima that are too shallow, does offer the best estimate of the bond length. However, it is clear that this damping function is not ideal, given the strength of the dispersion interaction which it applies. It should perhaps be expected that the worst performing DFT method, B3LYP, affords the best DFT-D method although it is unfortunate that any functional which does, to some extent, account for a dispersion interaction, is punished by too strong a correction.

Damping function II produces the potential energy curves plotted in figure 4.5, where a significant improvement in the description of the equilibrium bond length can be seen. All functionals now provide a reasonable description, although B3LYP is again an exception. CAM-B3LYP accurately reproduces the dissociation energy of each diatomic except Ar_2, therefore providing an excellent description of bonding in rare-gas diatomics and significantly outperforming all other functionals considered. The difference between the results for each damping function illustrates the critical role it can play in establishing an effective DFT-D method. The choice of damping function is of comparative importance to the DFT functional and the C_6 coefficients used. Given that the parameters within damping functions are frequently determined from empirical results, this is potentially a cause for concern.

4.2.2 The S22 set

Thus far, the majority of complexes have been small and, while providing significant insight, are of only limited chemical relevance. The set of 22 molecules proposed by Jurecka *et al.*[168] listed in table 4.8 has become the *de facto* standard set of molecules against

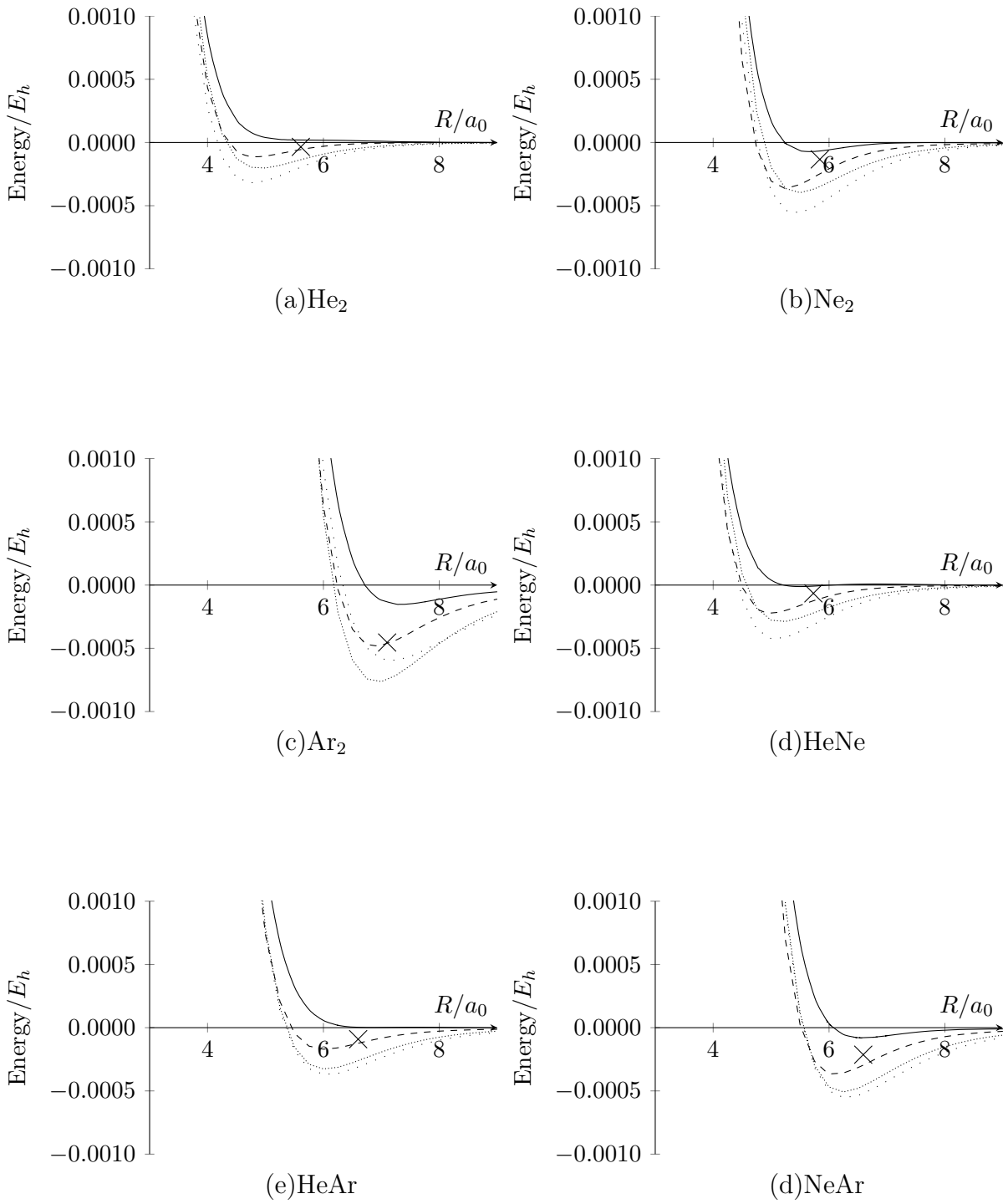

Figure 4.4: Dispersion corrected (function I) potential energy curves for the rare-gas diatomics. B3LYP (solid), CAM-B3LYP (dashed), B97-1 (densely dotted), KT3 (loosely dotted) and Reference (×).

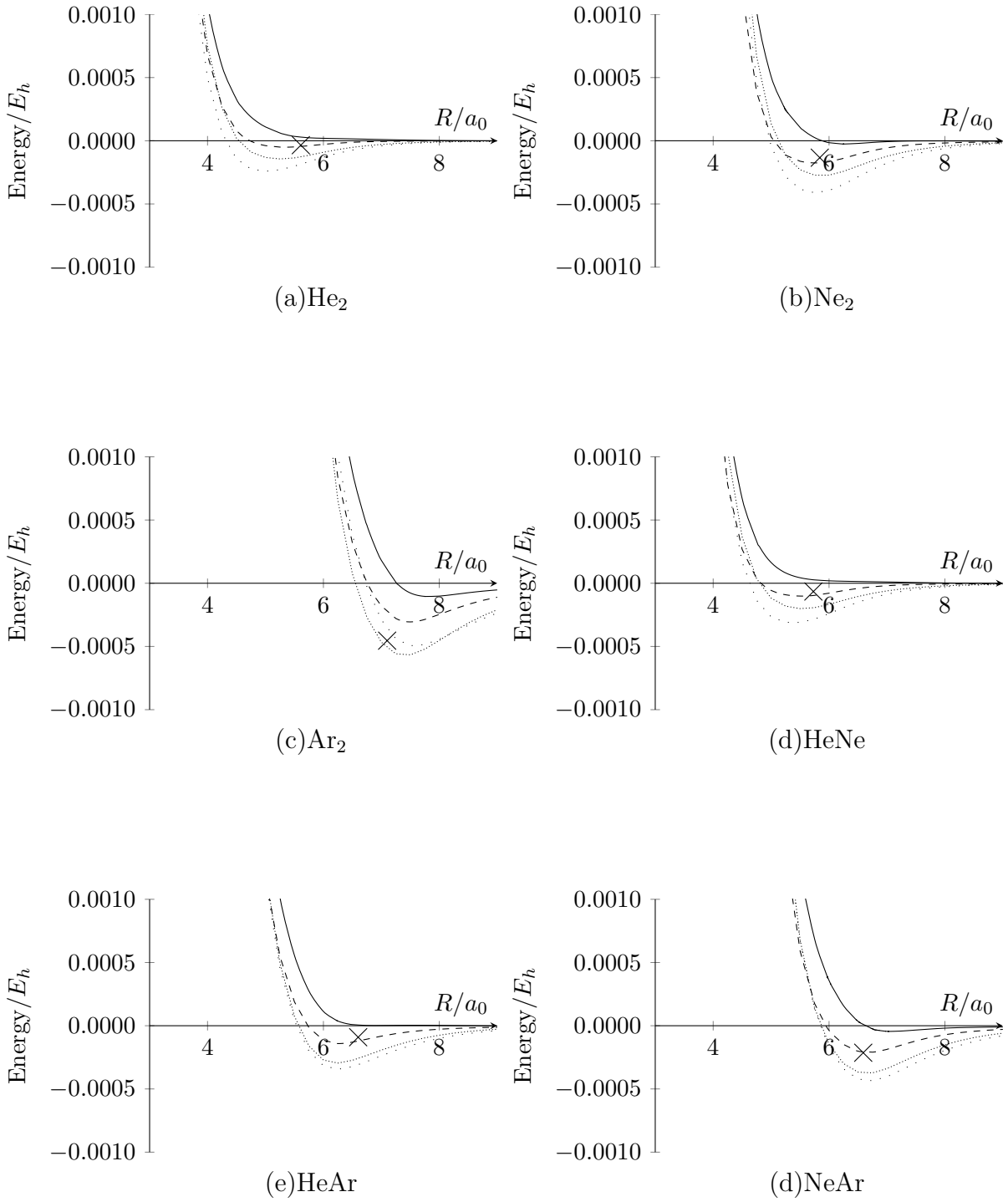

Figure 4.5: Dispersion corrected (function II) potential energy curves for the rare-gas diatomics. B3LYP (solid), CAM-B3LYP (dashed), B97-1 (densely dotted), KT3 (loosely dotted) and Reference (×).

Table 4.8: The complexes of the S22 set and the numbering system used.

Complex	Monomer A	Monomer B	Complex	Monomer A	Monomer B
1	NH_3	NH_3	12	pyrazine	pyrazine
2	H_2O	H_2O	13	uracil	uracil
3	CHO_2H	CHO_2H	14	indole	benzene
4	formamide	formamide	15	adenine	thymine
5	uracil	uracil	16	C_2H_4	C_2H_2
6	pyridoxine	aminopyridine	17	benzene	H_2O
7	adenine	thymine	18	benzene	NH_3
8	CH_4	CH_4	19	benzene	HCN
9	C_2H_4	C_2H_4	20	benzene	benzene
10	benzene	CH_4	21	indole	benzene
11	benzene	benzene	22	phenol	phenol

which to test the performance of theoretical methods at reproducing intermolecular interactions. The set is largely made up of chemically and biologically relevant complexes, some of which are hydrogen bonded, some dispersion bonded and the remainder, mixed complexes. The authors justified the relatively large size of the test set and the inclusion of some of the molecules by noting that the performance of different theories for smaller systems—notably the rare-gas dimers—does not give a good indication of the performance for the dispersion interaction in large molecules. One of the main appeals of the S22 set is the readily available CCSD(T) reference data and optimised geometries.[168] It is therefore pertinent to consider the S22 set in this chapter.

A comprehensive study by Zhao and Truhlar[169] compares the performance of 40 different functionals in determining the interaction energies of the S22 complexes. However, none of the functionals considered are explicitly designed to account for dispersion, nor is a dispersion correction employed at any point. The extensive data in their study is therefore useful only as an assessment of the performance of uncorrected functionals. There are several studies assessing the performance of the dispersion corrected functionals B97-D, PBE-D, BLYP-D and B3LYP-D.[102,103,137,170] The S22 set has been used to test the effectiveness of semi-empirical dispersion corrected methods[171] as well as the exchange-hole dipole moment approach mentioned earlier.[144] The most relevant studies to this work are those involving long-range and dispersion corrected functionals.[172–174] The results of these studies are considered later, in comparison to the results obtained here.

The formulation of the dispersion correction used from now on is more complex than that set out earlier. The dispersion correction between two whole fragments is extended so that it becomes a sum of all pair-wise interactions within each fragment,

$$E_{\text{disp}} = \sum_{i=1} \sum_{j>i} C_6^{ij} R_{ij}^{-6} f_{\text{d}}(R_{ij}). \tag{4.15}$$

Intramolecular dispersion interactions will not be considered here and therefore, the labels i and j correspond to atoms on the two different molecules of the complex considered. Now, the example of the water molecule no longer requires a C_6 coefficient for the entire water molecule, but instead requires individual, atomic coefficients for hydrogen and oxygen; the total dispersion interaction is the sum of 4 hydrogen-hydrogen, 4 oxygen-hydrogen and one oxygen-oxygen atomic dispersion interactions. This approach removes the difficulty in defining an appropriate intermolecular separation between molecules by using each interatomic separation. Wu and Yang[151] used a set of 44 molecular pairs to determine atomic C_6 coefficients. A least squares fitting procedure was used to minimise the difference between calculated and exact molecular dispersion coefficients

$$\sigma = \left[\frac{\sum_i^n (C_6^i(\text{calc})/C_6^i(\text{exact}) - 1)^2}{n} \right]^{\frac{1}{2}}, \tag{4.16}$$

where the value of $C_{6i}(\text{calc})$ is obtained as a sum of all pair-wise atomic interactions between the two fragments. In this approach it is possible to separate atoms according to their hybridisation. To reduce complexity, Wu and Yang used a combination rule to derive C_6 coefficients between unlike atoms from C_6 coefficients between like atoms

$$C_6^{ij} = \frac{2\left((C_6^{ii})^2 (C_6^{jj})^2 N_{\text{eff}}^i N_{\text{eff}}^i\right)^{\frac{1}{3}}}{(C_6^{ii}(N_{\text{eff}}^i)^2)^{\frac{1}{3}} + \left(C_6^{jj}(N_{\text{eff}}^i)^2\right)^{\frac{1}{3}}}. \tag{4.17}$$

We followed this minimisation procedure using the experimental results of Wu and Yang to reproduce their atomic coefficients as a verification of the procedure. The effective number of electrons ($N_{\text{eff}i}$) are set to the same values as used by Wu and Yang. The comparison in table 4.9 shows only slight discrepancies between the values calculated and those presented by Wu and Yang. Also shown are atomic coefficients determined from molecular C_6 coefficients calculated using B3LYP and CAM-B3LYP. For this Wu

Table 4.9: C_6^{ii} coefficients (a.u.) with hybridisation shown in brackets.

i	Wu and Yang	This work	B3LYP	CAM-B3LYP
H	2.83	2.80	2.73	2.74
C (sp^3)	22.24	22.06	22.49	21.79
C (sp^2)	27.76	27.35	28.07	27.45
C (sp)	29.76	30.14	31.51	30.95
N	19.30	19.51	20.11	19.17
O (sp^3)	11.71	11.61	13.12	12.64
O (sp^2)	12.74	12.95	12.12	12.15

and Yang approach, atomic C_6 coefficients are averaged over hybridisation states. The dispersion correction of Grimme will also be considered which includes an additional scaling parameter s_6

$$E_{\text{disp}} = -s_6 \sum_{i=1} \sum_{j>i} C_6^{ij} R_{ij}^{-6} f_{\text{d}}(R_{ij}). \tag{4.18}$$

This parameter scales the entire correction to account for the different behaviour of the intermolecular potential with different functionals.

For each complex in the S22 set, interaction energies are determined as the difference between the sum of the energies of the two isolated fragments and the energy of the complex. At all times, the interaction energies are corrected for BSSE using the procedure outlined in section 4.2. As an initial test, the BLYP-D results of Antony and Grimme[137] were successfully reproduced.

Both B3LYP and CAM-B3LYP were used with the aug-cc-pVTZ basis set and the geometries were taken from the work of Hobza *et al.*[102] The non-dispersion corrected interaction energies are given in table 4.10 and are equivalent to interaction energies with a dispersion correction where the scaling parameter s_6 is set to zero. The B3LYP and CAM-B3LYP interaction energies were then augmented with two different dispersion corrections, both of which involve damping function II (4.10) with $\beta = 20.0$. Firstly, the C_6 coefficients and van der Waals radii from the work of Grimme[108] were used to determine dispersion corrections resulting in "B3LYP-GD" and "CAM-B3LYP-GD". Secondly, for both B3LYP and CAM-B3LYP, molecular C_6 coefficients were determined using the respective functionals, at B3LYP/6-31G(2df,p) optimised geometries. The Wu

and Yang minimisation procedure was then used to determine hybridization-averaged atomic C_6 coefficients which, along with the van der Waals radii of Bondi, were used to give the dispersion corrected values "B3LYP-WYD" and "CAM-B3LYP-WYD". These two types of correction (that due to Grimme and that due to Wu and Yang) are intended to be as similar as possible to the original approaches of Grimme and Wu and Yang, respectively. Therefore, when the Grimme approach is used, the same correction is applied to both B3LYP and CAM-B3LYP whereas in the second approach, each functional is used to determine the C_6 coefficients and interaction energies. The C_6 coefficients were determined using d-aug-cc-pVDZ as test calculations showed that, while diffuse functions were beneficial, functions of higher angular momentum had little effect. Table 4.10 presents the dispersion corrections determined with both approaches. Table 4.11 presents the dispersion corrected interaction energies according to the schemes outlined as well as reference CCSD(T) data taken from the original work of Jurecka *et al.*[168]

The uncorrected interaction energies give a clear picture of the failure of DFT to deal with dispersion bound complexes. B3LYP fails to bind 8 out of the 22 complexes, while CAM-B3LYP also has difficulty, failing to bind 5 complexes. The need for a binding dispersion correction is clear as B3LYP underbinds all of the complexes. Similarly, CAM-B3LYP underbinds all but complexes 2 and 3, which are overbound by 0.12 and 0.72 kcal/mol. Mean absolute errors for the S22 set are shown in table 4.12.

The mean absolute error for uncorrected ($s_6 = 0$) interaction energies determined with B3LYP and CAM-B3LYP are 3.96 and 2.66 kcal/mol respectively. The Wu and Yang fitting procedure yields almost identical corrections for both B3LYP and CAM-B3LYP although these are both generally much weaker corrections than those calculated through Grimme's approach. For each of the dispersion corrected interaction energies presented in table 4.11, the dispersion correction has been applied with the s_6 scaling parameter set to 1. Although a value of $s_6 = 1.05$ has been previously established for B3LYP-GD and it is now in common use, we find that using $s_6 = 1.00$ yields very slightly improved interaction energies. B3LYP-GD overbinds 16 of the complexes while CAM-B3LYP-GD overbinds them all. Given that uncorrected B3LYP interaction energies are uniformly very underbound, the application of a strong dispersion correction is beneficial and the mean absolute error for B3LYP-GD (0.42 kcal/mol) is significantly better than that for CAM-B3LYP-GD (1.42 kcal/mol). The weaker corrections from the Wu and

Table 4.10: B3LYP and CAM-B3LYP interaction energies (kcal/mol) and Grimme, B3LYP (WY) and CAM-B3LYP (WY) dispersion corrections (kcal/mol) for the S22 set.

	Interaction energies		Dispersion corrections		
Complex	B3LYP	CAM-B3LYP	Grimme	B3LYP (WY)	CAM-B3LYP (WY)
1	−2.15	−2.76	−1.39	−0.64	−0.63
2	−4.41	−5.14	−0.78	−0.52	−0.51
3	−17.21	−19.33	−2.51	−1.39	−1.37
4	−13.90	−15.59	−2.66	−1.68	−1.64
5	−17.80	−19.60	−3.33	−2.30	−2.24
6	−13.67	−15.21	−3.97	−2.88	−2.81
7	−12.73	−14.46	−4.24	−3.20	−3.12
8	0.39	0.06	−0.83	−0.86	−0.86
9	0.52	−0.24	−2.14	−1.94	−1.92
10	0.80	0.10	−2.18	−1.84	−1.82
11	3.76	2.30	−5.72	−4.94	−4.86
12	2.51	0.81	−6.21	−5.00	−4.87
13	−0.85	−3.41	−9.01	−7.18	−7.01
14	4.68	2.62	−8.53	−7.09	−6.95
15	1.40	−2.10	−13.22	−10.31	−10.04
16	−0.64	−0.97	−1.00	−0.75	−0.74
17	−1.16	−2.00	−2.34	−1.66	−1.64
18	−0.07	−0.84	−2.28	−1.78	−1.75
19	−1.94	−3.00	−3.10	−1.72	−1.69
20	1.02	−0.01	−3.65	−2.69	−2.64
21	−0.48	−1.90	−5.30	−3.66	−3.59
22	−2.87	−4.45	−4.08	−3.28	−3.24

Table 4.11: Interaction energies (kcal/mol) determined using dispersion corrected DFT. In all cases, $s_6 = 1.00$. CAM-B3LYP is shortened to "CAM".

Complex	B3LYP-GD	B3LYP-WYD	CAM-GD	CAM-WYD	CCSD(T)[a]
1	−3.54	−2.79	−4.15	−3.39	−3.17
2	−5.19	−4.93	−5.91	−5.65	−5.46
3	−19.73	−18.61	−21.84	−20.70	−21.60
4	−16.56	−15.58	−18.25	−17.24	−17.69
5	−21.13	−20.09	−22.93	−21.84	−22.82
6	−17.64	−16.55	−19.18	−18.02	−18.60
7	−16.96	−15.92	−18.70	−17.58	−18.12
8	−0.44	−0.47	−0.77	−0.80	−0.49
9	−1.62	−1.41	−2.38	−2.16	−1.55
10	−1.38	−1.04	−2.08	−1.72	−1.76
11	−1.96	−1.18	−3.41	−2.55	−4.24
12	−3.70	−2.49	−5.40	−4.06	−6.04
13	−9.87	−8.04	−12.42	−10.41	−11.95
14	−3.85	−2.41	−5.91	−4.33	−6.96
15	−11.82	−8.91	−15.32	−12.41	−14.71
16	−1.64	−1.39	−1.97	−1.71	−1.76
17	−3.50	−2.82	−4.34	−3.64	−3.70
18	−2.35	−1.86	−3.12	−2.59	−2.66
19	−5.04	−3.66	−6.09	−4.68	−5.48
20	−2.63	−1.67	−3.65	−2.65	−3.49
21	−5.79	−4.14	−7.20	−5.49	−6.84
22	−6.95	−6.15	−8.54	−7.69	−8.09

[a]Ref 168

Yang procedure do little to solve the underbinding problem experienced with B3LYP, with all compounds remaining underbound, whereas their application to CAM-B3LYP produces a notable improvement. The mean absolute error for CAM-B3LYP-WYD (0.58 kcal/mol) is much lower than for B3LYP-WYD (0.90 kcal/mol).

Following Grimme's optimisation of the s_6 parameters for a number of functionals using a set of 40 noncovalently bound complexes,[108] we use our results to determine optimised s_6 values for each of the dispersion adjusted approaches considered. The optimal s_6 values for B3LYP-GD and B3LYP-WYD are 1.03 and 1.31, respectively, reflecting the tendency of B3LYP to produce an intermolecular potential which is underbound. It also highlights the fact that the Grimme correction is larger than the one obtained from the Wu and Yang procedure. For CAM-B3LYP-GD and CAM-B3LYP-WYD, the optimal s_6 values are 0.74 and 0.96, respectively, showing that CAM-B3LYP generally requires a smaller correction to account for dispersion. The mean absolute errors associated with these s_6 values are also shown in table 4.12. For B3LYP-WYD, which underbinds all of the complexes, the optimisation of the s_6 parameters gives a significant improvement. Also, for CAM-B3LYP-GD, which overbinds to a greater extent than CAM-B3LYP-WYD, optimisation also produces a reduction in error. However, it is the uniform underestimation of the interaction energy by B3LYP-WYD which means it produces the lowest error for an optimised s_6 parameter. Therefore, the superior performance of B3LYP-WYD is only a product of the systematic underestimation of B3LYP.

Table 4.13 provides a comparison of the best performing CAM-B3LYP based functional from this study (DFT C_6 coefficients (WY)/$s_6 = 0.96$) and the results of other functionals taken from the literature. Rather than using the data for the best performing B3LYP-D functional from this study, the errors listed in the table are when using Grimme's dispersion correction with $s_6 = 1.05$ as this method is now established. It can be seen that CAM-B3LYP-WYD does not offer any improvement in performance over other dispersion corrected functionals. The long-range and dispersion corrected ωB97X-D functional does provide the best performance but only shows a mean absolute error 0.04 kcal/mol improvement over the best performing B3LYP-WYD functional.

Table 4.12: Mean absolute errors in the interaction energy (kcal/mol) for the S22 set when using different s_6 scaling parameters.

s_6	0.00	1.00	optimised
B3LYP-GD	3.96	0.42	0.40
B3LYP-WYD	3.96	0.90	0.26
CAM-B3LYP-GD	2.66	1.44	0.70
CAM-B3LYP-WYD	2.66	0.58	0.58

Table 4.13: A comparison of mean and absolute mean errors in the interaction energy (kcal/mol) for a number of dispersion corrected functionals.

Theory	d	$\|d\|$
B97-D[a]	0.44	0.50
BLYP-D[a]	0.22	0.33
B3LYP-D[a]	-0.28	0.48
CAM-B3LYP-WYD	0.29	0.58
ωB97X-D[a]	-0.08	0.22
LC-BOP+ALL[b]	0.22	0.46

[a]Ref 173
[b]Ref 172

4.2.3 The role of the attenuation parameters in CAM-B3LYP-D

The approach taken in section 4.1.4 of systematically varying the parameters of the CAM-B3LYP functional was then employed to determine the optimal dispersion corrected functional for describing the interaction energies of hydrogen and dispersion bound complexes. For this, the dimers of helium, neon, water, ammonia, methanol, formamide, methane and ethane were chosen as a representative set. For each functional, defined by the choice of α and μ (equation (2.49)), the 8 interaction energies were determined. A dispersion correction was then applied to the interaction energy of each complex and the s_6 parameter optimised so as to produce the minimum mean absolute error for that particular functional with the 8 complexes.

To avoid the laborious task of determining the counterpoise correction for each functional, the same correction for each complex was uniformly applied across the full range of functionals. This is justified as the BSSE is a product of the incompleteness of the basis set rather than a shortcoming of the functional used. The correction applied to all

functionals was determined using B3LYP. The Grimme dispersion correction was also used for every functional. The same geometries of Jurecka *et al.*[168] from the S22 set were used. As before, the two conditions considered were $\alpha + \beta = 0.65$ and $\alpha + \beta = 1$. For each functional, as well as an optimised value, an s_6 value of zero and one was considered. Plots of the mean absolute error as a function of the parameters are given in figures 4.6 and 4.7. Care should be taken as, in each figure, the final plot corresponding to an optimised s_6 value is plotted on a smaller scale than in the preceding two plots because the flatness of the surface on a larger scale makes it difficult to identify the relevant features.

Figure 4.6: Mean absolute error $|d|$ in dispersion corrected interaction energy under variation of α and μ under the condition of $\alpha + \beta = 0.65$. (a) $s_6 = 0$, (b) $s_6 = 1$ and (c) s_6 optimised at each point.

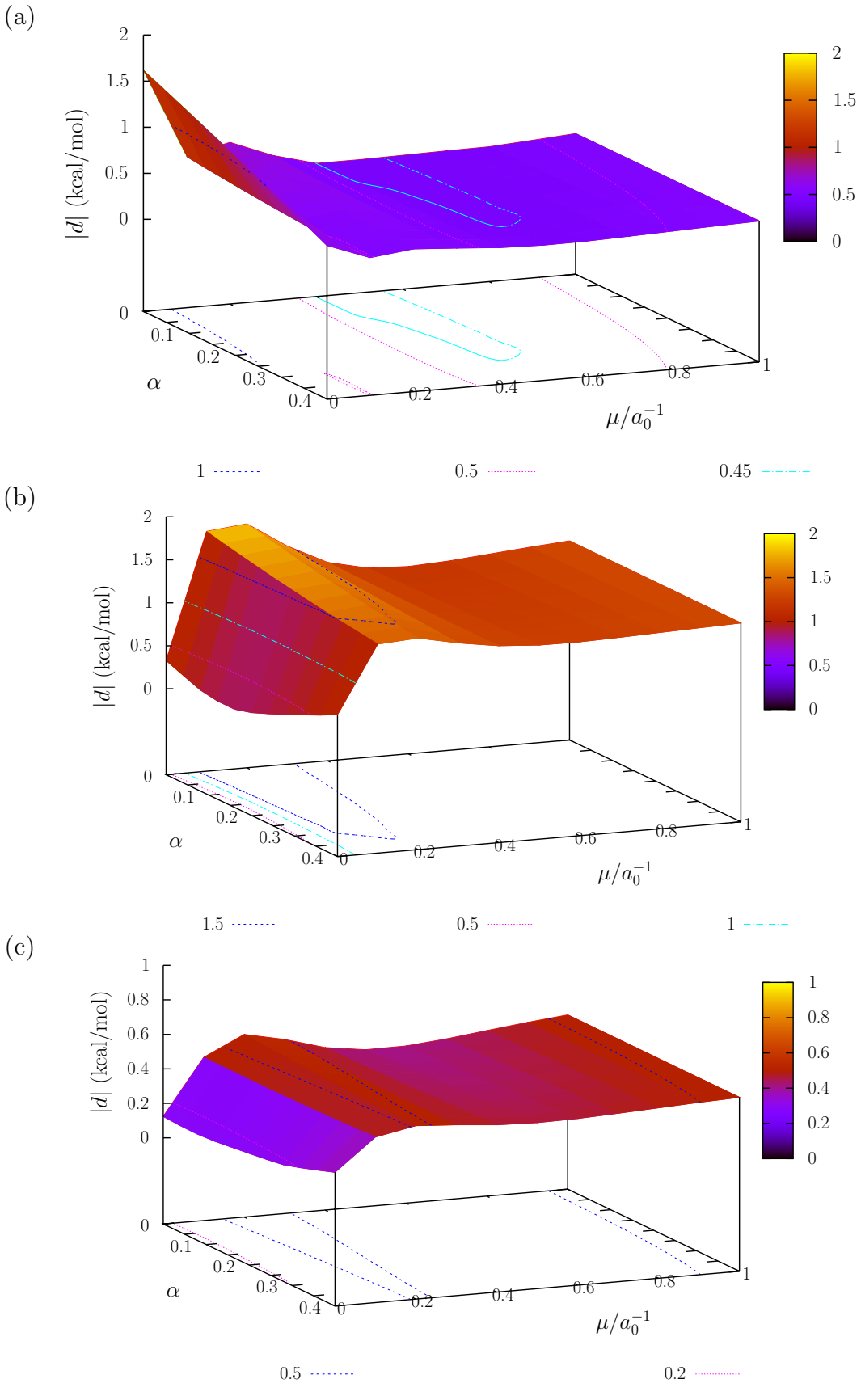

Table 4.14: BSSE Corrected Errors (kcal/mol) for the S22 subset with the α, β and μ parameters set to reproduce functionals which are most similar to BLYP, B3LYP and CAM-B3LYP.

	$s_6 = 0$		$s_6 = 1$		$s_6 = opt$	
	Error	Abs Error	Error	Abs Error	Error	Abs Error
BLYP	1.62	1.62	0.33	0.33	0.04	0.12
B3LYP	1.16	1.16	−0.13	0.20	0.01	0.15
CAM-B3LYP	−0.12	0.53	−1.40	1.44	0.10	0.49
CAM($\alpha + \beta = 0.65$)	0.10	0.45	−0.03	0.14	−0.01	0.12
CAM($\alpha + \beta = 1$)	0.67	0.67	−0.03	0.14	−0.01	0.12

For both $\alpha + \beta = 0.65$ and $\alpha + \beta = 1$, the same general trend is seen when using the three different s_6 parameters. When no correction is applied, the error surface is generally flat for values of $\mu \geq 0.2$. Applying a uniform correction with $s_6 = 1$ dramatically reduces the quality of the results for $\mu \geq 0.1$. The uncorrected interaction energies for the functionals in this range are reasonable and therefore, applying a standard correction will be of little benefit. In a similar way, the poor results for $\mu = 0.0$ do benefit from the application of the correction. As expected, the added flexibility of optimising the s_6 parameter for every functional produces error surfaces which are low in magnitude and relatively flat compared to non-optimised values. The overall outcome is that, when applying a correction, functionals with $\mu = 0.0$ perform best, which can be traced to their systematic underestimation of the interaction energy when no correction is applied.

Table 4.14 shows a comparison between the optimal CAM($\alpha + \beta = 0.65$) and CAM($\alpha + \beta = 1$) functionals and those functionals whose parameters most closely resemble the form of BLYP, B3LYP and CAM-B3LYP. BLYP is obtained exactly when $\alpha = 0$ and $\mu = 0$ a_0^{-1}. B3LYP is most closely achieved with $\alpha = 0.2$ and $\mu = 0$ a_0^{-1} and CAM-B3LYP with $\alpha = 0.2$, $\alpha + \beta = 0.65$ and $\mu = 0.3$ a_0^{-1}. B3LYP is not obtained exactly with these parameters as a different correlation form is being used, as defined in equation (4.5). BLYP and B3LYP underbind all 8 complexes and therefore benefit from the application of a dispersion correction. The optimisation of the s_6 parameter further reduces the error. Although CAM-B3LYP performs significantly better than both BLYP and B3LYP in the absence of a correction, its tendency to neither over- nor

Figure 4.7: Mean absolute error $|d|$ in dispersion corrected interaction energy under variation of α and μ under the condition of $\alpha + \beta = 1.00$. (a) $s_6 = 0$, (b) $s_6 = 1$ and (c) s_6 optimised at each point.

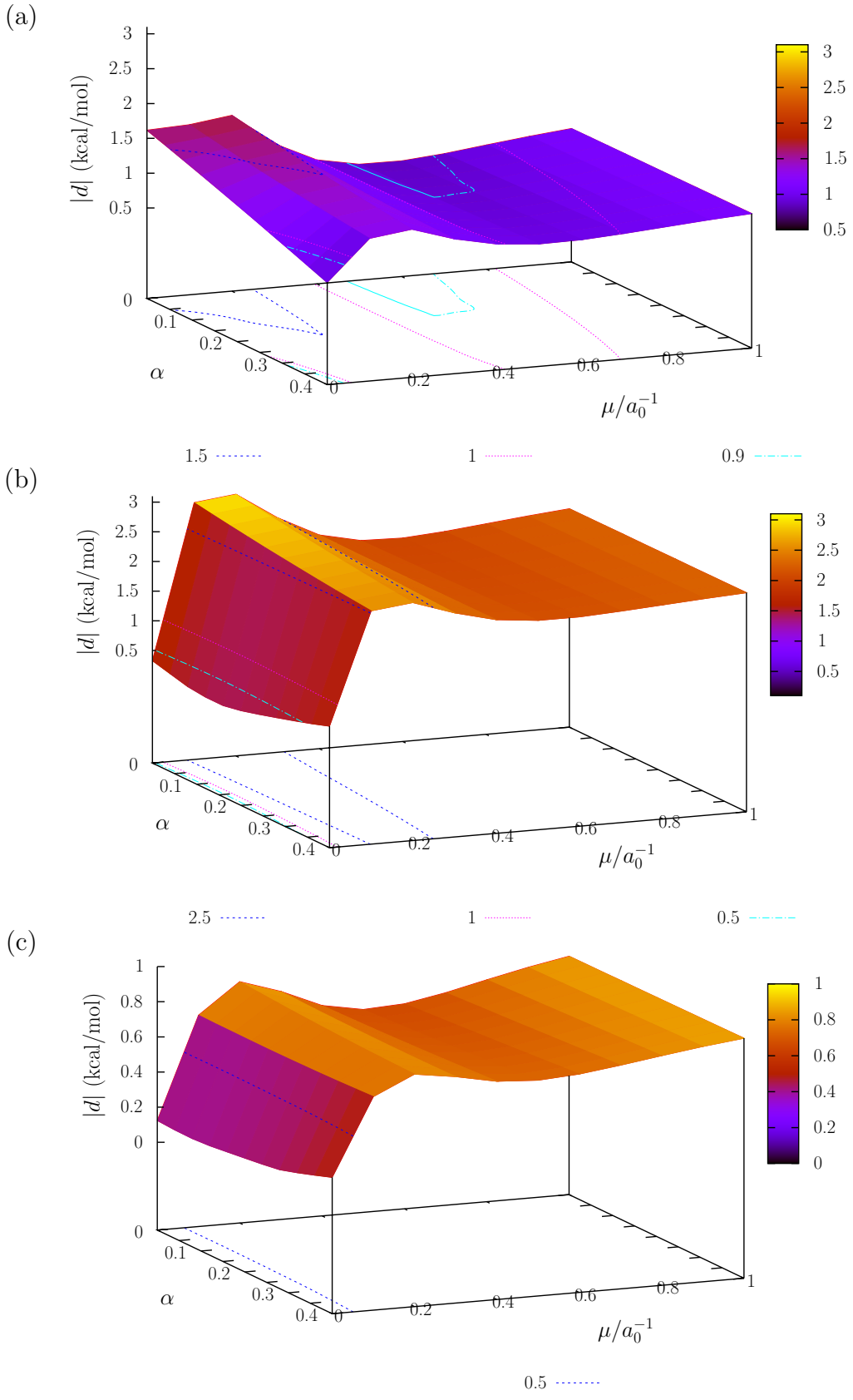

Table 4.15: α and μ (a_0^{-1}) values for optimum functionals under different s_6 conditions.

		$s_6 = 0$	$s_6 = 1$	s_6=opt
CAM($\alpha + \beta = 0.65$)	α	0.16	0.16	0.08
	μ	0.50	0.00	0.00
CAM($\alpha + \beta = 1$)	α	0.40	0.16	0.08
	μ	0.00	0.00	0.00

under-bind more frequently means that it suffers when a uniform correction is added. Interestingly, an optimised s_6 value does not offer any significant improvement over the uncorrected form of CAM-B3LYP, indicating that it is not a good candidate for dispersion correction.

Summary

Over the three test sets considered for the determination of C_6 dispersion coefficients, no single exchange-correlation functional showed a sustained superior performance over any of the others. CAM-B3LYP produced an all round good performance, showing a particularly significant improvement over B3LYP. Through the variation of the attenuation parameters, the poor performance of local functionals (low α/low μ) and Hartree-Fock (high μ) is highlighted. The originally determined attenuation parameters in CAM-B3LYP provide a generally good performance compared to other, differently attenuated varieties.

The application of an empirical post-SCF dispersion coefficient within the DFT-D framework is influenced significantly through the choice of an appropriate damping function. Additional parameters, such as the s_6 coefficient introduced by Grimme, add further flexibility to the effect of the dispersion correction. The importance of correctly selecting appropriate coefficients and damping function can be considered as important as being able to produce accurate C_6 coefficients or even accurate interaction energies. With this in mind, dispersion corrected CAM-B3LYP provides an excellent description of the intermolecular potential energy curves of the rare-gas dimers. For the S22 set, its performance is comparable to other optimised GGA, hybrid and long-range corrected functionals.

Chapter 5

Excited States of organic molecules

A number of applications of time-dependent density functional theory (TDDFT) to problems in organic chemistry are investigated. The validity of the comparison between theoretically determined and experimentally observed excitation energies is considered through an extensive investigation of pyrene and some of its derivatives. The extent to which different substituents influence the excitation energies is assessed. CAM-B3LYP provides an excellent description of the relevant excited states as well as removing erroneous low-lying charge transfer states present when using B3LYP.

The ability of TDDFT to correctly describe the formation of organic excimers is investigated, where it is shown that exact long-range exchange is necessary for a correct description. CAM-B3LYP provides a description of comparable accuracy to the BH-HLYP functional, whose good performance has been previously demonstrated.

5.1 Pyrene and its derivatives

5.1.1 The comparison of $\Delta E_{\mathbf{vert}}$ and $\lambda_{\mathbf{max}}$

The ability to accurately calculate excitation energies through the use of time-dependent density functional theory (TDDFT) is of critical importance for comparison with experimental work. It can be used to predict experimental spectra, be used as an aid in understanding experiment and provide theoretical insight into any process occuring. The calculation of vertical excitation energies from the equilibrium geometry of the ground state potential energy surface to the excited state potential energy surface is

equivalent to the determination of absorption spectra. However, comparing the results from absorption spectra with vertical excitation energies has subtle complications.

Experimentally, electronic transitions occur between particular vibrational levels of two different electronic states. It is possible for an electronic transition to have vibrational fine structure due to excitation from one vibrational state in the lower electronic state into a series of vibrational states in the upper electronic state. These manifest themselves in experimental spectra as a series of absorption bands and it is the one of maximum intensity that is denoted $\lambda_{\max}$. The theoretically determined vertical excitation energy neglects any vibrational issues and determines simply the vertical difference of the two electronic potential energy surfaces at a particular geometry. TDDFT also neglects the zero point energy. The vertical excitation energy is therefore only an approximation to the observed experimental excitation.

To determine the discrepancy between theoretical ΔE_{vert} and experimental $\lambda_{\max}$ values, it is necessary to do a full vibrational analysis on the system of interest, allowing the theoretical determination of $\lambda_{\max}$. Such an analysis has been performed by Dierksen and Grimme[175] for a range of organic molecules including several polycyclic aromatic hydrocarbons (PAHs). The intensity of a transition between initial (εv) and final ($\varepsilon' v'$) vibronic states is proportional to the square of the transition dipole

$$\mu_{\varepsilon' v', \varepsilon v} = \langle \varepsilon' v' | \, \hat{\mu} \, | \varepsilon v \rangle \, . \tag{5.1}$$

The dipole moment operator, $\hat{\mu}$ depends on the locations and charges of the electrons, $\mathbf{r}_i$ and $-e$, and the locations and charges of the nuclei, $\mathbf{R}_{\text{N}}$ and Z_{N}

$$\hat{\mu} = -e \sum_i \mathbf{r}_i + e \sum_N Z_{\text{N}} \mathbf{R}_{\text{N}} = \hat{\mu}_{\text{e}} + \hat{\mu}_{\text{N}}. \tag{5.2}$$

The transition dipole is therefore

$$\langle \varepsilon' v' | \, \hat{\mu} \, | \varepsilon v \rangle = \langle \varepsilon' v' | \, \hat{\mu}_{\text{e}} + \hat{\mu}_{\text{N}} \, | \varepsilon v \rangle \tag{5.3}$$

$$= \langle v' | \, \mu_{\varepsilon' \varepsilon} \, | v \rangle \, . \tag{5.4}$$

where $\mu_{\varepsilon' \varepsilon}$ is the electronic transition dipole moment, which can be expanded as a Taylor series around the equilibrium geometry, in terms of the vibrational normal coordinates

Q_i,

$$\mu_{\varepsilon'\varepsilon} = (\mu_{\varepsilon'\varepsilon})_{\text{eq}} + \sum_i \left(\frac{\partial \mu_{\varepsilon'\varepsilon}}{\partial Q_i}\right)_{\text{eq}} Q_i + \cdots . \tag{5.5}$$

The FC approximation amounts to truncating this at the first term, which allows for transitions that are dipole-allowed. Truncation at the second term (FCHT) allows for transitions where the electron transition dipole changes. For dipole-forbidden transitions where $\mu_{\varepsilon'\varepsilon} = 0$, the first term is zero and we have the HT approximation. Any intensity for a transition which has an electronic transition dipole moment of zero arises from transitions involving a change in the nuclear coordinates. The description of dipole-allowed, weakly dipole-allowed and dipole forbidden transitions can therefore be achieved through the Franck-Condon (FC), Franck-Condon-Herzberg-Teller (FCHT) and Herzberg-Teller (HT) approximations,[176–179] respectively. To account for each type of transition, Dierksen and Grimme calculated the vibrational normal modes of both the ground and excited states. This allowed them to quantify the difference between ΔE_{vert} and λ_{max} for a series of molecules. They concluded that once this discrepancy had been accounted for, the TDDFT approach is superior to other theoretical methods for determining excitation energies. Of specific relevance to the current work was their findings with regard to pyrene. Their results will be discussed in the following section as a precursor to our own study.

5.1.2 TDDFT Studies on Pyrene

The long fluorescence lifetime of pyrene (figure 5.1) and its ability to form fluorescent excimers gives pyrene specific chemical interest. The ability to tune the behaviour of pyrene with numerous substituents has led to a wide range of uses across chemistry and biochemistry. Derivatives of pyrene have been used to create OLEDs capable of emitting over the full visible range.[180–182] The sensitivity of the fluorescence behaviour to changes in the environment allow it to be used as a probe; specifically, pyrene-1-butyric acid can be used to determine oxygen concentrations in biological systems.[183,184] Pyrene readily forms excimers (see section 5.2) at sufficient concentrations in solution, allowing investigation of excimer behaviour as well as finding further uses in the detection of specific substrates.[185]

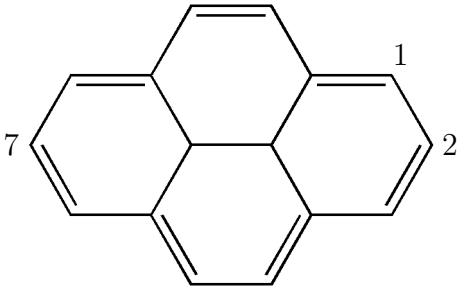

Figure 5.1: The structure of pyrene, showing the numbering used for the locations of substitution.

Table 5.1: The first two experimental and DFT excitation energies (eV) of pyrene.[a]

	$\Delta E_{\text{vert}}^{\text{calc}}$	$\Delta E_{0-0}^{\text{calc}}$	$\Delta E_{0-0}^{\text{obs}}$	$\Delta E_{\text{vert}} - \Delta E_{0-0}^{\text{calc}}$
L_a	3.69	3.42	3.84	0.27
L_b	3.76	3.57	3.36	0.19

[a]Ref. 175

Dierksen and Grimme[175] showed that in the case of pyrene, λ_{max} is the same as $\Delta E_{0-0}^{\text{obs}}$, the transition from the ground vibrational level of the initial electronic state to the ground vibrational level of the final electronic state. The notation ΔE_{0-0} will be used with superscripts to differentiate between experimentally observed (obs) and theoretically calculated (calc) values. Using the Platt[186,187] nomenclature, there are two states of interest in pyrene: $L_b(S_1 \leftarrow S_0)$ and $L_a(S_2 \leftarrow S_0)$, which are denoted as covalent and ionic in character respectively. This nomenclature is based upon the symmetry of the orbitals involved in each transition. For pyrene (D_{2h}), these states correspond to $(b_{1g} \rightarrow b_{3u}) - (b_{2g} \rightarrow a_u)(L_b)$ and $b_{1g} \rightarrow a_u(L_a)$ transitions, respectively. Figure 5.2 shows the dominant orbital transitions involved in these two states.

The TDDFT-B3LYP/TZVP results of the vibrational analysis conducted by Dierksen and Grimme are summarised in table 5.1. The commonly made comparison is between the TDDFT vertical excitation energy $\Delta E_{\text{vert}}^{\text{calc}}$ and the experimentally observed value $\Delta E_{0-0}^{\text{obs}}$ ($\equiv \lambda_{\text{max}}$). The $\Delta E_{0-0}^{\text{calc}}$ are those determined by Dierksen and Grimme which can be directly compared with $\Delta E_{0-0}^{\text{obs}}$. For the dipole-allowed L_a state $\Delta E_{\text{vert}}^{\text{calc}}$ overestimates $\Delta E_{0-0}^{\text{calc}}$ by 0.27 eV. However, $\Delta E_{0-0}^{\text{calc}}$ underestimates the experimental value by 0.42 eV. The overestimation introduced by using ΔE_{vert} rather than the 0-0 value is, to a large extent, reduced by the underestimation of the excited state. The reasonably good

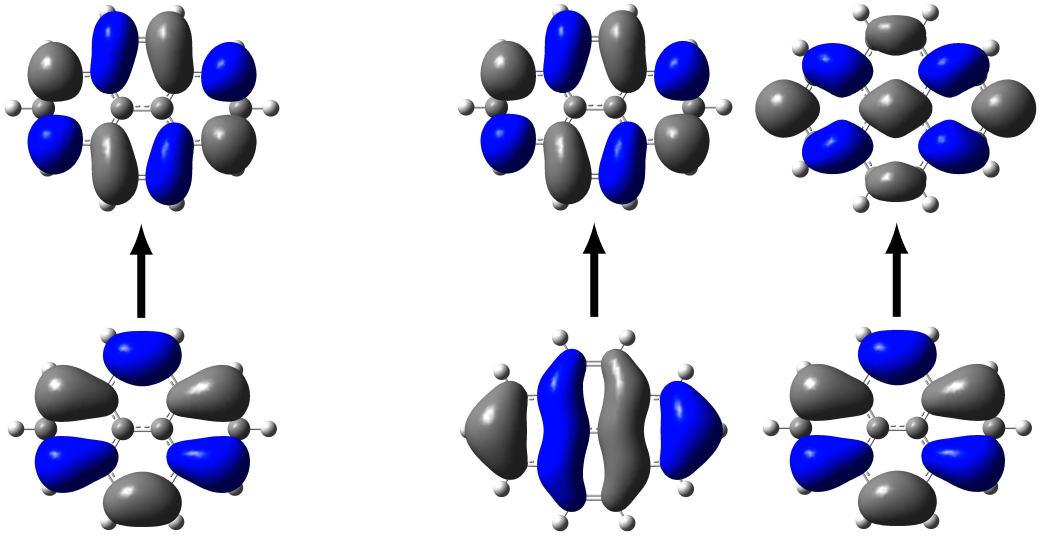

Figure 5.2: The dominant orbital transitions in the (a) L_a and (b) L_b states of pyrene.

performance of B3LYP for the L_a state is, therefore a result of a *fortuitous cancellation of errors*. The same analysis for the weakly dipole-allowed L_b state shows that $\Delta E^{\text{calc}}_{\text{vert}}$ overestimates the calculated $\Delta E^{\text{calc}}_{0-0}$, which in turn represents an overestimation of the actual observed value, $\Delta E^{\text{obs}}_{0-0}$, making the TDDFT values a poor approximation to the observed values. The cancellation of errors seen for the L_a state is not present here. On the basis of these findings, it is possible to propose a correction to calculated $\Delta E^{\text{calc}}_{\text{vert}}$ values so that they are directly comparable with experimentally observed spectra. In the case of pyrene (B3LYP/TZVP) the correction ($\Delta E^{\text{calc}}_{\text{vert}} - \Delta E^{\text{calc}}_{0-0}$) amounts to 0.27 eV and 0.19 eV for the L_a and L_b states, respectively.

The underestimation of the L_a excited state by B3LYP, which is apparent from a comparison of $\Delta E^{\text{calc}}_{0-0}$ and $\Delta E^{\text{obs}}_{0-0}$, is usually attributed to its ionic character.[188] In the same way that charge-transfer excitations are incorrectly underestimated using conventional DFT functionals, ionic states of PAHs are also underestimated. A study by Parac and Grimme[189] found that for PAHs, as the size of the system increases, the L_a state becomes increasingly underestimated, while the accuracy in the prediction of the L_b state remains almost constant, when using conventional hybrid functionals. The result of this difference in accuracy for the two states is that no DFT study to date has been able to correctly reproduce the ordering of the lowest excited states of the pyrene molecule. Specific failures have been illustrated for BP86, B3LYP and BH-HLYP.[189,190] It should,

however, be noted that an increasing proportion of exact exchange in hybrid functionals does improve performance.[190]

Having established the current failings of TDDFT treatments of pyrene, we now turn to a more extensive consideration of pyrene and pyrene derivatives with particular chemical interest. For this, we assess the performance of CAM-B3LYP in comparison to B3LYP. Firstly, we consider unsubstituted pyrene. We then move on to consider derivatives of pyrene that have been substituted in the 2-position, the 2,7-positions and finally the 1-position. The numbering of the substitution sites is shown in figure 5.1. The structures of all of the pyrene derivatives studied are shown in figure 5.3. The Mes group is 1,3,5-trimethylbenzene. This work has been done in collaboration with the experimental work of the Prof. Marder group who provided experimental results.

In light of the discussion concerning the non-trivial nature of comparing between theory and experiment, we are principally concerned with trends and the focus is in comparing the B3LYP/CAM-B3LYP results for substituted pyrene derivatives with B3LYP/CAM-B3LYP results for unsubstituted pyrene. There is then a comparison between the two functionals and a consideration of the accuracy of the results with respect to those observed experimentally. It should be noted that the labels L_a and L_b are sometimes used loosely to indicate a state which involves an orbital transition similar to that observed in unsubstituted pyrene. It may also be the case that, due to symmetry-breaking, the excitation does not formally correspond to this label. All structures were optimised at the B3LYP/6-31G(d) level using GAUSSIAN03[191] and then verified to be minima by calculating the vibrational frequencies. All TDDFT excitation energies were determined using DALTON[98] with both the B3LYP and CAM-B3LYP functionals and the cc-pVTZ basis set, except for compound 13, for which 6-31G(d) was used. Calculations were not carried out on compound 4 given the size of the chain in the substituent and its similarity to compound 3. In compound 15, the chain was replaced by a terminating methyl group. For compounds 2 and 18, the methyl groups in the Bpin substituent were replaced with single hydrogen atoms after this had been shown to have little effect on the excitation energies. Test calculations were carried out to determine the effect of solvent on the excitation energies and it was found to influence the results by less than 0.1 eV and therefore neglected in all calculations. All plotted orbitals are B3LYP/cc-pVTZ isosurfaces with a value of 0.02 a.u.

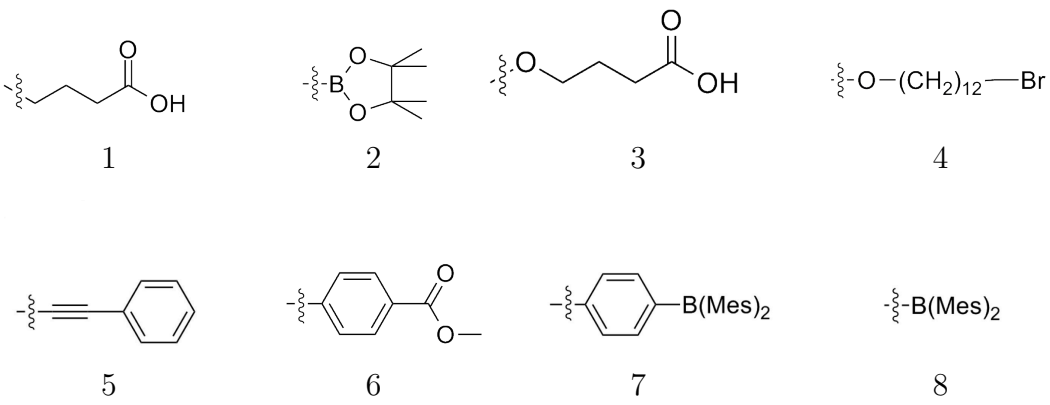

1 2 3 4

5 6 7 8

(a) Structures of 2-substituted pyrene derivatives

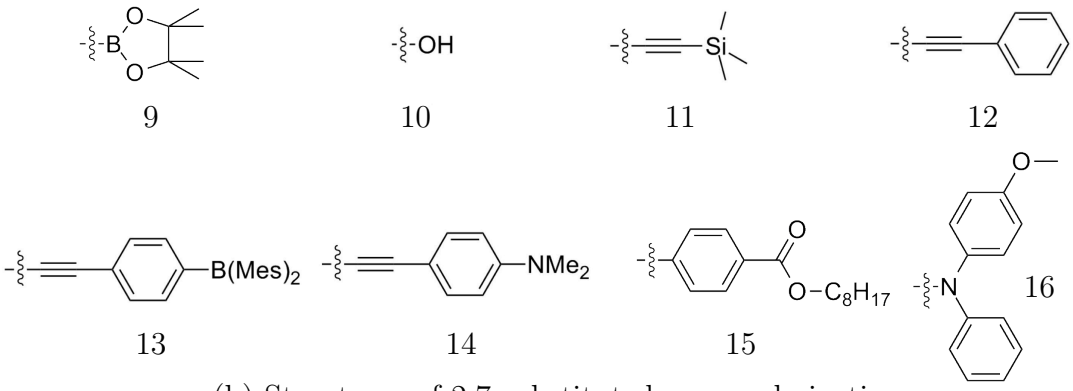

9 10 11 12

13 14 15 16

(b) Structures of 2,7-substituted pyrene derivatives

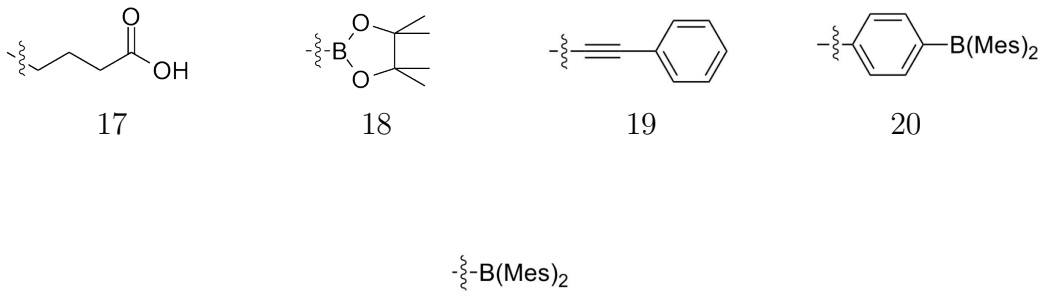

17 18 19 20

21

(c) Structures of 1-substituted pyrene derivatives

Figure 5.3: Structures of all pyrene derivatives.

5.1.3 Unsubstituted Pyrene

Firstly, we consider the performance for unsubstituted pyrene. Our B3LYP results agree with those published by other authors[189,190,192–194] and give the L_b and L_a states to be at 3.72 eV and 3.65 eV, respectively differing from the results of Dierksen and Grimme by only 0.04 eV. The experimental results available to us from the work of the Marder group give these two transitions at 3.42 eV and 3.67 eV. If we apply the correction mentioned earlier to account for the comparison between $\Delta E_{0-0}^{\text{obs}}$ and $\Delta E_{\text{vert}}^{\text{calc}}$ we can define "corrected-experimental values" of 3.61 eV and 3.94 eV. It can now be seen that the B3LYP estimate for the L_a state is too low, as expected.

As mentioned, all previous DFT studies incorrectly predict the high oscillator strength, ionic L_a state to be lower in energy than the low oscillator strength, covalent L_b state. CAM-B3LYP gives excitation energies of 3.92 eV (L_b) and 3.94 eV (L_a). Therefore, CAM-B3LYP has correctly reproduced—for the first time—the ordering observed experimentally. If we compare these with the "corrected-experimental results" of 3.61 eV and 3.93 eV then we see that CAM-B3LYP is overestimating the energy of the L_b state but correctly predicting the energy of the L_a state. The overestimation of the L_b state is to be expected, as CAM-B3LYP is known to overestimate the energy of local excitations which are correctly predicted with conventional hybrid functionals.

To facilitate the following discussion of substituent effects, the excitation energies that involve transitions most closely resembling those of the L_a and L_b states in unsubstituted pyrene are plotted in figures 5.4 and 5.5, respectively. The plots contain excitation energies calculated using both B3LYP and CAM-B3LYP as well as experimentally observed excitation energies. Also included are straight lines corresponding to the excitation energy of unsubstituted pyrene, with and without the correction suggested by Dierksen and Grimme. The figures clearly illustrate the effect of substitution at each position.

5.1.4 2-substituted Pyrene: Derivatives 1-8

The HOMO and LUMO orbitals of pyrene that are involved in the formation of the L_a state (Figure 5.2(a)) have nodes at the 2-position (Figure 5.1). The substitution

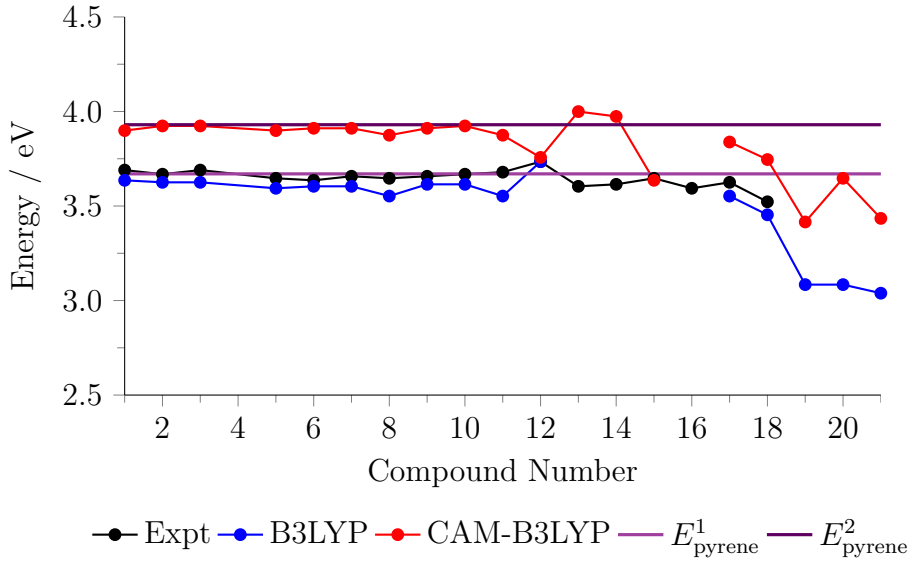

[1]The experimentally observed energy of the L_a state of pyrene (3.67eV)
[2]The experimentally observed energy of the L_a state of pyrene with "correction" (3.93eV)

Figure 5.4: Comparison of experimentally observed and DFT excitation energies (eV) for the L_a state of pyrene derivatives.

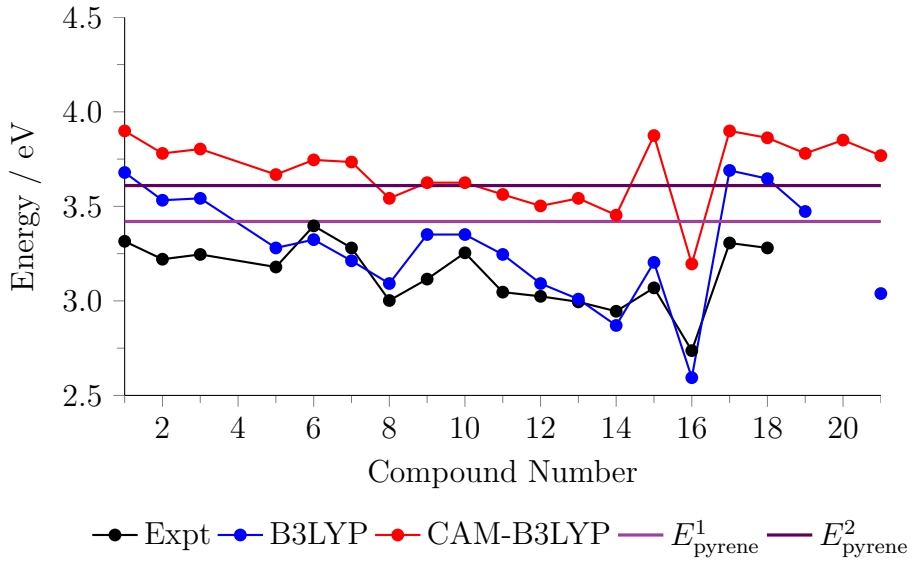

[1]The experimentally observed energy of the L_b state of pyrene (3.42eV)
[2]The experimentally observed energy of the L_b state of pyrene with "correction" (3.61eV)

Figure 5.5: Comparison of experimentally observed and DFT excitation energies (eV) for the L_b state of pyrene derivatives.

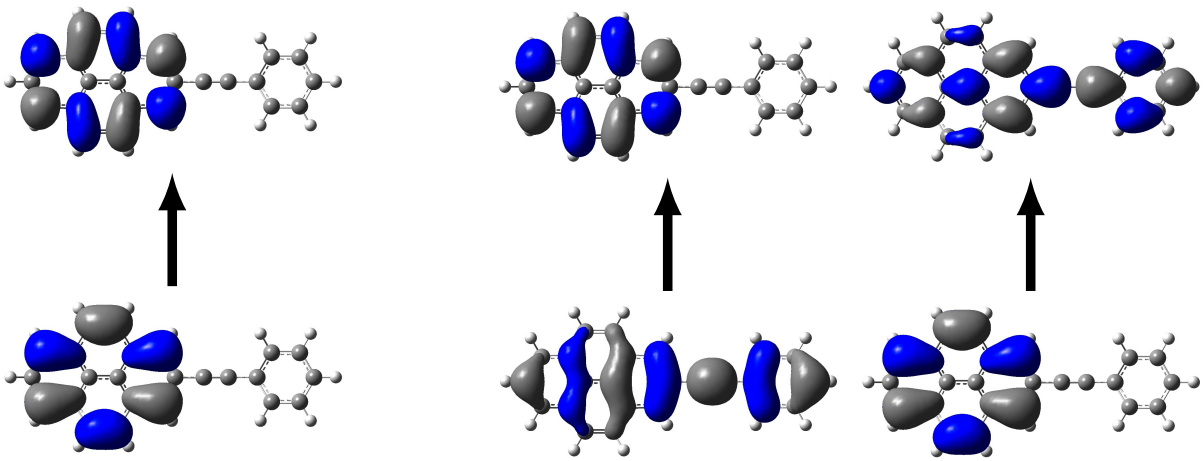

(a) (b)

Figure 5.6: The dominant orbital transitions in the (a) L_a and (b) L_b states of compound 5.

of pyrene in this position is therefore not expected to have significant effect on these orbitals. By considering the Kohn-Sham molecular orbitals, it is indeed possible to identify an excitation within each 2-substituted molecule that directly corresponds to the same orbital transition seen in the L_a state of pyrene. The B3LYP results for all the 2-substituted compounds give this L_a excitation energy within 0.1 eV of the energy calculated for unsubstituted pyrene. Unlike the incorrect ordering predicted by B3LYP for unsubstituted pyrene, the L_a state of all of the 2-substituted compounds is correctly predicted to be the second state—except for compounds 1 and 7 where it is predicted to be the 1^{st} and 4^{th} state, respectively. The same trends are seen in the results obtained with CAM-B3LYP, where all of the compounds have an easily identifiable L_a state which are within 0.1 eV of the same state in unsubstituted pyrene. As an example for the general trend seen in the orbitals of 2-substituted compounds, the molecular orbitals involved in the L_a and L_b states of compound 5 and 8 are shown in figures 5.6 and 5.7, respectively. It can clearly be seen from these examples that the orbitals involved in the L_a transition are indistinguishable from the the equivalent transition in unsubstituted pyrene.

The HOMO−1 and LUMO+1 orbitals involved in the L_b transition of pyrene have non-zero contributions at the 2-position. Substitution at this location is therefore expected to affect the nature of these orbitals, with the result being a shift in excitation

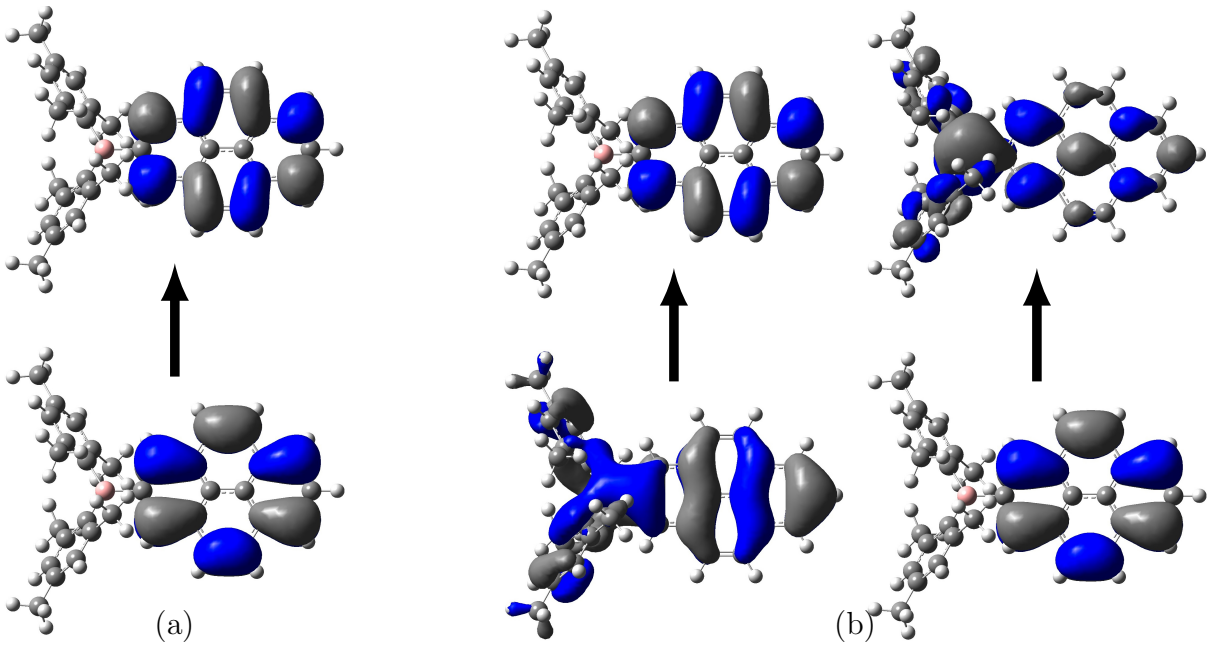

Figure 5.7: The dominant orbital transitions in the (a) L_a and (b) L_b states of compound 8.

energy away from that seen for unsubstituted pyrene. The experimental results show that the energy of the L_b state is reduced for all 2-substituted compounds. This observation is reproduced by the B3LYP results, with all excitation energies being at least 0.18 eV lower than the corresponding excitation in unsubstituted pyrene. B3LYP correctly predicts this state to be the lowest excited state for every compound. The same trend in results is seen for CAM-B3LYP where all excitation energies are at least 0.12 eV lower than the pyrene reference. The change in orbital delocalisation upon substitution is clearly illustrated for compounds 5 and 8 in figures 5.6 and 5.7, respectively.

5.1.5 2,7-substituted Pyrene: Derivatives 9-16

With the 7-position of pyrene being equivalent to the 2-position, the bis-substituted 2,7-pyrene derivatives are expected to show similar trends to those seen for the 2-substituted derivatives. The experimental results show the same lack of variation for the L_a state and reduction in energy for the L_b state. This again reflects the effect of the substituent on the orbitals involved in the respective transitions, an example of which is given for compound 15 in figure 5.8. The orbitals giving rise to the L_a state are again indistinguishable from those in the corresponding transition in pyrene, whereas for the L_b

state, the orbitals again delocalise over the substituent. When an L_a state is identifiable, B3LYP predicts it to be within 0.1 eV of the value for unsubstituted pyrene. Similarly, CAM-B3LYP also gives this excitation within 0.1 eV, with the exception of compounds 12, 15 and 16.

The 2,7-substituted compounds generally display a greater extent of delocalisation resulting in a more pronounced shift in the L_b excitation energy which can be seen in figure 5.5; all B3LYP L_b transitions occur at an energy at least 0.37 eV lower than in pyrene (except for compound 14 which is incorrectly higher in energy than in pyrene). The same trend is seen in the CAM-B3LYP results where the energy of the L_b excitation is at least 0.29 eV lower than the pyrene reference.

Both the B3LYP and CAM-B3LYP results show similar trends to those observed experimentally. That is, for the majority of compounds, the L_b state is the lowest in energy, followed by the L_a state. However, there are a few exceptions. When using B3LYP, the L_a state could not be identified for compounds 14 and 15, while it is found to be the 4^{th} and 14^{th} state in compounds 12 and 13, respectively. In the case of CAM-B3LYP, the L_a state for compounds 13 and 14 is the 4^{th} and 3^{rd} state, respectively. In the case of the latter two compounds in particular, broad peaks observed in the absorption spectra overlap with the "pyrene-like L_a" transition. The intense absorption arises from a delocalized state which generally involves charge-transfer from the pyrene core to empty p-orbitals on the $B(Mes)_2$ groups for 13 and from the nitrogen lone-pair to the pyrene core in 14. The result is that, for both extended π-acceptor and π-donor conjugated systems, these charge-transfer absorptions lie between the L_b- and L_a-like excitations.

For both the 2- and 2,7-substituted compounds (1-16), the trends shown in figure 5.4 show that both B3LYP and CAM-B3LYP yield an excitation energy very close to the excitation energy of unsubstituted pyrene for the L_a state, with the exception of compounds 12 and 16. Additionally, CAM-B3LYP shows exceptional agreement with the corrected experimental value. This highlights the way in which substitution at these positions has little effect on the excitation energy of the L_a state. For the L_b state (figure 5.5), both functionals now give excitation energies lower than unsubstituted pyrene, showing the influence of the substituent on this transition. However, given the relatively good performance of B3LYP for this state, CAM-B3LYP generally gives

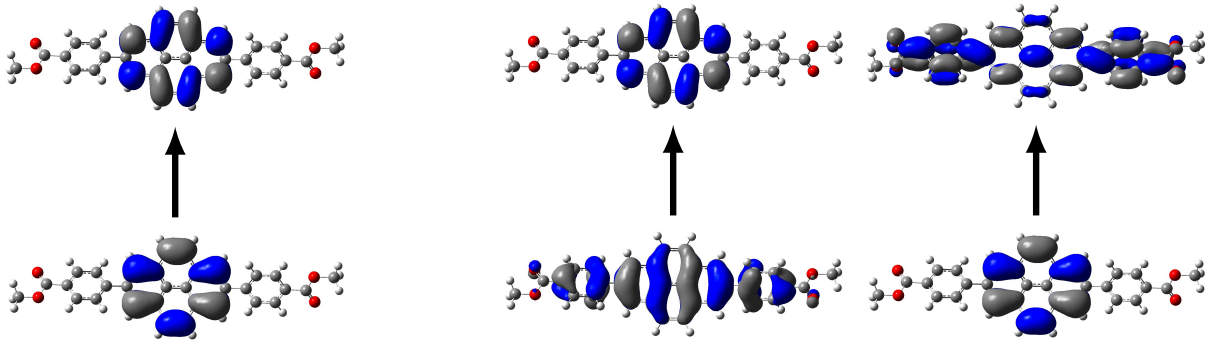

(a) (b)

Figure 5.8: The dominant orbital transitions in the (a) L_a and (b) L_b states of compound 15.

excitation energies which are too high when compared to experimental values.

5.1.6 1-substituted Pyrene: Derivatives 17-21

All four orbitals involved in the L_a and L_b states of pyrene (Figure 5.2) have non-zero contributions at the 1-position. Substitution at this position is therefore expected to affect the energy of *both* of these states. Firstly, a brief discussion of the experimental observations is necessary. Only one transition could be resolved for compounds 20 and 21. The high extinction coefficient of this state would suggest that it is the L_a, however, as substitution in this position is expected to increase the "allowedness" of the L_b state, no definite assignment can be made. Similarly, in compound 19, both the lowest excitations have high extinction coefficients, again making assignment difficult. Compounds 17 and 18 display similar behaviour to the 2- and 2,7-substituted compounds; it should be mentioned that there is a noticeable similarity between the excitation energies for these two compounds and those seen in unsubstituted pyrene.

The B3LYP results for compounds 17 and 18 do not reproduce the ordering of the states observed experimentally. However, the substituents involved in these two compounds have little effect on the pyrene orbitals. Therefore, it is perhaps unsurprising that B3LYP gives the incorrect ordering for these compounds, given its performance for unsubstituted pyrene; for both compounds, both states are within 0.1 eV of the corresponding transition in pyrene. The orbitals involved in the L_a and L_b states of

compound 18 are shown in figure 5.9 to illustrate the similarity with those seen in pyrene. Unlike pyrene, CAM-B3LYP does not correct this failure of B3LYP; it also predicts the lowest state to be L_a followed by L_b. The energy gap between the two states is much smaller, suggesting that if the theory/experiment comparison issue is accounted for, the L_a state would be accurately predicted using CAM-B3LYP, similar to pyrene. The small energy gap predicted by CAM-B3LYP for pyrene makes it possible for the ordering of the two states to switch easily—even in cases where the influence of the substituent is relatively small.

For compounds 19, 20 and 21, significant delocalisation onto the substituent occurs. In particular, some orbitals for the latter two of these three compounds exist entirely on the substituent alone. An example of this delocalisation in compound 19 is shown in figure 5.10, which can be compared to the small effect seen in compound 18. It can now be seen that the orbitals involved in the L_a transition which were unaffected by substitution in the 2- and 7-positions, are now partially delocalised onto the substituent. This large delocalisation results in significant shifts in excitation energy when using both B3LYP and CAM-B3LYP. Although CAM-B3LYP generally preserves the energy of the L_b state with respect to unsubstituted pyrene, all other excitations (both functionals, both states) vary by as much as 0.5 eV when substituted at the 1-position.

The theoretically determined geometry of compound 19 disagrees with that reported in Ref 195. The structure in that earlier study has the ethynylaryl group twisted away from the pyrene system at a right angle, whereas the optimisation performed here gives an entirely planar structure. It should be expected that the triple bond will facilitate conjugation between the benzene ring and the pyrene ring system. This conjugation suggests that the planar structure predicted here by the B3LYP/6-31G(d) method is correct. Additional evidence comes from the shifts seen in the experimental results, suggesting the substituent is playing a role in the transitions which would not be possible without conjugation. To verify this, small variations were made to the geometry they presented to break any symmetry present and it was then optimised yielding a planar structure, 0.05 eV lower in energy.

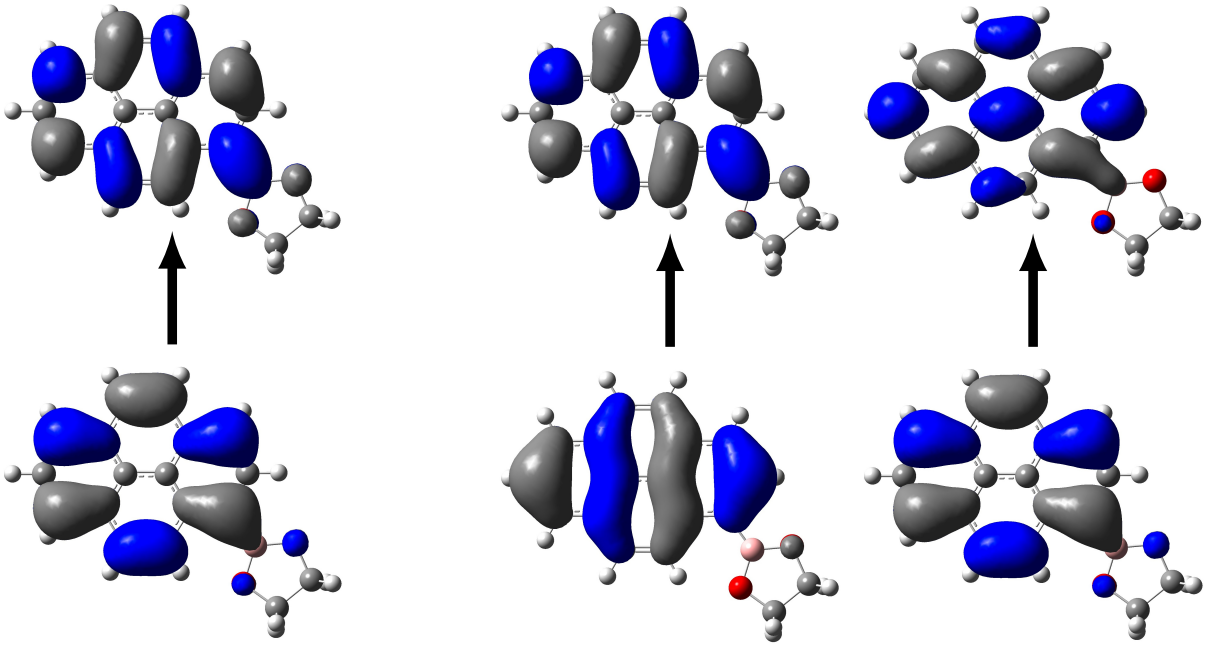

(a) (b)

Figure 5.9: The dominant orbital transitions in the (a) L_a and (b) L_b states of compound 18.

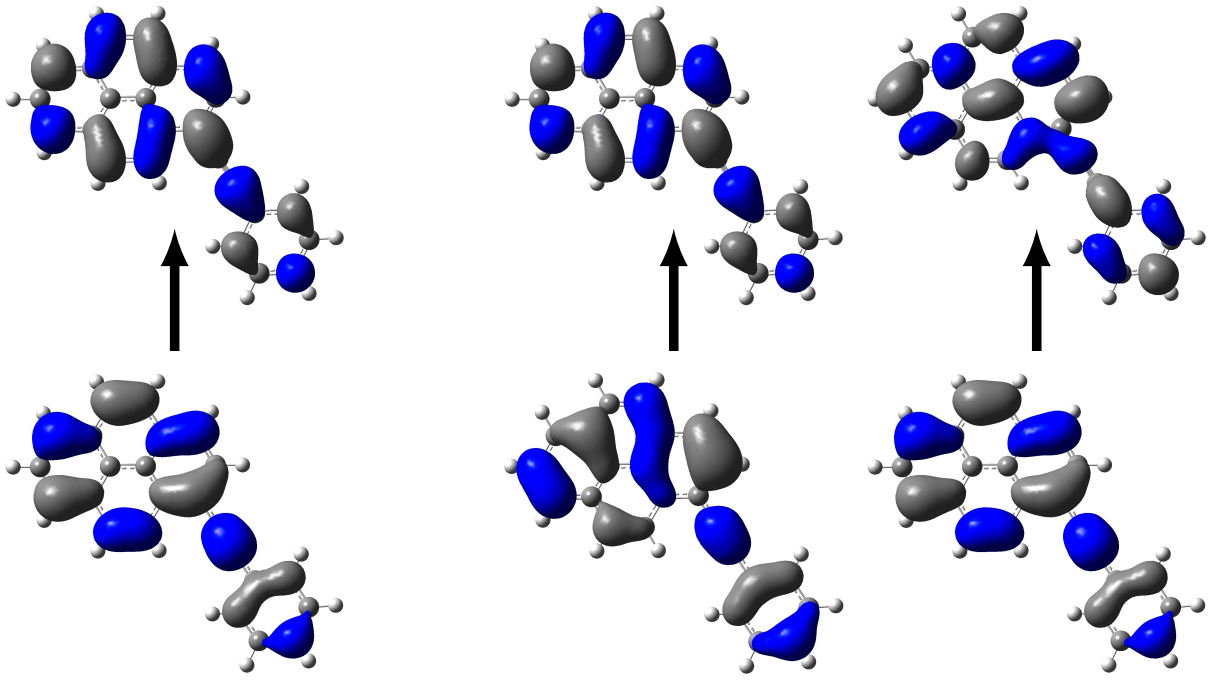

(a) (b)

Figure 5.10: The dominant orbital transitions in the (a) L_a and (b) L_b states of compound 19.

5.1.7 The Influence of Boron Based Substituents

As mentioned, the compounds considered here are of specific chemical relevance. Of particular interest are compounds involving boron and the role that the boron atom plays in determining the characteristics of the compound. There are two types of substituent based on the boron atom. The first is the dimesitylboron ($B(Mes)_2$) moiety which behaves as an efficient π-acceptor[196–198] and is of interest in work involving π-conjugated organic compounds containing 3-coordinate boron centres which have found applications in OLEDs, sensors, solar cells and other materials.[199] This substituent is present in a number of forms: $B(Mes)_2$ (compounds 8 and 21), $PhB(Mes)_2$ (compounds 7 and 20) and $CCPhB(Mes)_2$ (compound 13). In these compounds the boron atom is either bonded directly to the pyrene system or through a conjugated π-intermediate. The empty p-orbital on the boron atom is therefore able to facilitate extensive delocalization of the electron density from the pyrene system onto the substituent. The second type of boron containing substituent is present in compounds 2, 9 and 18 as the Bpin group. Borylated arene compounds are important precursors to a range of derivatives.[200] In these systems, the presence of two oxygen atoms bonded directly to the boron atom completely negates the effect seen in $B(Mes)_2$. The empty p-orbital is likely filled with electron density from the oxygen atoms, reducing its ability to allow electron density to transfer from the pyrene system onto the substituent. The result is that relatively large shifts are seen in the L_b state of compounds 7, 8, 13, 20 and 21 while little change is seen for compounds 2, 9 and 18.

The effect of the Bpin group on the orbitals of the pyrene system is therefore limited. A similar effect is also seen in compounds 1 and 17 where the pyrene system is substituted with an acid. As the acid is on the end of a short alkyl chain, there is no possibility for conjugation onto the substituent. The orbitals involved in the L_b and L_a state of compound 1 are so similar to those in unsubstituted pyrene, that even the incorrect ordering of these two states is reproduced by B3LYP. This is the only 2- or 2,7-substituted compound for which this incorrect ordering occurs when using B3LYP, highlighting the negligible effect of this substituent. In a similar fashion to unsubstituted pyrene, CAM-B3LYP is able to correct this ordering problem. A similar situation is seen in compound 17, although, for this molecule CAM-B3LYP is unable to reproduce

the correct ordering.

5.1.8 Charge-Transfer Excitations

It has been shown that conventional hybrid functionals fail to quantitatively reproduce excitation energies for the ionic L_a state of pyrene and its derivatives. The failure of hybrid functionals within TDDFT for this state is different from that already seen earlier for charge-transfer and Rydberg states. In the latter two cases, the value of the overlap diagnostic Λ (equation (2.89)) is low. However, for the excitation energies of pyrene, calculated using B3LYP, the values of Λ are 0.88 for the L_a state and 0.68 for the L_b state. Clearly, Λ is unable to predict this type of failure.

The substitution of the pyrene system with large, conjugated groups does give rise to traditional charge transfer excitations. These can be understood and potentially predicted through the use of Λ. The presence of low-lying, heavily underestimated, charge transfer states can be misleading when trying to interpret the results for these compounds. In compounds 13 and 14 there are charge-transfer states, both with $\Lambda < 0.3$, at the 3rd excitation with B3LYP. These states are completely removed from the low energy region when using CAM-B3LYP. The nature of these excitations is illustrated in figures 5.11 and 5.12. Although the oscillator strengths of these states is essentially zero and they will not be seen experimentally, their erroneous presence in the low energy region is still a problem when using theory in combination with experimental observations.

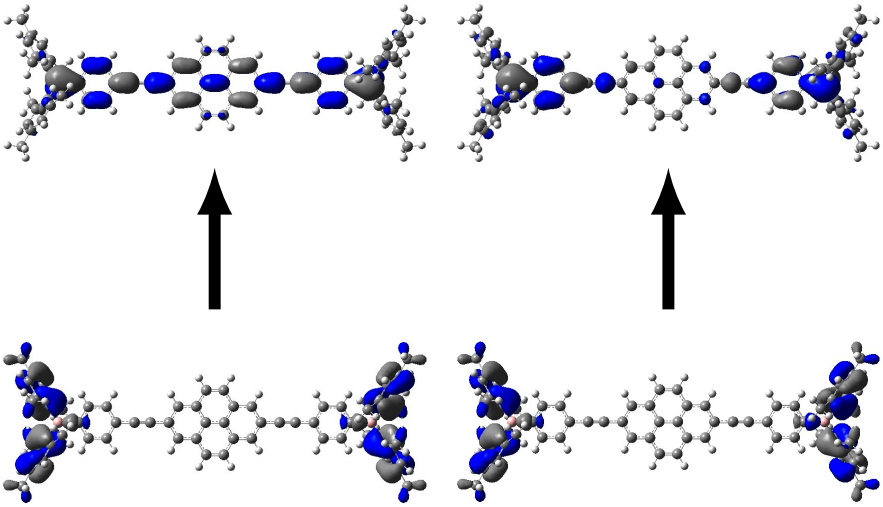

Figure 5.11: The orbital contributions to the low Λ (3^{rd}) excitation seen in compound 13.

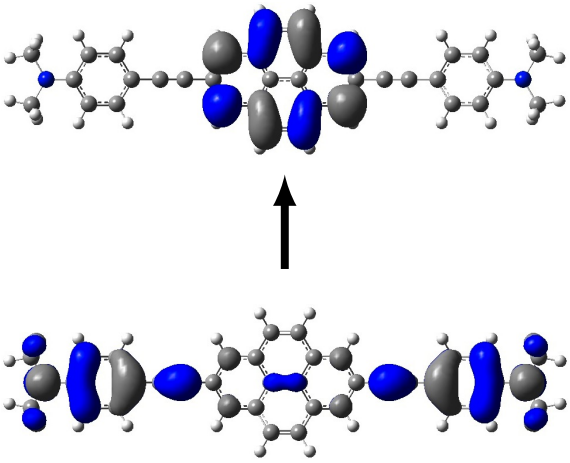

Figure 5.12: The orbital contributions to the low Λ (3^{rd}) excitation seen in compound 14.

5.2 Excited State Dimers and Complexes

We now consider the role of TDDFT in predicting the structure of two classes of complexes which are formed as a result of electronic excitations. The terms "excimer" and "exciplex" are used to refer to excited state dimers and excited state complexes, respectively. The generally accepted definition for such systems is that they are unbound in the ground electronic state yet bound in an electronically excited state.[201,202] Alternatively, in cases where the ground state is very weakly bound, the equilibrium inter-fragment distance of the excited state is significantly shorter than in the ground state and the dissociation energy of the excited state is much greater than that of the ground state. The lowest potential energy curve plotted in figure 5.13 represents the lowest excited state of the Ne_2 excimer and it can be seen that, compared to the ground state data in chapter 4, the minimum is much deeper and at a much shorter interatomic distance.

One of the most common excimers is the excited pyrene dimer. Experimental studies have shown the appearance of a broad emission band as the concentration of pyrene in solution is increased.[203] This behaviour has been attributed to the formation of excimers and is sufficiently common that all of the experimental data referred to in section 5.1 had to be recorded at sufficiently low concentrations to avoid the formation of excimers. The following discussion and results focus on the case of excimers, much of which can be generalised to exciplexes where the two fragments are not the same. Anything that is unique to exciplexes will be discussed along with the relevant results. Excimer formation involves one fragment in its ground state and one in its excited state forming a dimer. An accurate description of excimers therefore requires a functional that is accurate at determining both intermolecular forces and excited state energies, thereby connecting the two key themes of this thesis. Given the nature of the species involved, we will employ the dispersion correction outlined in chapter 4. As an initial example, the neon excimer is considered. This is followed by an analysis of the benzene excimer and the styrene-trimethylamine exciplex.

5.2.1 Neon Excimer

As a preliminary investigation, we follow the work of Huenerbein and Grimme[204] and assess the performance of CAM-B3LYP in predicting the structure and potential energy

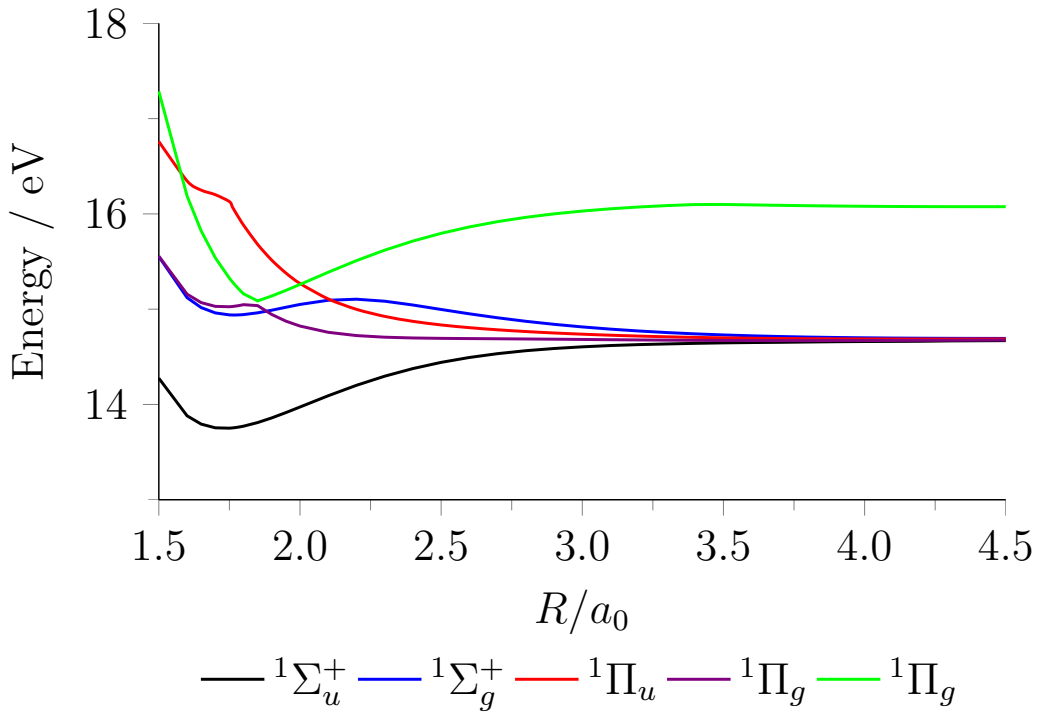

Figure 5.13: Excited states of the neon dimer calculated with CAM-B3LYP/aug-QZVP relative to twice the ground state energy of the neon atom.

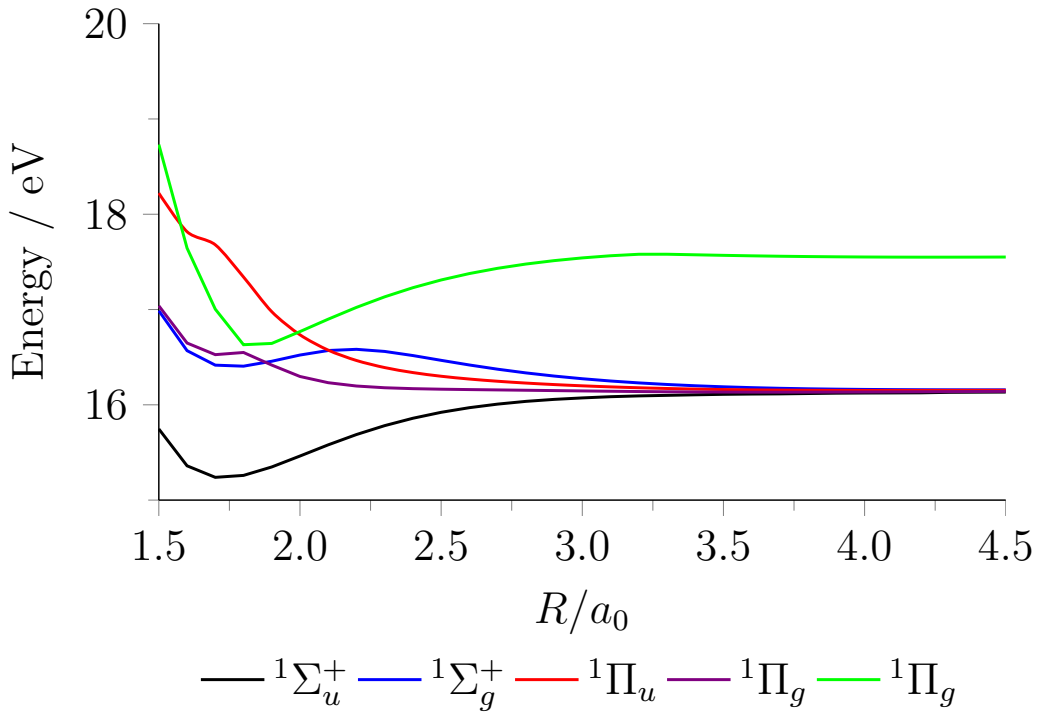

Figure 5.14: Excited states of the neon dimer calculated with BH-HLYP/aug-QZVP relative to twice the ground state energy of the neon atom.

curve of the noble gas excimer Ne_2. Given that their findings demonstrated the superior performance of BH-HLYP over B3LYP, it is relevant to determine the performance of CAM-B3LYP. CC2 reference data is available in their study as well as BH-HLYP and BLYP comparison data. There are two areas of interest: i) the description of the equilibrium geometry region including dissociation energy and ii) the inter-fragment distance and the asymptotic behaviour of the potential energy curves corresponding to excitation on a single fragment. For this noble gas excimer, we employ the same aug-QZVP basis set as used by Huenerbein and Grimme and the dispersion correction of equation (4.15).

A comparison of BH-HLYP and CAM-B3LYP with CC2 is provided in table 5.2; potential energy curves are presented in 5.14 and 5.13, respectively. The state of interest—the one which facilitates excimer formation—is the lowest excited state $^1\Sigma_u^+$. It is clear from the results that both BH-HLYP and CAM-B3LYP, when augmented with the dispersion correction, provide excellent descriptions of both the dissociation energy and equilibrium distance. The effect of the dispersion correction in this region is small, accounting for a lower than 0.05eV reduction of the dissociation energy.

Table 5.2: Dissociation energies (D_e/eV) and equilibrium interfragment distances (R_e/Å) for the neon excimer.

		BH-HLYP	CAM-B3LYP	CC2
Ne_2	R_e	1.72	1.73	1.71
	D_e	0.90	0.95	0.85

For CAM-B3LYP (figure 5.13) and BH-HLYP (figure 5.14), the energies of the excited states are plotted relative to twice the energy of the neon atom. As a result, the asymptotic values of each curve corresponds to an excitation energy of a single neon atom. The CC2 (exp.[205]) excitation energies for the 1st and 2nd excited states are 16.02 eV (16.67 eV) and 17.71 eV (18.38 eV), respectively. BH-LYP values are 16.15 eV and 17.58 eV, respectively. CAM-B3LYP fares slightly worse with values of 14.70 eV and 16.15 eV. BLYP (data and plots available in Ref. 204) leads to a severe underestimation of the energies of the states and also produces erroneous states not seen in calculations which employ exact exchange, supporting the view that TDDFT calculations with pure GGA functionals should be avoided in favour of those that incorporate some portion of

exact exchange.

5.2.2 Benzene Excimer

The benzene excimer received a similar analysis to the neon excimer in the work of Huenerbein and Grimme.[204] There are several other works of relevance, involving coupled cluster,[206] CASSCF[207] and TDDFT studies.[208] Firstly, the equilibrium region will be investigated by employing fully relaxed geometries. Secondly, the behaviour of the potential surface as a function of R, the interfragment distance, will be considered. This will include a discussion of the long-distance behaviour. Comparison is made with two relevant works: Huenerbein and Grimme[204] and Fink *et al.*[207] In order to facilitate this comparison, we employ the same basis sets that they used: TZVP and cc-pVDZ, respectively. The former of these two studies showed a generally good performance by the BH-HLYP functional and the interest here is whether CAM-B3LYP can offer any improvement over this performance.

Benzene excimer at the equilibrium geometry

Firstly, the equilibrium region of the benzene excimer is considered. For this, all calculations use the TZVP basis set and are dispersion corrected. In order for our results to be comparable to those Huenerbein and Grimme, the CAM-B3LYP dispersion correction is defined to be identical to the one they used for BH-HLYP, including the s_6 parameter which is set at 0.9. The dissociation energy of the excimer can be calculated as

$$\Delta E = (E_{\mathrm{B}^*} + E_{\mathrm{B}}) - E_{\mathrm{B}^*\mathrm{B}}, \tag{5.6}$$

where E_{B}, E_{B^*} and $E_{\mathrm{B}^*\mathrm{B}}$ denote the energy of the benzene monomer, the benzene monomer in its first excited state and the benzene excimer, respectively. All of the energies calculated are for fully relaxed geometries. This requires the optimisation of excited states which is done through the implementation of analytic gradients in TDDFT. The Gaussian09[191] code was used for these calculations. As excimer formation occurs through the lowest excited state which is not of charge-transfer character, it can be expected that CAM-B3LYP and BH-HLYP will likely give results in close agreement with B3LYP. However, the comparison of most interest is between the former two. The

dissociation energy calculated by CAM-B3LYP is 0.75 eV, slightly higher than the 0.70 eV calculated using BH-HLYP. This corresponds to a slightly better performance by BH-HLYP as the experimental value of the dissociation energy is in the region 0.22–0.36 eV. However, as can be seen in table 5.3 (albeit using a slightly different basis set), CAM-B3LYP gives a much more accurate prediction of the excitation energy of the monomer state that is involved in excimer formation. When using the TZVP basis set, the excitation energies for BH-HLYP and CAM-B3LYP can be revised to 5.63 eV and 5.22 eV, respectively; CAM-B3LYP shows an even greater improvement over BH-HLYP. Therefore, the better performance of BH-HLYP over CAM-B3LYP is likely due to a fortuitous cancellation of errors, despite the latter's superior performance in predicting the excited states at equilibrium geometry of the benzene monomer. Unfortunately, the ambiguity in the reference values makes drawing any firm conclusions difficult.

Benzene excimer in the asymptotic region

In order to plot a potential energy curve as a function of the interfragment distance, frozen ground state geometries were chosen in which the C-C and C-H bond distances are 1.397 and 1.084Å, respectively.[207,209] The potentials were plotted using the cc-pVDZ basis set as used by Fink *et al.*[207] The B3LYP and BH-HLYP results of Fink *et al.* have been successfully reproduced and a comparison of the potential energy curves of B3LYP, BH-HLYP with CAM-B3LYP is presented in figures 5.15, 5.16 and 5.17. The trends in the CAM-B3LYP curves effectively reproduce those seen in BH-HLYP. No dispersion correction is considered here to ensure consistency with Fink *et al.* and also because we are now concerned with functional trends rather than absolute energy values.

The potentials in figures 5.15, 5.16 and 5.17 are plotted relative to the energy of two non-interacting ground state benzene monomers. In cases where the excited state potentials concern the interaction between one benzene monomer in its ground state (B) and one benzene monomer in its excited state (B^*), the asymptotic value of each potential must equal the corresponding excitation energy of the benzene monomer,

$$E^{R\to\infty}_{[\mathrm{BB}]^*} = (E_{\mathrm{B}^*} + E_{\mathrm{B}}) - (E_{\mathrm{B}} + E_{\mathrm{B}}) = E_{\mathrm{B}^*} - E_{\mathrm{B}} = \omega_{\mathrm{B}} \tag{5.7}$$

Table 5.3: Excitation energies (eV) of the benzene monomer calculated using cc-pVDZ.

	expt.	B3LYP	BH-HLYP	CAM-B3LYP
1^1B_{2u}	4.78/4.90	5.48	5.72	5.57
1^1B_{1u}	6.20	6.22	6.26	6.32
1^1E_{1u}	6.94	7.26	7.45	7.35
IP − EA	-	11.15	11.12	11.19

However, for charge transfer states, the formation of ionic species must be considered,

$$E^{R\to\infty}_{[\mathrm{BB}]^*} = (E_{\mathrm{B}^+} + E_{\mathrm{B}^-}) - (E_{\mathrm{B}} + E_{\mathrm{B}}) = (E_{\mathrm{B}^+} - E_{\mathrm{B}}) - (E_{\mathrm{B}} - E_{\mathrm{B}^-}) = \mathrm{IP}_{\mathrm{B}} - \mathrm{EA}_{\mathrm{B}}. \tag{5.8}$$

The lowest excited state excited in the excimer ($^1B_{1g}$) involves a local excitation and the asymptotic values of the potential for all three functionals considered exactly match the monomer excitation energies ($^1B_{2u}$) given in table 5.3. The values of IP − EA are also listed, which should equal the asymptotic value of the lowest charge transfer state of the benzene excimer, which is of symmetry $^1E_{1g}$.

When using B3LYP, the 1^1E_{1g} state has charge-transfer character. This is evident from the slower $-0.2/R$ decay of the potential. The asymptotic value of this state is however only 6.72 eV which is 4.43 eV lower than IP − EA. This severe underestimation of charge-transfer energies is well-known and is a serious problem as it incorrectly designates the lowest $^1E_{1g}$ as being charge-transfer and disrupts any similar energy states with the same symmetry. CAM-B3LYP successfully removes this erroneous charge-transfer state by pushing it up in energy. The result is that the 1^1E_{1g} state no longer has charge-transfer character, and gives the correct asymptotic value of 7.35 eV, degenerate with 1^1E_{1u}. The charge transfer state as calculated by CAM-B3LYP has an asymptotic value of 11.06 eV, in excellent agreement with the value of IP − EA.

Excitation energy transfer in the Benzene excimer

Excimer formation facilitates the transfer of energy from one excited monomer to another ground state monomer,[210]

$$B_1^* + B_2 \to B_1 + B_2^*. \tag{5.9}$$

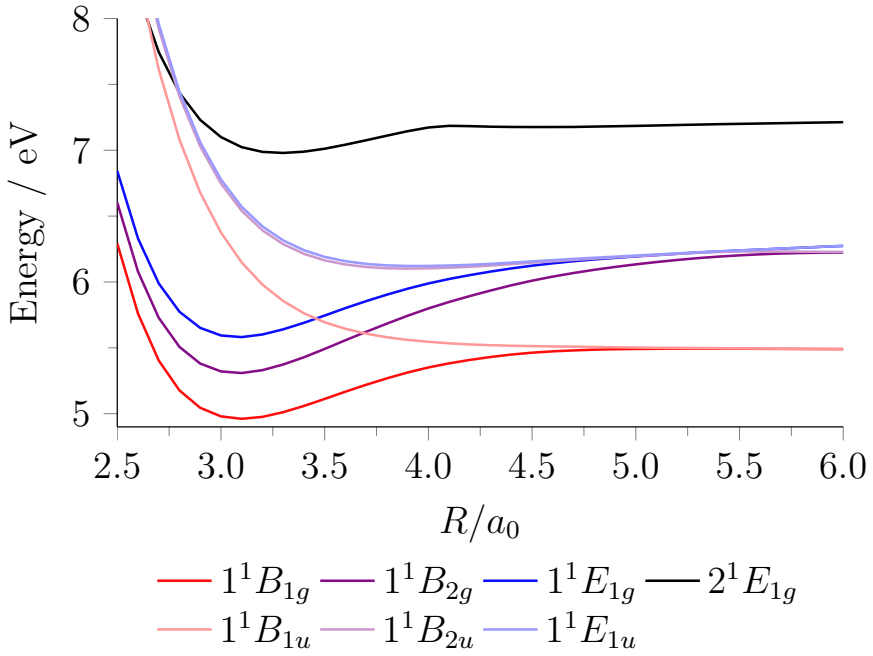

Figure 5.15: Potential energy curves of the excited states of the benzene dimer as calculated with B3LYP/cc-pVDZ.

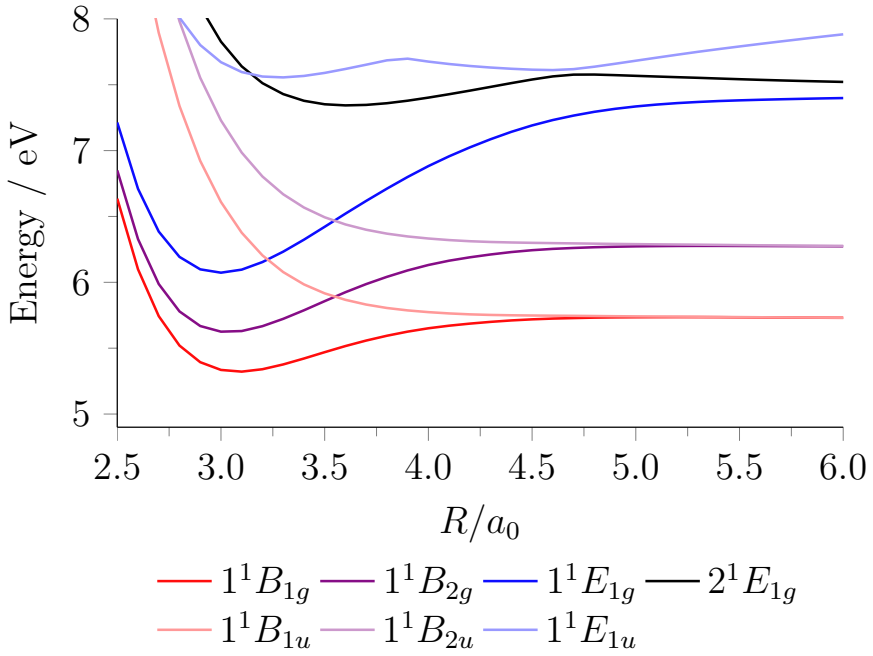

Figure 5.16: Potential energy curves of the excited states of the benzene dimer as calculated with BH-HLYP/cc-pVDZ.

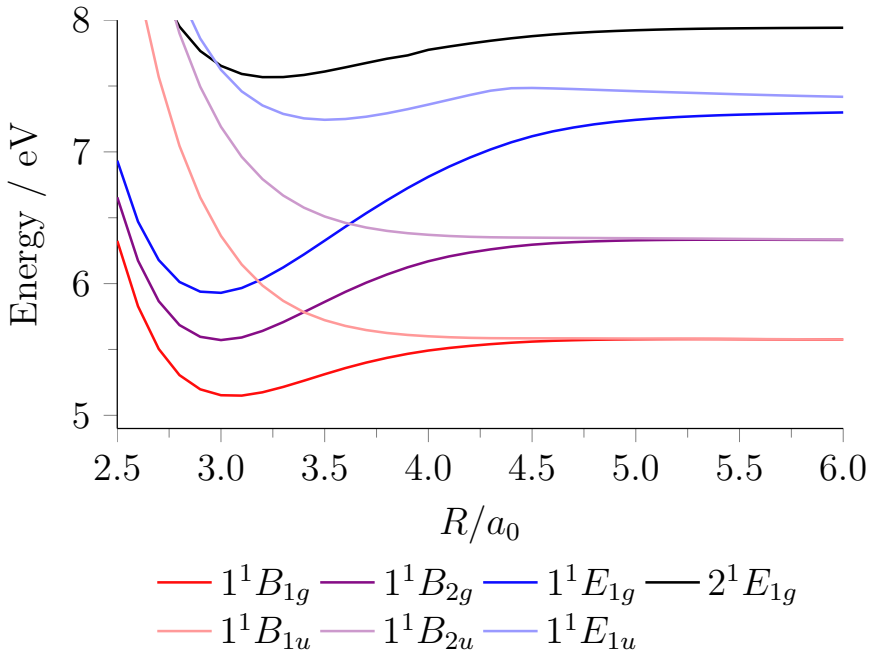

Figure 5.17: Potential energy curves of the excited states of the benzene dimer as calculated with CAM-B3LYP/cc-pVDZ.

The rate of this process is dependent on the electronic coupling matrix element v_{EC}, which measures the splitting of degenerate monomer states as a result of the interaction in the excimer. This is known as Exciton or Davydov splitting, and for excimers is equal to half the vertical excitation energy of the state of interest. An accurate treatment of this parameter should produce a smooth curve which decays to zero with the interfragment distance. Figure 5.18 shows the behaviour of v_{EC} for the 1^1E_{1u} monomer state as described by each functional considered. Clearly, the presence of low-lying charge-transfer states in the B3LYP picture produces an incorrect kink in the curve which is also too shallow at shorter distances, when compared with reference data.[207] CAM-B3LYP and BH-HLYP give curves which are almost indistinguishable from the reference curve - both have successfully removed the low-lying charge-transfer state.

5.2.3 The styrene-trimethylamine exciplex

The final system considered by Huenerbein and Grimme is the styrene-trimethylamine (*sty-tma*) exciplex. The formation of this excimer occurs through a charge-transfer state and so is particularly relevant to this thesis. The relevant orbital transition is HOMO→LUMO, where the HOMO is localised almost entirely on the *tma* fragment and

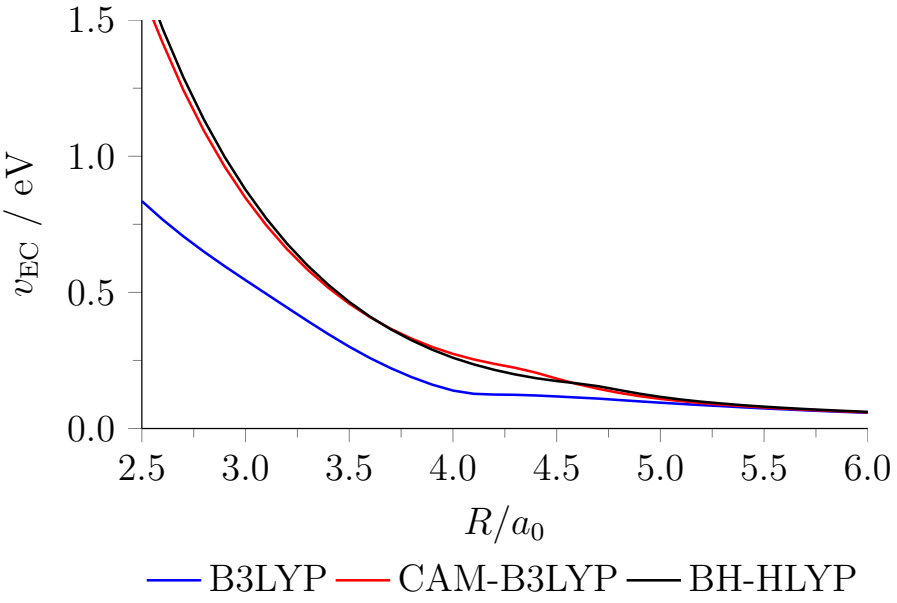

Figure 5.18: The trend in the electronic coupling matrix element v_{EC} (eV) as a function of interfragment distance R (a_0).

the LUMO on the *sty* fragment. Excimer formation is therefore through the interaction of a ground state *tma* molecule and *sty* in its first excited state

$$\Delta E_{[sty-tma]^*} = (E_{sty^*} + E_{tma}) - E_{[sty-tma]^*}. \tag{5.10}$$

The experimentally determined first excitation energy of *sty* is 4.31 eV.[211] As the experimental dissociation energy is 0.66 eV,[212] we can put the vertical excitation energy of the excimer at 3.56 eV, accounting for 0.09 eV for the ZPVE as determined by BH-HLYP.

BH-HLYP gives the first excited state of *sty* at 4.79 eV and the excimer energy at 3.90 eV. These values are 0.48 eV and 0.34 eV above the experimental reference values. CAM-B3LYP gives the states at 4.59 eV and 3.66 eV, only 0.18 eV and 0.10 eV above experiment. Clearly, CAM-B3LYP is doing a much better job than BH-HLYP at predicting the energetics at the equilibrium structure of the relevant excited states. However, when the necessary energy difference is computed to determine the dissociation energy, CAM-B3LYP is slightly higher at 0.93 eV, than BH-HLYP at 0.89 eV. Although the BH-HLYP dissociation energy is slightly closer to the experimental value, this conceals the performance of CAM-B3LYP in determining the energy of the states involved.

Summary

An extensive investigation of TDDFT vertical and experimentally observed excitation energies of pyrene and a number of its derivatives shows a clearly superior performance of CAM-B3LYP over B3LYP. Not only does CAM-B3LYP predict the correct ordering of the lowest two excited states of unsubstituted pyrene while conventional hybrid functionals do not, it also provides an exceptional reproduction of variations in experimental excitation energies observed when different classes of substituent are employed. All of these conclusions are drawn in conjunction with corrections necessary when considering the non-trivial comparison of vertical excitation energies and experimental (0-0) excitation energies.

Given the extent to which both functionals incorporate exact exchange in the long-range region, the performance of BH-HLYP and CAM-B3LYP should perhaps not be expected to differ significantly. In the case of the formation of organic excimers and exciplexes, the two functionals have indeed been shown to have a largely similar performance. They significantly outperform the conventional hybrid functional B3LYP whose tendency to underestimate charge-transfer states causes disruption to other low-lying states of a similar energy.

The impact of incorrectly underestimated charge-transfer states produced by B3LYP has been illustrated in this chapter for a number of scenarios. Such poor performance can significantly affect the confidence experienced when using this functional and the superior performance of CAM-B3LYP indicates the importance of long-range exact exchange.

Chapter 6

Properties of the Retinal chromophore

The ability of CAM-B3LYP to successfully describe a series of properties and characteristics of retinal is investigated. Firstly, the proton affinity and the effect of the protein environment are considered. In both cases, the application of CAM-B3LYP yields results in much better agreement with reference data compared to conventional GGA and hybrid functionals. Secondly, the effect of physical (ringtwist) and chemical (hydrogenation) change to the retinal molecule are considered. Of particular interest are the differing characters of the excitations produced by different functionals. The purpose of the work is not so much to compile a systematic picture of retinal and its characteristics using CAM-B3LYP, but rather to identify situations in which conventional hybrid functionals fail and show how this can be remedied by using a long-range corrected alternative. In this respect, CAM-B3LYP shows excellent performance.

Human vision is governed by the protein rhodopsin which contains the chromophore retinal. The absorption of light by retinal causes a photoisomerization process which induces an electrochemical response responsible for sight.[213] Retinal binds to the protein through a protonated Schiff base (pSb). It is this form that is therefore used to model rhodopsin in the present study and its structure is shown in figure 6.1. There have been numerous studies conducted into the ability of computational simulations to reproduce the behaviour of the retinal chromophore. It is common to use polyenes and the protonated Schiff bases of polyenes, where a terminating CH_2 group has been replaced with the isoelectronic NH_2^+ group, as models for the retinal molecule.[214–216] Given that the

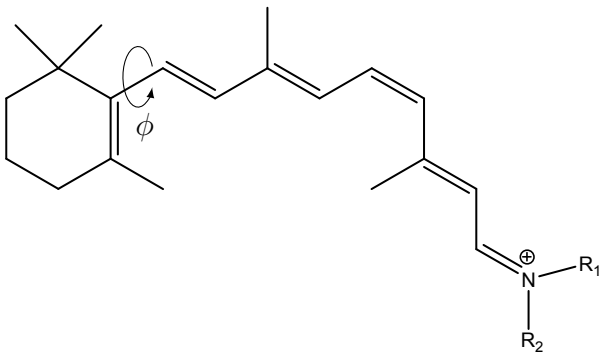

Figure 6.1: Chemical structure of the protonated Schiff base form of retinal. The twist about the C6-C7 bond is denoted by ϕ.

functionality of retinal arises from its photoinduced twisting mechanism, several studies probe the potential energy surface as a function of a number of twist angles.[217,218] In particular, there have been a number of studies conducted by Sundholm and co-workers, including an investigation into the twisting mechanism[219] in which high-level CC2 results were obtained. The outcomes of these studies will be discussed in further detail, in relation to the work conducted here, at the appropriate points.

6.1 Proton affinity

We first consider the binding between the retinal chromophore and the protein environment, which occurs through the protonated Schiff base. As noted by Wanko *et al.*[215] the delocalization error seen at the LDA and GGA levels erroneously stabilises systems where charge is delocalised—this underestimation was explicitly illustrated in stretched H_2^+ in section 3.2. This is relevant for systems such as retinal, which contain extended conjugated functional groups. The tendency of a functional to delocalise charge across such a system will artificially lower the energy and so at the LDA and GGA levels, the proton binding energy of the Schiff base is too high.[215] The proton affinity of the Schiff base group attached to a series of polyene chains of increasing length was determined; the error increases with increasing chain length.

To test the ability of CAM-B3LYP to correctly describe the proton binding energy of the Schiff base, we calculated the proton affinities of Schiff bases attached to polyene

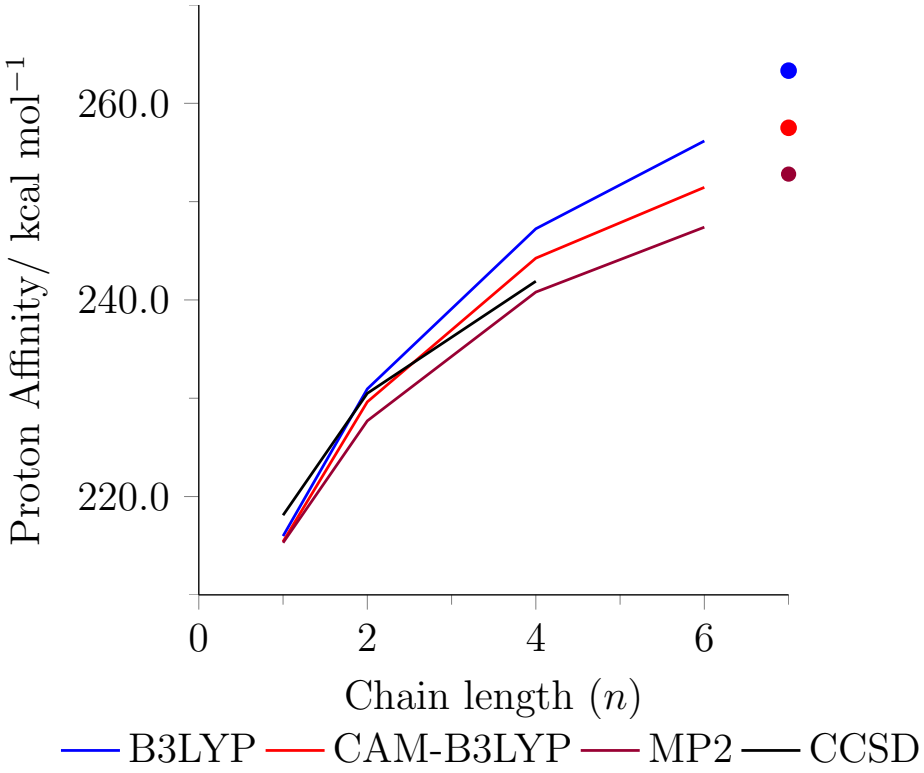

Figure 6.2: The variation of proton affinity as a function of the length of the pSbn chain length where n denotes the number of double bonds. The single data points at the right hand side indicate the value for the full retinal chromophore.

chains, pSbn, where n indicates the number of double bonds in the chain system,

$$\mathrm{PA} = E_{\mathrm{Sb}n} - E_{\mathrm{pSb}n}. \tag{6.1}$$

Both B3LYP and CAM-B3LYP geometries were optimised with the 6-31G(d) basis set and the affinities were then determined using the TZVP basis set. The trend in affinities can be seen in figure 6.2 compared with MP2 and CCSD data.[215] The authors of Ref. 215 note that the MP2 data is a fair reference given that the errors of the MP2 method and the cc-pVTZ basis set partially cancel.

The use of CAM-B3LYP shows a clear improvement over B3LYP, giving results that are close to MP2 as the chain length increases. This improvement can be traced to the reduced inclination of CAM-B3LYP over B3LYP to delocalise charges—this is consistent with the findings of chapter 3. However, the CAM-B3LYP results are perhaps not as convincing as would be expected and there does remain a noticeable discrepancy relative to the reference MP2 data, although this does go some way to increasing confidence in

DFT results for proton transfer reactions in proteins.

6.2 Modelling the environment

We now consider the interaction between the retinal chromophore and the protein environment. It is through this interaction that it is possible to tune the wavelength at which the chromophore absorbs light.[220,221] One way of tuning this wavelength is through altering the electrostatic interaction of the protonated Schiff base and the protein environment. As the most important contribution to the electrostatic environment of the retinal chromophore in rhodopsins is from negatively charged groups within the binding pocket, Wanko *et al.*[216] investigated the effect by using point charges. They optimised the geometry of pSb5 with a point charge (-1.1 a.u.) placed 2.2 Å from the Schiff base proton. They then calculated the first excitation energy in the presence of a series of charges (0.0 a.u., -0.5 a.u. and -1.1 a.u.) and compared these to the excitation energy at the geometry optimised without any point charge. Through this they were able to probe the effect of the electrostatic environment on the geometry and the excitation energy. We use the same DFT optimised geometry as used by Wanko *et al.* and determine the excitation energies and dipole moments with the TZVP basis set augmented with the diffuse functions from aug-cc-pVDZ.

The excitation energy differences presented in table 6.1 are defined as the excitation energy in the presence of a counterion using the geometry optimised in the presence of a -1.1 a.u. charge relative to the excitation energy of retinal in the presence of no charge using the geometry optimised with no charge. As a reference, we use the high-level *ab-initio* approach of Spectroscopy ORiented Configuration Interaction (SORCI).[222] It can be seen that at all levels of theory, the increase in the magnitude of the charge on the counterion produces an increase in excitation energy. The tendency of the first excitation to increase in energy when in the presence of a stronger counter ion has been attributed to the charge-transfer nature of the transition which involves moving positive charge from the Schiff base to the allyl fragment. As the counterion is located in the vicinity of the Schiff base, this migration of positive charge must work against the electric field generated by the counter ion. A larger counter ion will therefore result in a larger excitation energy. CAM-B3LYP provides the best DFT evaluation of this

Table 6.1: The shift in excitation energy (eV) that occurs when the geometry is optimised in the presence of a point charge (-1.1 au) and when it is not. The excitation energy of the geometry optimised in the presence of the point charge is determined with a range of different counterions.

Theory	Charge=0.0	Charge=−0.5	Charge=−1.1
BP86	-0.07	-0.01	0.08
B3LYP	-0.03	0.04	0.16
CAM-B3LYP	0.02	0.15	0.31
CAM-B3LYP($\alpha+\beta=1$)	0.07	0.23	0.42
HF/CIS	0.09	0.22	0.37
SORCI	0.03	0.28	0.58

Table 6.2: The change in dipole moment caused by the first excitation. The values correspond to $\Delta\mu = \mu(S_1) - \mu(S_0)$ where the dipole moments are calculated using the geometry optimised in the presence of a point charge (-1.1 au).

Theory	Charge=0.0	Charge=−0.5	Charge=−1.1
BP86	1.6	2.1	2.8
B3LYP	2.3	2.8	3.3
CAM-B3LYP	3.2	3.7	3.9
CAM-B3LYP($\alpha+\beta=1$)	4.2	4.4	4.1
HF/CIS	4.3	4.2	3.8
SORCI	6.0	6.6	6.7

difference in excitation energy, however, it still underestimates the difference by almost a factor of 2, relevant to the SORCI reference values.[216]

As a measure of the charge-transfer nature of this excitation, the dipole moment difference can also be calculated as $\Delta\mu = \mu(S_1) - \mu(S_0)$. The dipole moment differences associated with the first excitation are shown in table 6.2. Again, despite only yielding qualitative accuracy, CAM-B3LYP shows the best performance of all DFT functionals. However, the results obtained when using increased fractions of exact exchange above that included in CAM-B3LYP suggest that this may be detrimental to an accurate description, as the trend of increasing shifts with increasing counterion is reversed.

6.3 Effect of ringtwist on excited states

The planarity of the ring system with respect to the polyene chain in the retinal molecule is an important geometrical parameter. It can be controlled by varying the value of the

angle ϕ in figure 6.1. Following Ref. 216, the accuracy of DFT was quantified by comparing excited state energies (figure 6.3), oscillator strengths (figure 6.4) and dipole moment differences ($\Delta\mu$) (figure 6.5) with CC2 values for $39° \leqslant \phi \leqslant 170°$. For this, we use a variety of the protonated Schiff base where R_1 and R_2 in figure 6.1 are both methyl groups. All of the unpublished reference CC2 data has been made available through collaboration with Dr. Marius Wanko and was determined using constrained-optimized PBE0 geometries, which are also used here for the DFT calculations. Again, the TZVP basis set with additional diffuse functions from aug-cc-pVDZ is used.

By considering the CC2 results in figures 6.3, 6.4, and 6.5, it is possible to understand the behaviour of the first two excited states of the pSb of retinal. The S_1 state can be defined as a locally excited (LE) state. The oscillator strength of the $S_0 \rightarrow S_1$ transition is large and remains fairly constant throughout the twist, indicating a large degree of overlap between the occupied and unoccupied orbitals involved. Also, the value of $\Delta\mu$ remains fairly constant throughout the twist indicating little variation in how the charge is redistributed during this excitation. Conversely, the S_2 state is defined as an intramolecular charge transfer (ICT) state. At twist angles corresponding to a perpendicular arrangement of the ring and chain systems, the oscillator strength drops to almost zero for the $S_0 \rightarrow S_2$ excitation, consistent with the relevant occupied and unoccupied orbitals localising on different parts of the molecule. This is reflected in the significant increase in $\Delta\mu$ showing that there is indeed a large degree of charge redistribution at these twist angles.

The results obtained using B3LYP deviate significantly from the reference data. The energies of both excited states are not only underestimated but the behaviour of the S_1 state is entirely incorrect. Additionally, the trends seen in the oscillator strength and $\Delta\mu$ suggest that it is not simply a case of B3LYP giving the incorrect ordering of the lowest two states, but rather that the characters of the excitations are wrong. The results obtained using CAM-B3LYP bear a striking resemblance to the CC2 reference data. The trends in energies are reproduced almost exactly, although the magnitude of the excitation energies are slightly overestimated. Similarly, the trends in oscillator strengths and $\Delta\mu$ are also accurately reproduced. Plots of the B3LYP orbitals involved in the dominant transitions at near-planar and perpendicular twist angles are shown in figure 6.7. The CAM-B3LYP orbitals localise to a lesser extent at the perpendicular

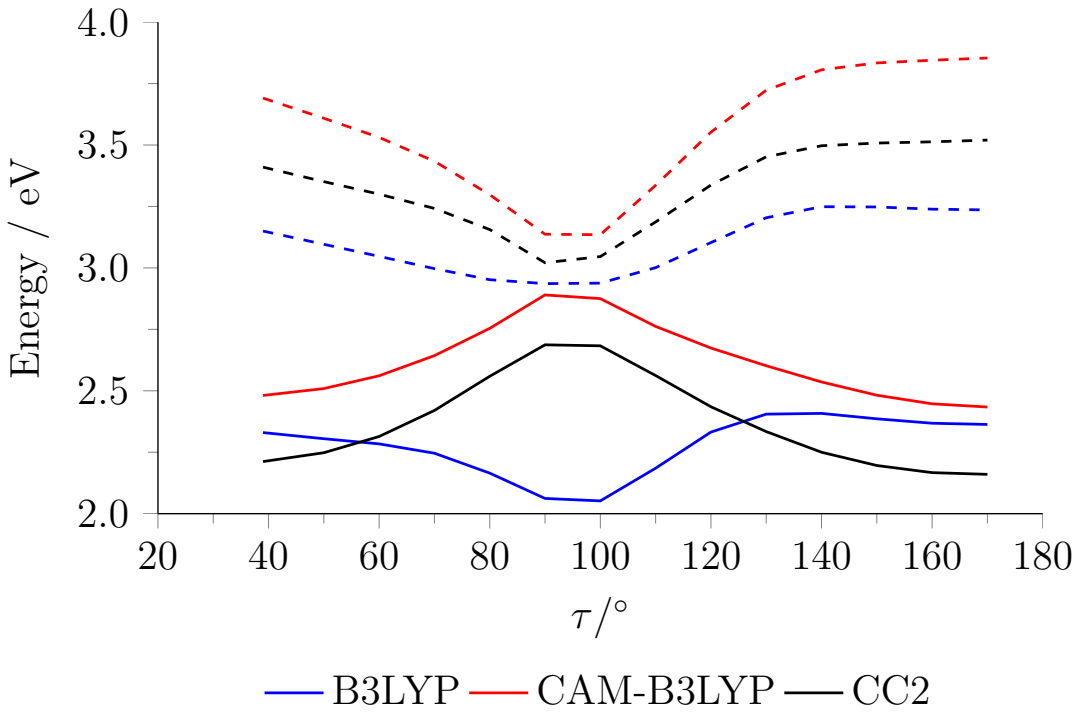

Figure 6.3: Energies of the first (solid) and second (dashed) excited states of the retinal molecule as a function of the twist angle between ring and chain.

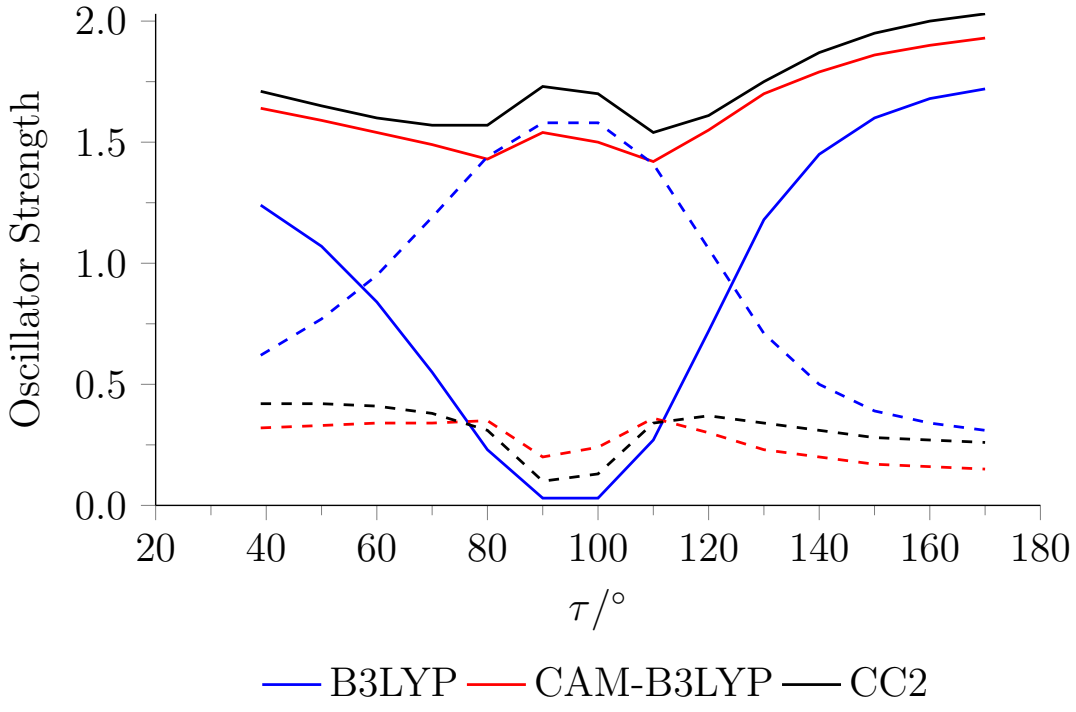

Figure 6.4: Oscillator strengths of the first (solid) and second (dashed) excitations of the retinal molecule as a function of the twist angle between ring and chain.

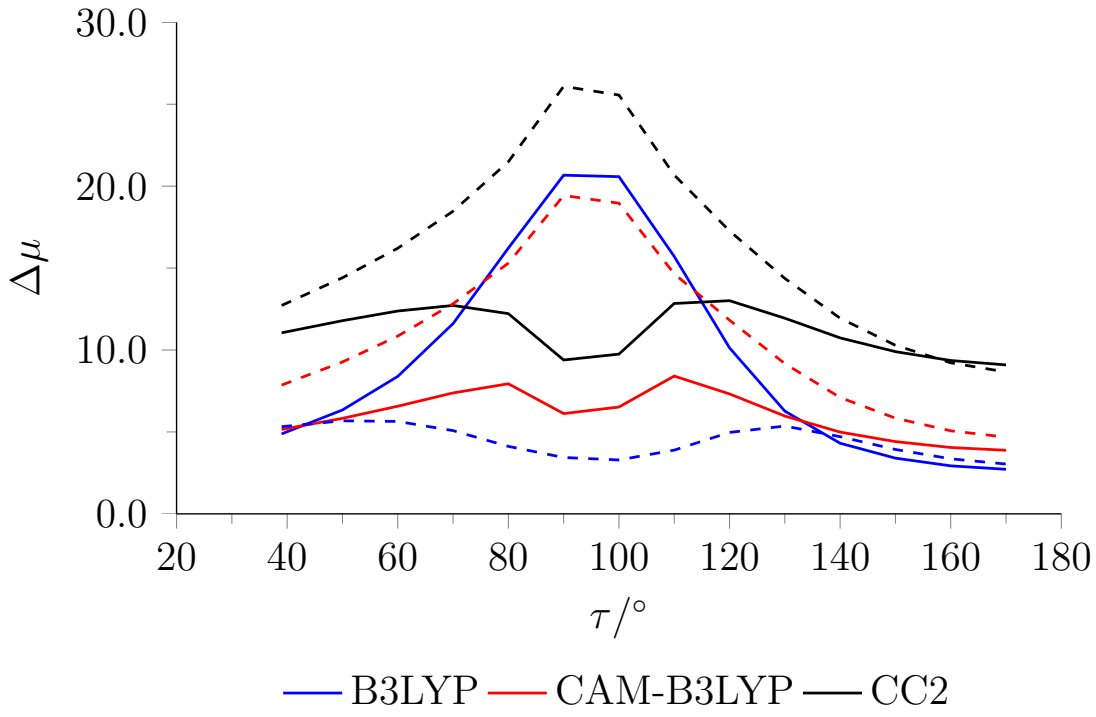

Figure 6.5: Dipole differences ($\Delta\mu$) of the first (solid) and second (dashed) excitations of the retinal molecule as a function of the twist angle between ring and chain.

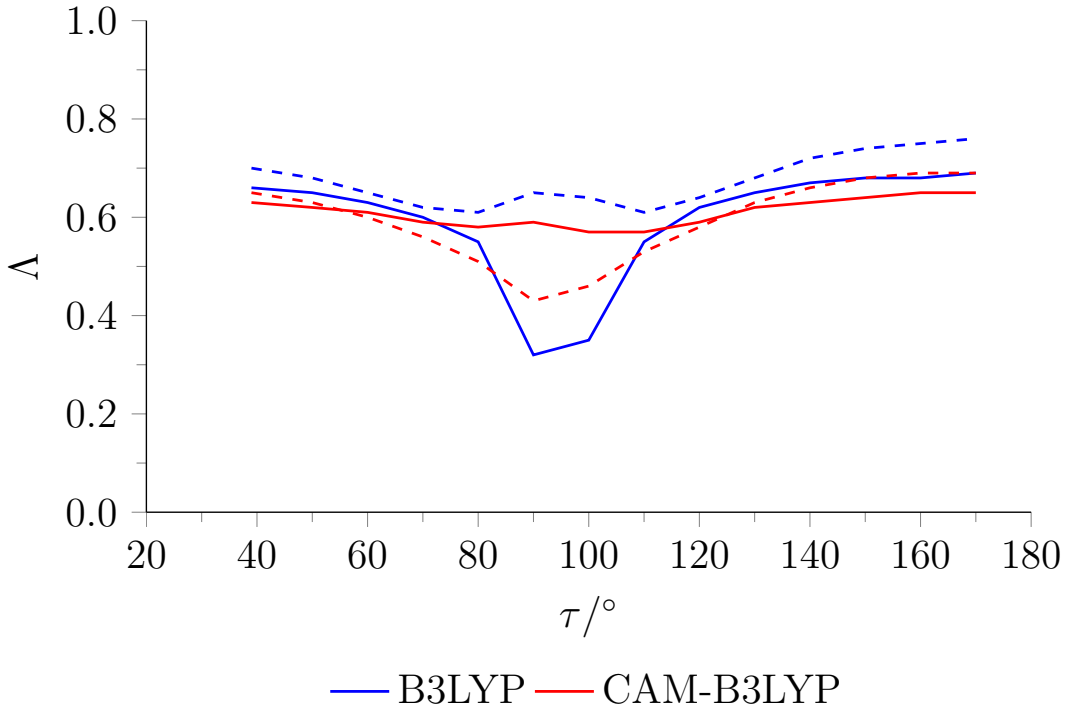

Figure 6.6: Λ diagnostic values of the first (solid) and second (dashed) excitations of the retinal molecule as a function of the twist angle between ring and chain.

geometry but are otherwise indistinguishable.

The failings of B3LYP are now considered, with reference to the more accurate CAM-B3LYP results. At the near-planar geometries of 39° and 170°, the B3LYP and CAM-B3LYP orbitals are essentially indistinguishable. For both functionals, the $S_0 \rightarrow S_1$ excitation is dominated by the HOMO→LUMO transition and the $S_0 \rightarrow S_2$ excitation dominated by HOMO−1→LUMO. This is consistent with the similarity in behaviour between B3LYP and CAM-B3LYP at these angles. It is justifiable to say that B3LYP largely shares the LE and ICT character of the $S_0 \rightarrow S_1$ and $S_0 \rightarrow S_2$ excitations, respectively, seen in CAM-B3LYP at these angles.

However, at perpendicular twist angles the B3LYP and CAM-B3LYP orbitals are no longer indistinguishable. Two differences are observed. Firstly, the ordering of the HOMO and HOMO−1 orbitals is switched between the two approaches. However, as the $S_0 \rightarrow S_1$ and $S_0 \rightarrow S_2$ remain dominated by HOMO→LUMO and HOMO−1→LUMO, respectively, the LE/ICT character is reversed. Secondly, the localisation of the HOMO orbital onto the ring system is more severe when using B3LYP than it is when using CAM-B3LYP. This results in a lower Λ (equation (2.89)) value for the $S_0 \rightarrow S_1$ excitation (figure 6.6).

Now that it has been established that B3LYP gives the correct LE and ICT character of the first and second excitations, respectively, at near-planar geometries, and the incorrect character at near perpendicular geometries, it is possible to quantify the errors in excitation energies. At angles $\phi \leqslant 80°$ and $\phi \geqslant 120°$, the solid lines in figure 6.3 all correspond to the LE state and it can be seen that B3LYP provides a reasonably good estimate. Similarly, the dashed lines correspond to the ICT state which is also reasonably well reproduced. In these circumstances the error is generally less than 0.25 eV. However, at angles $80° < \tau < 120°$, the valid comparisons to make are between the solid black line (CC2 S_1) and dashed blue line (B3LYP S_2) for the LE state and between the dashed black line (CC2 S_2) and solid blue line (B3LYP S_1) for the ICT state. For the former, we can see that the B3LYP LE state is around 0.3 eV too high, which is not a serious problem. However, for the ICT state, B3LYP underestimates the energy by more than 1 eV. This error can be traced to the already understood underestimation of charge-transfer states when using GGA or conventional hybrid functionals. The accurate reproduction of the LE state is unsurprising given the Λ value for this state

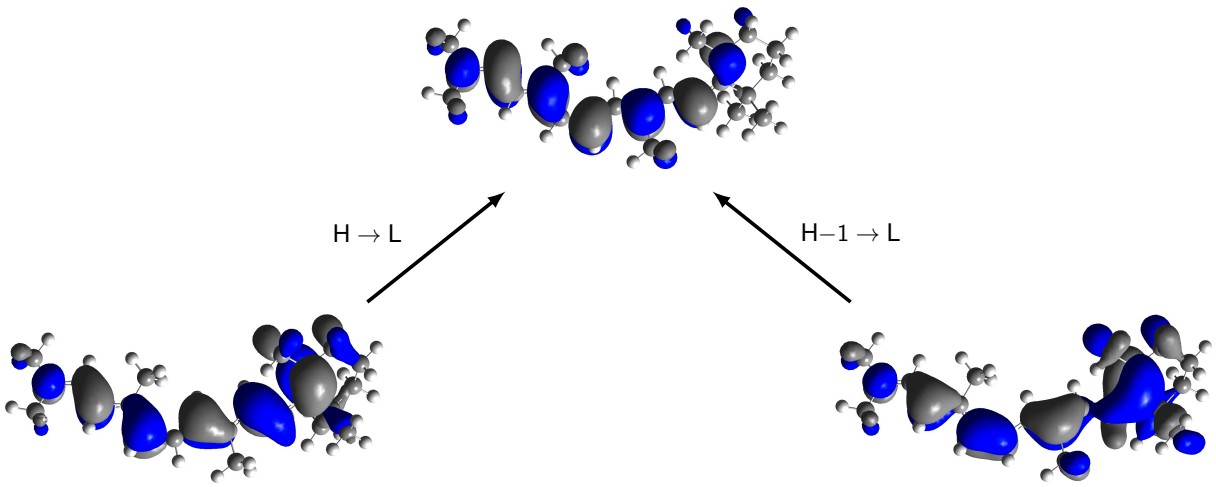

(a) 39°

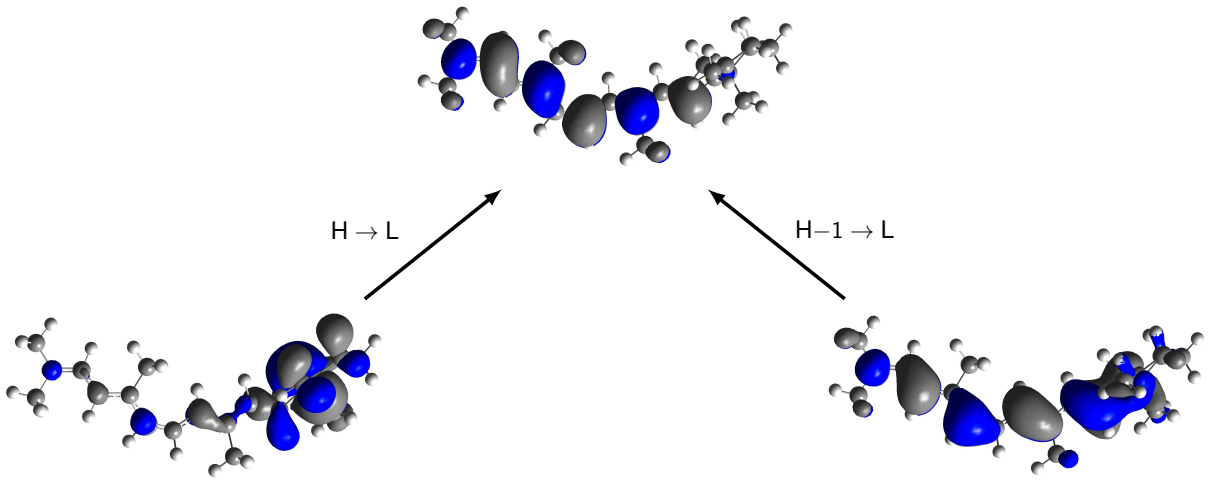

(b) 90°

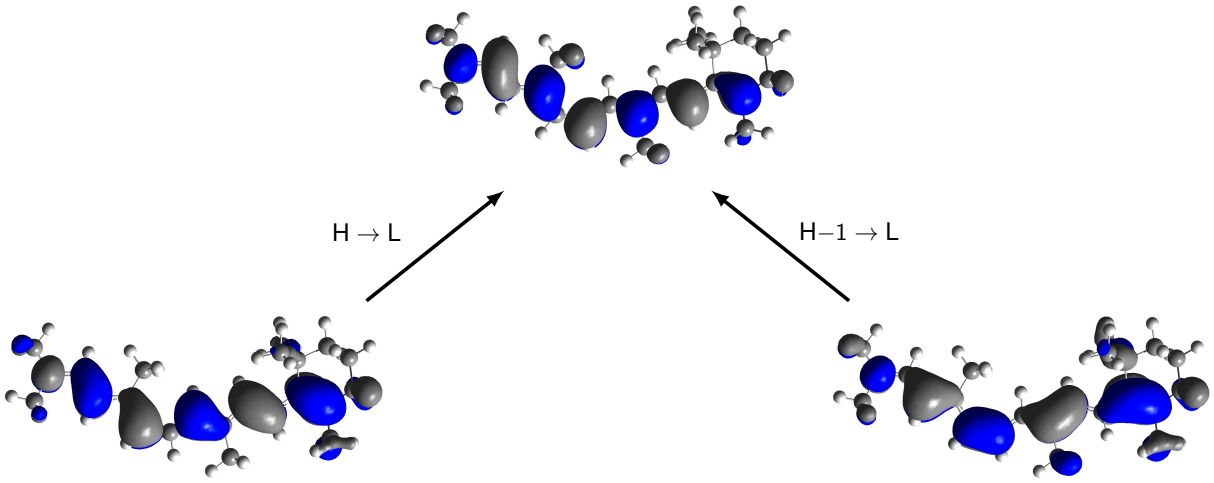

(c) 170°

Figure 6.7: B3LYP orbitals involved in the relevant transitions of the lowest two excitations in retinal at 39°, 90° and 170°. CAM-B3LYP orbitals show slightly more delocalisation at 90° where the HOMO and HOMO−1 orbitals are also switched in order, but are otherwise identical. H=HOMO, L=LUMO.

is consistently ~ 0.6 whereas the underestimation of the ICT state could have been predicted by noting the significant drop in Λ value observable in figure 6.6, which plots Λ for the excitations as a function of the twist angle ϕ. The poor performance of B3LYP is therefore a combined result of charge-transfer failure and an incorrect ordering of the states. The switch in character is well illustrated by the trend in oscillator strengths (figure 6.4) and, to a lesser extent, by the change in dipole moment, $\Delta\mu$ (figure 6.5).

CAM-B3LYP shows a significant improvement over B3LYP. The energies of the two excited states (figure 6.3) closely match those given by CC2 in trend and although they are slightly overestimated, provide a good absolute prediction of the energy. The oscillator strengths (figure 6.4) show a remarkable agreement with the CC2 data confirming that CAM-B3LYP is producing excitations of the correct character. This is further backed up by the trends seen in the dipole differences in figure 6.5.

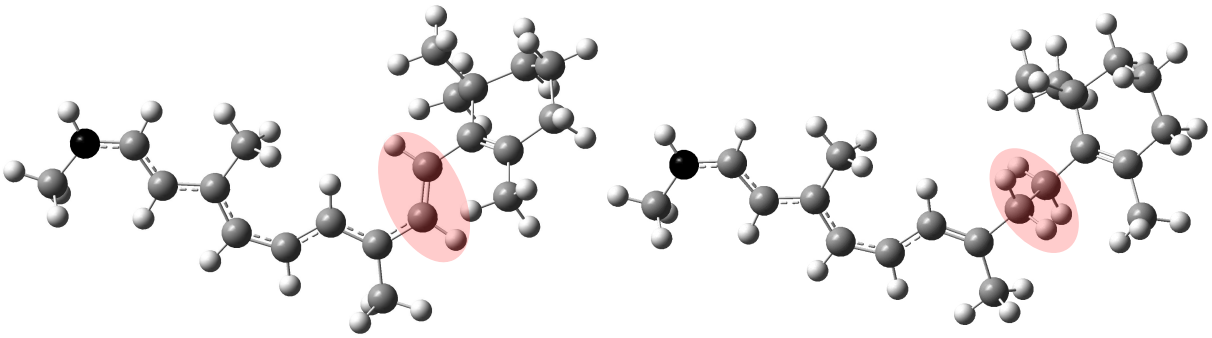

Figure 6.8: The structure of (a) 11-*Z-cis* retinal and (b) 11-*Z-cis*-7,8-dihydro retinal, highlighting the hydrogenation at C7-C8.

6.4 Effect of chemical change on excited states

In this section, it is demonstrated how an analysis involving the Λ diagnostic can provide a useful perspective when considering how a simple chemical change—with seemingly trivial effects on the chemical properties—can significantly affect the accuracy of TDDFT calculations. This is illustrated by the hydrogentation of 11-*Z-cis* retinal to 11-*Z-cis*-7,8-dihydro retinal, as considered by Zaari and Wong[223] and illustrated in figure 6.8. These authors investigated the effect of this chemical change in order to determine the effect of conjugated chain length on the photoisomerization process.[224] They observed that prior to hydrogenation, B3LYP excitation energies and oscillator strengths were in good agreement with reference CC2 data. However, following hydrogenation the B3LYP results showed some large discrepancies in comparison to the reference data. They attributed this to the possibility that the excitations had become charge-transfer in character. We now employ the Λ diagnostic to quantify the degree of charge transfer in the relevant excitations and determine whether or not the errors are reduced when CAM-B3LYP is employed. All calculations are performed at B3LYP/6-31+G(d) optimised geometries and excitation energies are determined with the same 6-31++G(d,p) basis set used by Zaari and Wong. Firstly, the effect of hydrogenation on excitation energy will be considered, followed by the more subtle implications of the chemical change for the oscillator strengths.

The results in table 6.3 show that prior to hydrogenation both of the lowest two excitations have high associated Λ values of 0.68 and 0.72, respectively. As both of these val-

Table 6.3: Vertical excitation energies (eV) and oscillator strengths (in parenthesis) of the retinal chromophore where the C7–C8 bond is unsaturated and saturated, determined using B3LYP, CAM-B3LYP and RI-CC2. The Λ values listed are determined using B3LYP

	B3LYP	CAM-B3LYP	RI-CC2	Λ
11-*Z*-*cis* retinal				
$S_0 \rightarrow S_1$	2.30(1.17)	2.39(1.34)	2.10(1.47)	0.68
$S_0 \rightarrow S_2$	3.04(0.24)	3.63(0.21)	3.30(0.26)	0.72
11-*Z*-*cis*-7,8-dihydro retinal				
$S_0 \rightarrow S_1$	1.53(0.08)	2.82(0.44)	2.62(0.64)	0.23
$S_0 \rightarrow S_2$	3.05(0.90)	3.23(0.98)	3.03(0.88)	0.54
$S_0 \rightarrow S_3$	3.25(0.39)	4.70(0.01)	4.40(0.01)	0.30

ues are well above the threshold[84] ($\Lambda \sim 0.3$), no breakdown in TDDFT accuracy should be expected and the excitation energies are in good agreement with CC2. These two excitations are comprised, almost exclusively, of HOMO→LUMO and HOMO−1 →LUMO orbital transitions, respectively. These transitions are shown in figure 6.9 where it is clear that all three orbitals involved are delocalized across the entire molecule including both the chain and ring components.

Following hydrogenation, only the $S_0 \rightarrow S_2$ excitation has an associated Λ value above the threshold, at 0.54. No breakdown in TDDFT accuracy is predicted for this excitation and, indeed, the B3LYP results are in good agreement with the reference data. However, for the $S_0 \rightarrow S_1$ and $S_0 \rightarrow S_3$ transitions, the Λ values are significantly smaller, falling in the region where breakdown for B3LYP excitation energies is predicted. Accordingly, for both of these excitations, the energy is significantly underestimated—by more than 1 eV in both cases relevant to the CC2 data. The presence of both high and low Λ transitions following hydrogenation is a result of the breaking of conjugation between the ring and chain systems. It is no longer possible for orbitals to be delocalized across the entire molecule, instead they must localise on either the ring or the chain. This localisation of the orbitals can be seen in figure 6.10.

The high-Λ value associated with the $S_0 \rightarrow S_2$ excitation is a result of it being predominantly HOMO−1→LUMO in character, which is a chain-to-chain transition. In contrast, both the $S_0 \rightarrow S_1$ and $S_0 \rightarrow S_3$ transitions are predominantly the ring-to-chain HOMO→LUMO and HOMO−2→LUMO transitions, resulting in significantly smaller Λ values. The charge-transfer nature of the $S_0 \rightarrow S_1$ excitation alluded to in the

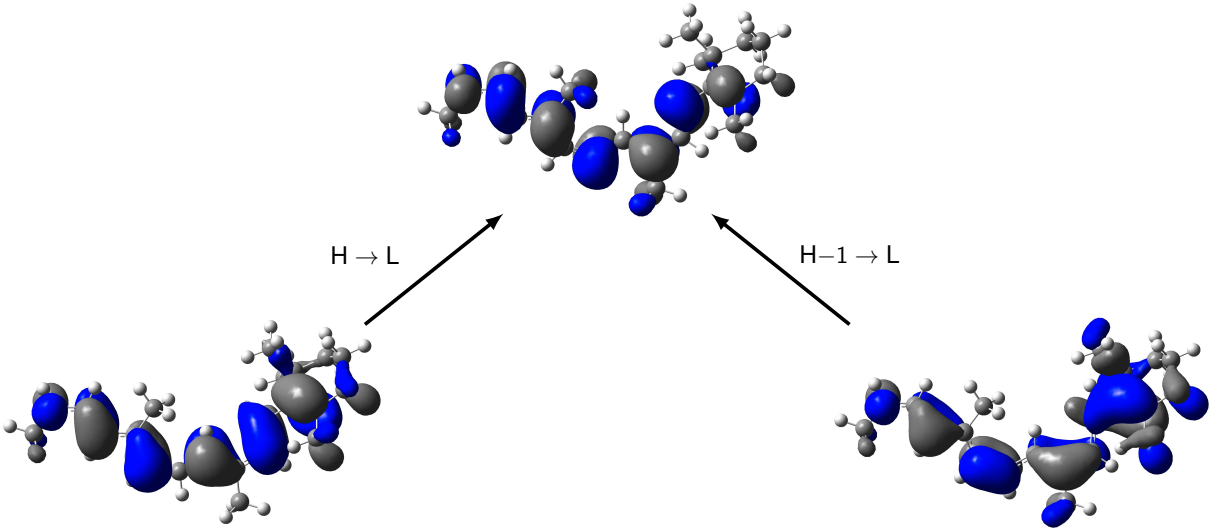

Figure 6.9: Orbital transitions in 11-*Z-cis* retinal, determined using B3LYP. H=HOMO, L=LUMO.

orbital plots presented by Zaari and Wong has now been explicitly quantified—in terms of occupied-unoccupied orbital overlap—by using the Λ diagnostic.

B3LYP predicts the $S_0 \rightarrow S_1$ excitation to have a low oscillator strength and the $S_0 \rightarrow S_3$ to have a high oscillator strength, the opposite of that given by the reference CC2 results. This incorrect ordering can be understood by considering the explicit orbital transitions which contribute to the excitations. Excitations that are ring-to-chain in character and, as a result, have a low-Λ value must, necessarily, have a low oscillator strength. The low oscillator strength of the $S_0 \rightarrow S_1$ excitation is therefore a result of it being comprised almost exclusively of a HOMO→LUMO transition. In contrast, although the $S_0 \rightarrow S_3$ excitation is predominantly HOMO−2→LUMO, it does involve a significant chain-to-chain HOMO−1→LUMO contribution. It is the presence of the latter contribution which results in the large oscillator strength. In a similar manner, the $S_0 \rightarrow S_2$, although predominantly HOMO−1→LUMO in character, does contain some HOMO−2→LUMO contribution. This mixing of characters reflects the similarity in energy of the two excitations. The $S_0 \rightarrow S_1$ excitation is much lower in energy and therefore, no mixing is seen for this state.

When using CAM-B3LYP, all excitation energies are higher than when using B3LYP. The result of this is that all excitation energies are slightly overestimated compared to the reference CC2 data. However, the $S_0 \rightarrow S_1$ and $S_0 \rightarrow S_3$ excitations following hydrogenation are of a comparable accuracy to all other excitations, whereas they were

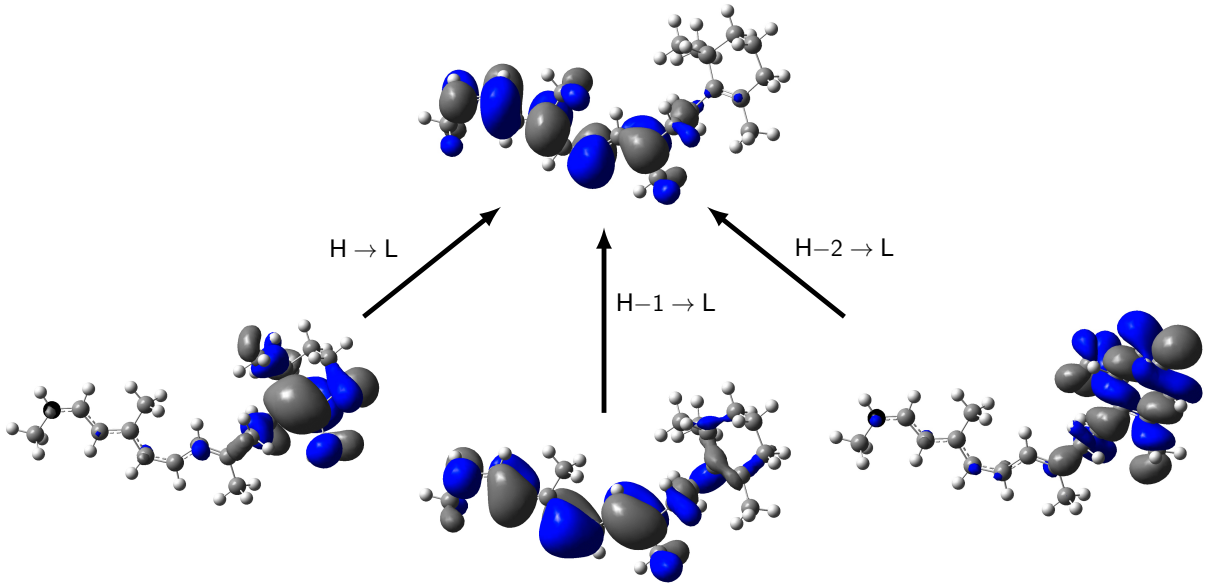

Figure 6.10: Orbital transitions in 11-*Z*-*cis*-7,8-dihydro retinal, determined using B3LYP. H=HOMO, L=LUMO.

significantly underestimated when using B3LYP. CAM-B3LYP therefore provides excitations whose errors are independent of Λ value and are all in error to the same degree as the best results provided by B3LYP. Additionally, the incorrect ordering of the B3LYP oscillator strengths has now been resolved by using CAM-B3LYP, resulting in consistency with CC2. The relevant CAM-B3LYP orbitals are indistinguishable from the B3LYP orbitals and the dominant orbital transitions are also the same. The explicit orbital transitions involved in the excitations now show the opposite behaviour to that seen in B3LYP—the $S_0 \rightarrow S_1$ excitation, although predominantly HOMO→LUMO in character, contains a significant HOMO−1→LUMO contribution resulting in a large oscillator strength. The $S_0 \rightarrow S_3$ is almost exclusively HOMO−2→LUMO, with no other significant contributions, resulting in a small oscillator strength. This different mixing arising in CAM-B3LYP is a reflection of the fact that it is now the $S_0 \rightarrow S_1$ and $S_0 \rightarrow S_2$ excitations which are similar in energy, while the $S_0 \rightarrow S_3$ excitation is significantly higher in energy.

Summary

It has previously been noted that "the application of DFT to proton transfer reactions in retinal proteins is not straightforward and should be pursued with some care",[215] but

it has been shown here that through the application of CAM-B3LYP, a greater degree of confidence can be placed in DFT results relating to proton affinities. Also, when concerned with the environment of chromophores and how they affect the behaviour, CAM-B3LYP shows significantly better qualitative accuracy than conventional GGA and hybrid functionals. However, in both cases, quantitative accuracy is not achieved through the use of CAM-B3LYP.

It has also been shown that an orbital overlap perspective can be useful for understanding why simple physical and chemical changes can lead to a significant reduction in TDDFT accuracy. This breakdown can manifest itself as errors in both the character and energy of excitations. It has also been illustrated how such errors can easily be predicted through the same orbital overlap perspective. Errors in oscillator strengths can be understood in terms of orbital transition contributions. All of these errors are largely eliminated by the use of CAM-B3LYP. It can be inferred from the example of Retinal used in this chapter that *any* physical or chemical process that sufficiently reduces the overlap will degrade the TDDFT accuracy when conventional GGA and hybrid functionals are being used.

Chapter 7

The character of molecular excited states: $C_3H_4N_2$

Through the analysis of a specific molecular example, the topographical accuracy of excited state potential energy surfaces is investigated. The accuracy of local and charge-transfer excitations is assessed for PBE (a representative GGA functional) and CAM-B3LYP. Both singlet and triplet excitations are considered, where the latter are determined through the commonplace TDDFT approach and the less frequently employed ΔSCF method. Of particular interest is the effect on the *character* of the excited states—the charge-transfer error arising in TDDFT with GGA functionals can manifest itself in the character, as opposed to the energy. By employing CAM-B3LYP, issues present when using GGA functionals are largely eliminated. The charge-transfer error arising with GGA functionals within TDDFT does not present itself when the ΔSCF approach is used. The characters of TDDFT and ΔSCF excitations are reconciled through appropriate combinations of orbitals. The lack of symmetry in the molecule means that the effect of avoided crossings is significant.

The accuracy of long-range charge-transfer (CT) excitations from DFT has already been considered in chapters 5 and 6. In section 5.1.8, the ordering and character of charge-transfer excited states for a series of extended, conjugated pyrene derivatives was shown to be in error when using B3LYP. In sections 6.3 and 6.4, the incorrect character of excitations in retinal resulted in significant errors in the oscillator strengths. A recent study on tripeptides[84] showed that charge-transfer excitations have significantly different character when determined using functionals with a range of exact exchange. Other studies,[225–227] as well as the content of chapter 6, have shown how the accuracy of

potential energy surfaces depends strongly on the choice of functional. In this chapter, we combine these two issues (character of excitations and accuracy of surfaces) for which conventional functionals fail and consider whether CAM-B3LYP can provide a more satisfactory description.

Wiggins *et al.* considered the well known charge-transfer compound 4-(dimethylamino) benzonitrile (DMABN).[226] In their study, they constructed potential energy surfaces as the sum of the ground state energy and vertical excitation energies determined using TDDFT. They noted that "If the spatial overlap between the occupied and virtual orbitals involved in the excitation has a strong dependence on the nuclear conformation, then the accuracy of the surface will not be uniform." The result of this is that regions of the potential energy surface corresponding to high overlap are well described and regions corresponding to low overlap are poorly described, when conventional GGA and hybrid functionals are used. They were able to resolve this issue through the use of CAM-B3LYP, for which they found no correlation between Λ value and TDDFT accuracy. CAM-B3LYP exhibited excellent agreement with reference CC2 data. This same issue arose in the character of the lowest two excited states of Retinal in section 6.3.

We now employ a similar compound to DMABN to generate a similar situation for which we can assess the performance of both TDDFT and ΔSCF (a method used here for determining triplet excitation energies, which will be defined later). We pay particular attention to the description of the *character* of excitation as a function of a twisting angle and the relative performance of each approach. In the discussion that follows, the term "transition" is used to refer to a particular occupied–unoccupied orbital pair whereas "excitation" refers to the overall combination of transitions in the electronic excitation.

The molecule $C_3N_2H_4$ (figure 7.1) is smaller than DMABN but captures the same fundamental chemistry. The dimethylamino group in DMABN is replaced with the simplest possible amine group. The central ring system in DMABN is replaced with a single double bond which retains the conjugation that exists through the molecule. So, the functionality of the molecule has been retained but the structure is smaller, allowing a more extensive analysis to be performed. Although $C_3N_2H_4$ is not expected to exactly reproduce the behaviour of DMABN, it is expected that the similar combination of functional groups will give rise to similarly interesting behaviour.

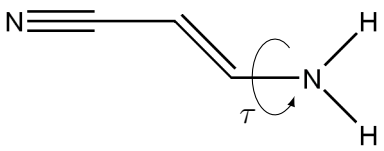

Figure 7.1: The structure of $C_3N_2H_4$ with the C—N bond around which the twist occurs indicated by τ.

All calculations are performed using the PBE GGA functional and CAM-B3LYP, in order to quantify the effect of attenuated exchange on the behaviour. A hybrid functional, with constant exchange, such as B3LYP, is expected to have an intermediate behaviour between these two functionals. CCSD calculations have been performed as a reference. All calculations are performed with the aug-cc-pVTZ basis set; full surfaces are mapped with DFT while selected geometries are used for the CCSD calculations to reduce computational cost. The structures are optimised (MP2/6-31G*) within the constraint that the amine group remains planar. This constraint removes the complication of pyramidalisation seen in the amine group when the molecule is twisted away from the fully planar geometry. At angles of $\tau = 0°$ and $90°$, the molecule has C_s symmetry and the excited states therefore have either A′ or A″ symmetry. At all intermediate twist angles the mirror plane is lost resulting in C_1 symmetry and all excited states are of A symmetry.

Firstly, the TDDFT energy, the Λ value and the oscillator strength of the lowest three *singlet* states of $C_3N_2H_4$ are considered as a function of the twist angle. Secondly, the energy and the Λ value of the lowest three *triplet* states are considered—the oscillator strengths for triplet states are by definition zero. The results are compared with those from the ΔSCF approach. In all cases, particular attention is paid to the *character* of the state.

7.1 Singlet excited states of $C_3N_2H_4$

PBE TDDFT Singlets

Figure 7.2 presents plots of the TDDFT energy, Λ value and oscillator strength for the lowest three singlet excited states of $C_3N_2H_4$, as a function of twist angle ϕ, determined

Table 7.1: Energies (eV) of the lowest three singlet excited states of $C_3N_2H_4$ at 0° and 90°.

Angle	State	PBE	CAM-B3LYP	CCSD
0°	1st	4.43 (R)	5.15 (R)	5.34 (R)
	2nd	5.06 (R)	5.50 (LE)	5.67 (LE)
	3rd	5.24 (LE)	5.67 (R)	5.99 (R)
90°	1st	3.36 (CT)	5.13 (CT)	5.64 (CT)
	2nd	5.19 (R)	6.51 (R)	6.63 (R)
	3rd	5.38 (R)	6.70 (LE)	7.28 (LE)

using PBE. The excitation energies and characters of the lowest three singlet states at 0° and 90° are shown in table 7.1 where it can be seen that all of the PBE energies are underestimated relative to the CCSD reference values. At $\tau = 0°$, the lowest two PBE states are of Rydberg character.

The diabatic states corresponding to the two Rydberg transitions can be identified in figure 7.2(a): The first Rydberg transition is denoted by the blue surface followed by red with the jump between the two surfaces occuring at $\sim 45°$; the second Rydberg transition is red followed by green with the jump at $\sim 20°$. The energies (figure 7.2(a)) of these transitions are reasonably constant; the orbitals vary little upon twisting. Both transitions exhibit consistently low Λ values (blue followed by red and red followed by green in figure 7.2(b))—below the threshold value of ~ 0.4. It is therefore predicted that the energy of these two states is underestimated when using PBE. At both $\tau = 0°$ and 90°, the energy of the second Rydberg state is sufficiently underestimated for it to drop below the locally excited (LE) state, giving an incorrect state ordering.

At $\tau = 0°$, the third state is of local character and becomes a charge-transfer state at $\tau = 90°$. This state decreases in energy during the twist, intersecting the second Rydberg state at $\sim 10°$ and the lowest Rydberg state at 45°. The evolution of the locally excited state to a charge-transfer state corresponds to the diabatic state which can be identified in figure 7.2 as green, followed by red, followed by blue. It is clear from this transition that at twist angles of $\tau > 60°$, there is a significant drop in the value of Λ, indicating that this excitation is indeed adopting charge-transfer character. This explains why the state is underestimated relative to CCSD by only 0.43 eV at 0° but 2.28 eV at 90° (see table 7.1). This transition, which is of local character at $\tau = 0°$ and

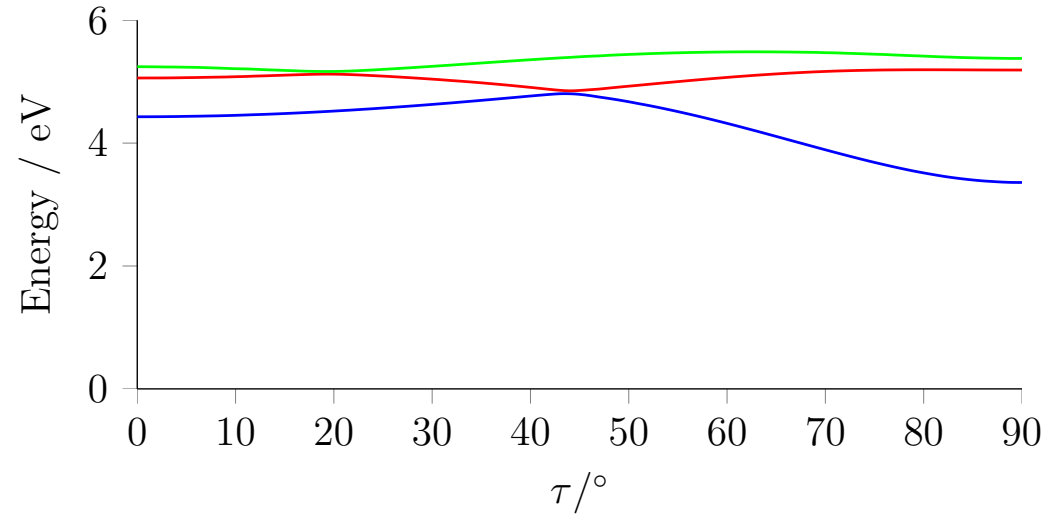

(a)

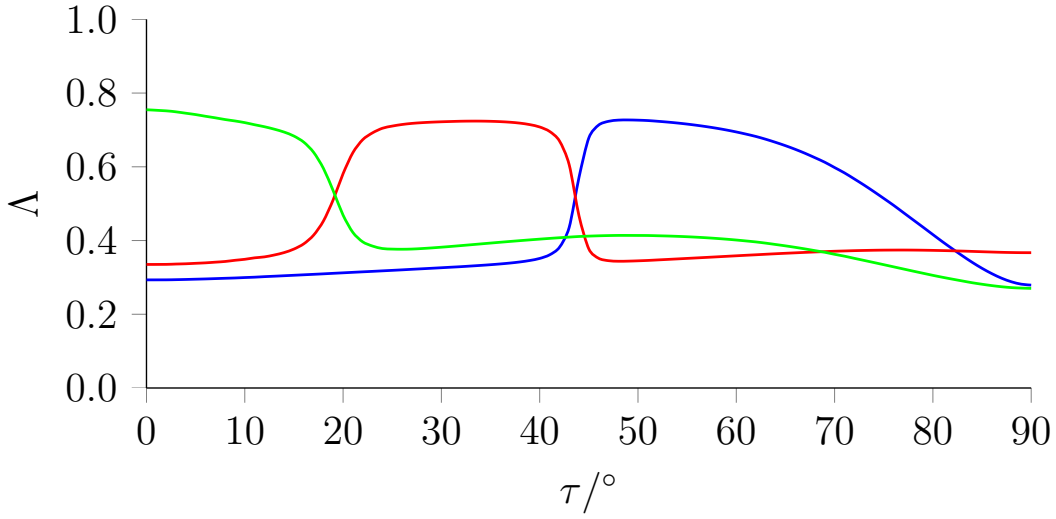

(b)

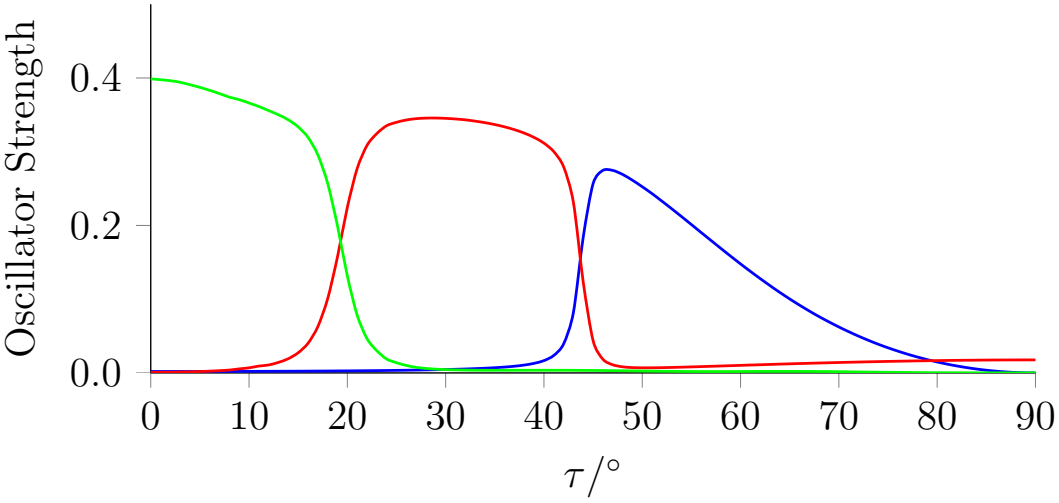

(c)

Figure 7.2: Plots of the TDDFT (a) Energy, (b) Λ value and (c) oscillator strength as a function of the twist angle τ for the lowest three singlet excited states of $C_3N_2H_4$ calculated using PBE. 1^1A blue, 2^1A red and 3^1A green.

charge-transfer character at $\tau = 90°$ will hereafter be referred to as LE→CT.

The dominant orbital transitions for the lowest PBE singlet *state* (the blue curve in figure 7.2(a)) are plotted in figure 7.3. It is clear that before 45° the state is of Rydberg character. After the avoided crossing at this angle, the state has local character which, due to the twisting of the molecule, eventually adopts charge-transfer character at 90° as a result of the HOMO orbital localising on the amine. This evolution of an locally excited state into a charge-transfer state upon twisting of the amine group is exactly as observed by Wiggins *et al.* for DMABN. The effect of the charge-transfer underestimation by PBE is evident from a comparison of the curves in figure 7.2(a) and the CCSD equivalent plotted in figure 7.4 where it is evident that the lowest state becomes increasingly underestimated at larger twist angles.

The oscillator strengths for the lowest three excitations are plotted in figure 7.2(c). The form of all three curves accurately reflects that seen for the Λ values. This is unsurprising given the relationship between Λ and the oscillator strength highlighted in chapter 6.

CAM-B3LYP TDDFT Singlets

Figure 7.5 presents plots of the TDDFT energy, Λ value and oscillator strength for the lowest three singlet excited states of $C_3N_2H_4$ as determined using CAM-B3LYP. It is clear from the results in table 7.1 that CAM-B3LYP provides a significantly improved performance over PBE. Not only are the energies in significantly better agreement with the reference CCSD values than when using PBE, but the correct ordering of the states at both 0° and 90° is reproduced. Furthermore, CAM-B3LYP shows an improved qualitative description of the behaviour of the lowest three singlet excited states during the twist, as illustrated by the similarity to the CCSD curves in figure 7.4.

The improved description of Rydberg states with CAM-B3LYP increases their energy, the result being that the second Rydberg state at 0° is above the locally excited state, thus removing the first avoided crossing seen at $\sim 10°$ when using PBE. The LE→CT transition, being the 2nd state at 0° now only intersects the lowest Rydberg state. It still produces the same significant drop in Λ value for angles of $\tau > 60°$ (red followed by blue in figure 7.5(b)), but not the corresponding drop in energy seen when using PBE. This is essentially the same observation made by Wiggins *et al.* for the

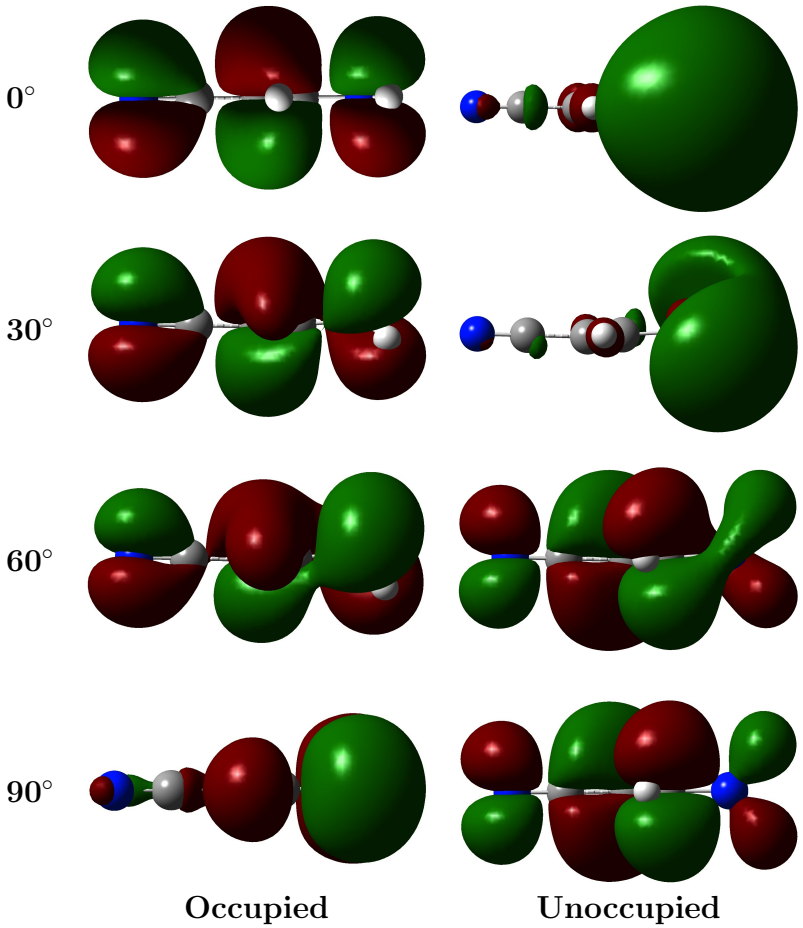

Figure 7.3: The evolution of the PBE ground state occupied and unoccupied orbitals involved in the dominant transition of the first singlet excited state, with increasing twist angle τ.

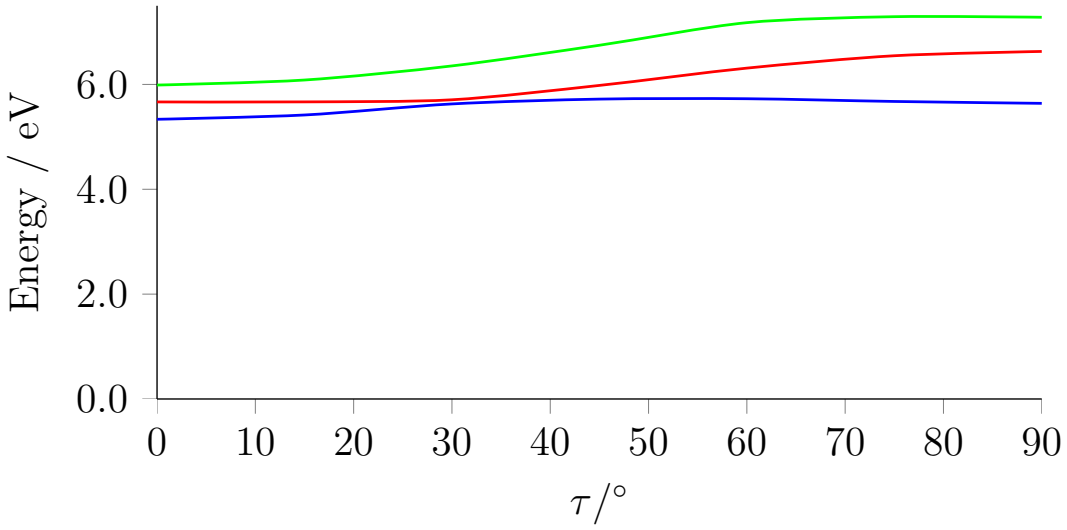

Figure 7.4: Plot of the Energy as a function of the twist angle τ for the lowest three singlet excited states of $C_3N_2H_4$ calculated using CCSD. 1^1A blue, 2^1A red and 3^1A green.

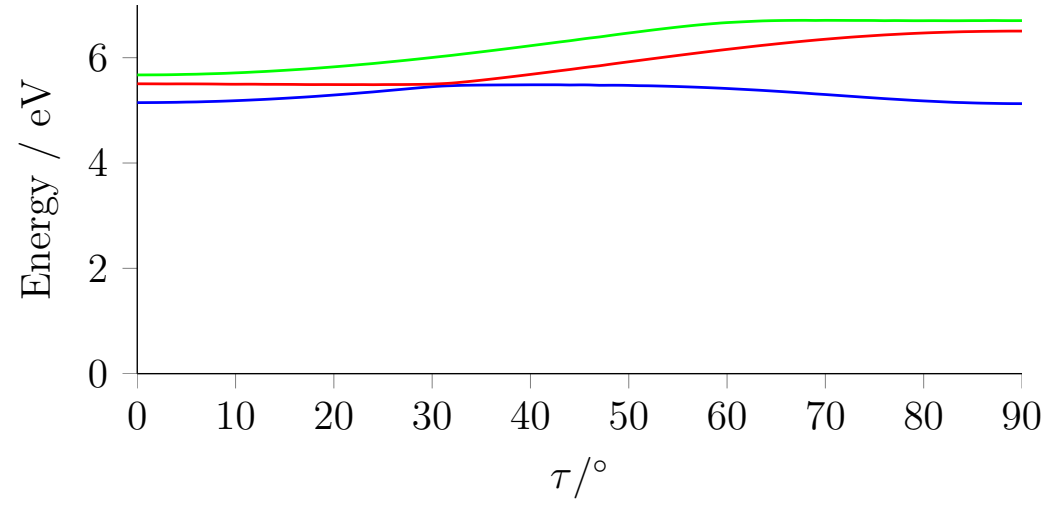

(a)

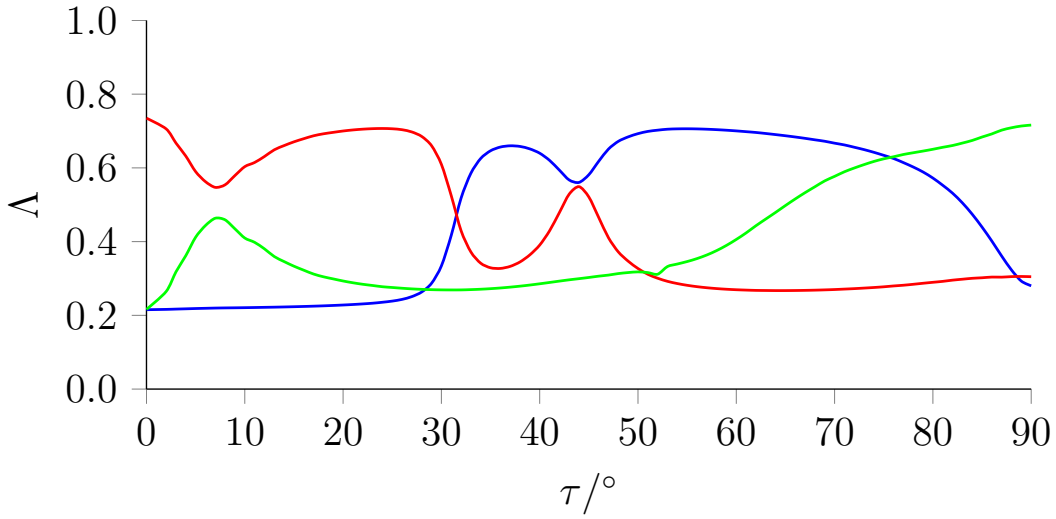

(b)

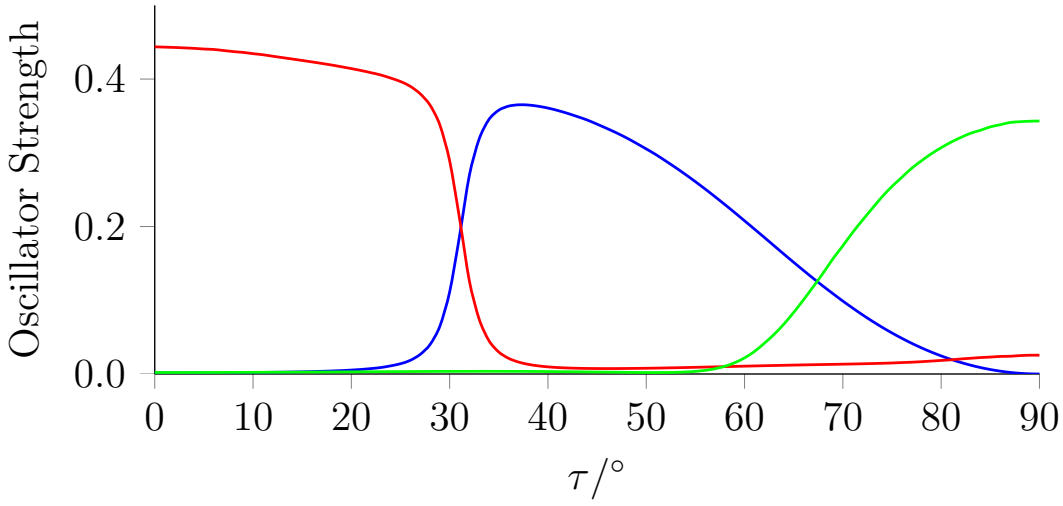

(c)

Figure 7.5: Plots of the TDDFT (a) Energy, (b) Λ value and (c) oscillator strength as a function of the twist angle τ for the lowest three singlet excited states of $C_3N_2H_4$ calculated using CAM-B3LYP. 1^1A blue, 2^1A red and 3^1A green.

performance of CAM-B3LYP compared to PBE in DMABN.

There are features which occur in the plot of Λ (figure 7.5(b)) at $\tau \sim 10°$ and $\sim 45°$ which are not seen in the energy or oscillator strength. At $\tau = 10°$ the red and green curves approach one another; at 45° the blue and red curves do the same. These features arise because there is a re-ordering of the CAM-B3LYP virtual orbitals during the twist. At $\sim 10°$ the LUMO+1 and LUMO+2 orbitals switch character and at $\sim 45°$ the LUMO and LUMO+1 orbitals switch character. This can be seen in the plot of orbital energies as a function of twist angle shown in figure 7.6. The effect of an orbital re-ordering is simply to change the labels of the orbitals involved in the transition before and after the feature. There is no change in the character of the excitation. However, there is a significant change in the orbitals involved at the switch point. The orbitals mix as they become degenerate in energy, to produce orbitals different from those seen before or after the switch. Figure 7.7 shows the orbitals involved in the two dominant transitions of the lowest CAM-B3LYP excited state at 45°. At this angle, the locally excited state (figure 7.5(b), blue curve) adopts some Rydberg character, lowering the value of Λ. Correspondingly, the Rydberg state (red curve) adopts some local character, raising the value of Λ. Aside from this additional feature, the orbitals involved in the lowest state when using CAM-B3LYP are similar to those seen with PBE (figure 7.3) although the avoided crossing with the second state, responsible for a switch from Rydberg to local character, occurs at an earlier twist angle of $\sim 30°$.

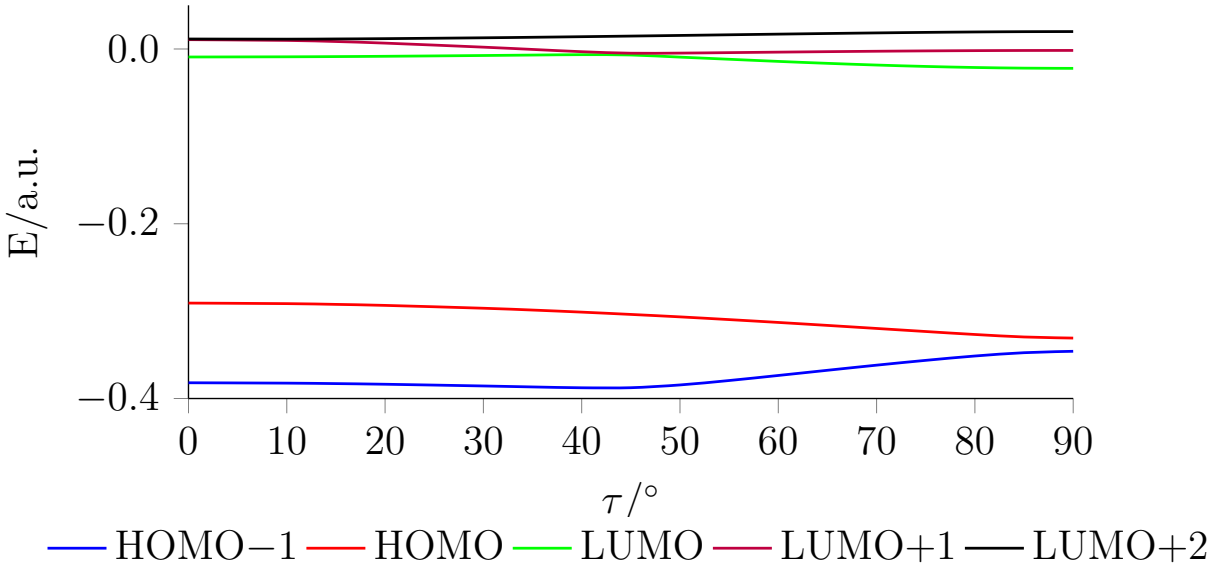

Figure 7.6: The variation in orbital energies with twist angle when using CAM-B3LYP

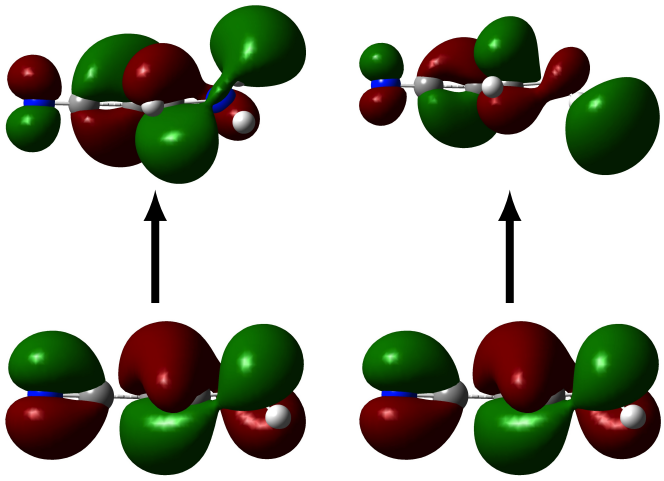

(a) HOMO→LUMO (b) HOMO→LUMO+1

Figure 7.7: The dominant orbital transitions involved in the lowest singlet excited state at 45° using CAM-B3LYP.

7.2 Triplet excited states of $C_3N_2H_4$

The development of TDDFT and its ability to produce accurate energies for locally excited states when using conventional GGA and hybrid functionals has led to its widespread application to singlet excited states. Although there have been applications of TDDFT to the determination of triplet states in small molecules in the past,[71] there has recently been an increase in interest in this area and the publication of a number of extensive studies.[228,229] The main finding of these studies is that TDDFT often underestimates triplet excitation energies relative to reference data.

7.2.1 TDDFT Triplets

PBE TDDFT Triplets

Figure 7.8 presents plots of the TDDFT energies and Λ values for the lowest three triplet excited states of $C_3N_2H_4$ determined using PBE. Again, from the data shown in table 7.2 it is clear that PBE underestimates the energy of all states in comparison to CCSD. When using PBE, the lowest excited triplet state does not experience an avoided crossing with any of the other states. The dominant transition in this state is similar to that seen in the singlet analysis, involving a local excitation evolving into a charge-transfer excitation. However, now this state is uninterrupted by avoided crossings and the dominant transitions for the lowest PBE triplet *state* are plotted in figure 7.9. Note that the orbital transitions involved at $\tau = 60°$ and 90° in figure 7.9 are indistinguishable from those already seen for the singlets in figure 7.3. The evolution of the lowest state into one of charge-transfer character is evident in the dropping off of the Λ value as the twist progresses. It should therefore again be expected that at angles approaching $\tau = 90°$, the energy of this state will be underestimated. Indeed, as can be seen from the results in table 7.2, the locally excited transition at 0° is underestimated by 0.38 eV, whereas at 90°, the charge-transfer state into which it has evolved is underestimated by 1.64 eV—significant enough for the charge-transfer state to incorrectly be the lowest state when using PBE.

The second state is a Rydberg state and, similar to the behaviour seen in the singlet excitations, the transition changes little during the twisting procedure. This state does undergo an avoided crossing with the third state at $\tau \sim 50°$. It can therefore be seen

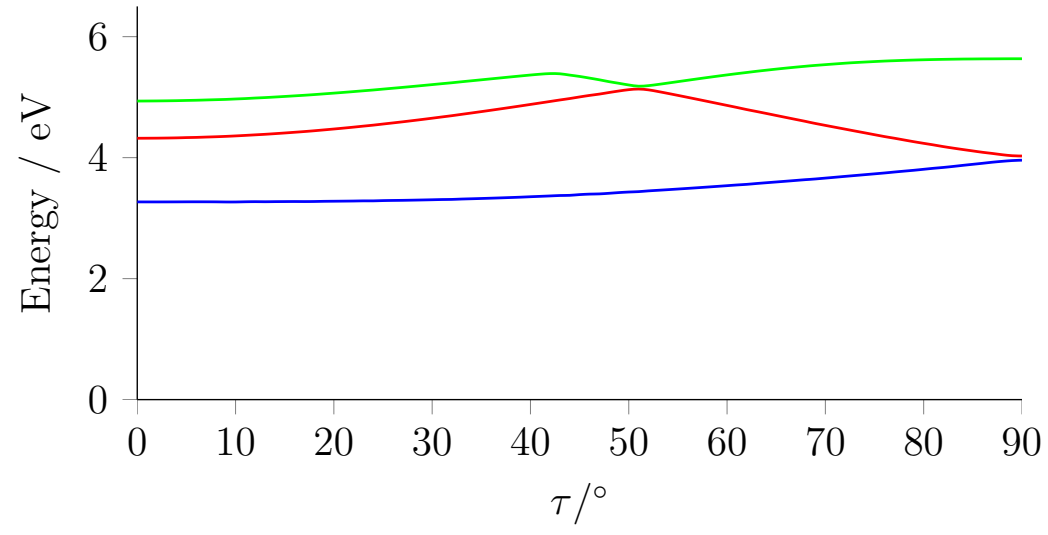

(a)

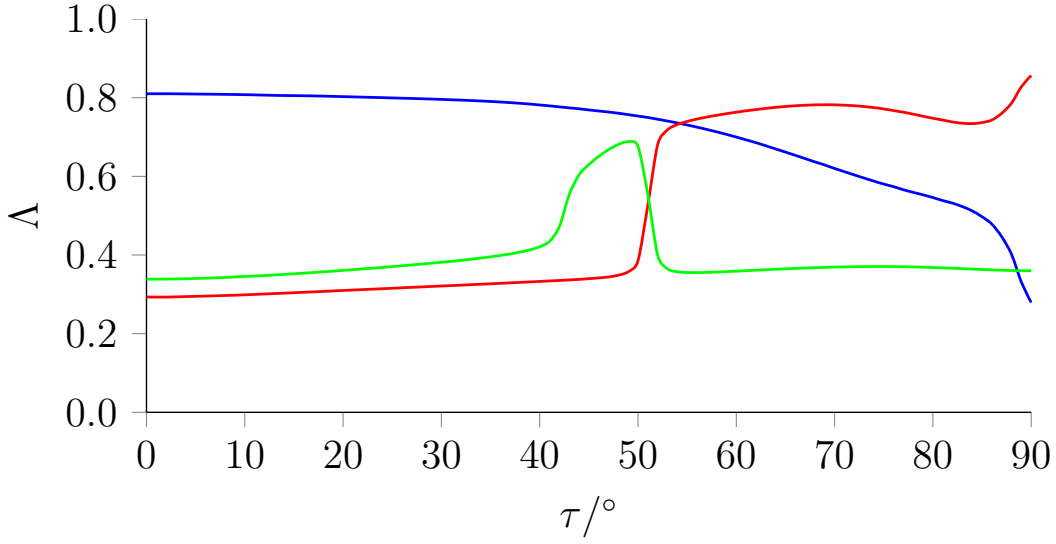

(b)

Figure 7.8: Plots of the TDDFT (a) Energy and (b) Λ value as a function of the twist angle τ for the lowest three triplet excited states of $C_3N_2H_4$ calculated using PBE. 1^3A blue, 2^3A red and 3^3A green.

Table 7.2: Energies (eV) of the lowest three triplet excited states of $C_3N_2H_4$ at 0° and 90°.

Angle	State	PBE	CAM-B3LYP	CCSD
0°	1st	3.27 (LE)	3.09 (LE)	3.65 (LE)
	2nd	4.32 (R)	5.02 (R)	5.21 (R)
	3rd	4.94 (R)	5.35	5.90 (R)
90°	1st	3.96 (CT)	3.67 (LE)	4.28 (LE)
	2nd	4.03 (LE)	5.02 (CT)	5.60 (CT)
	3rd	5.63 (R)	6.14	6.69

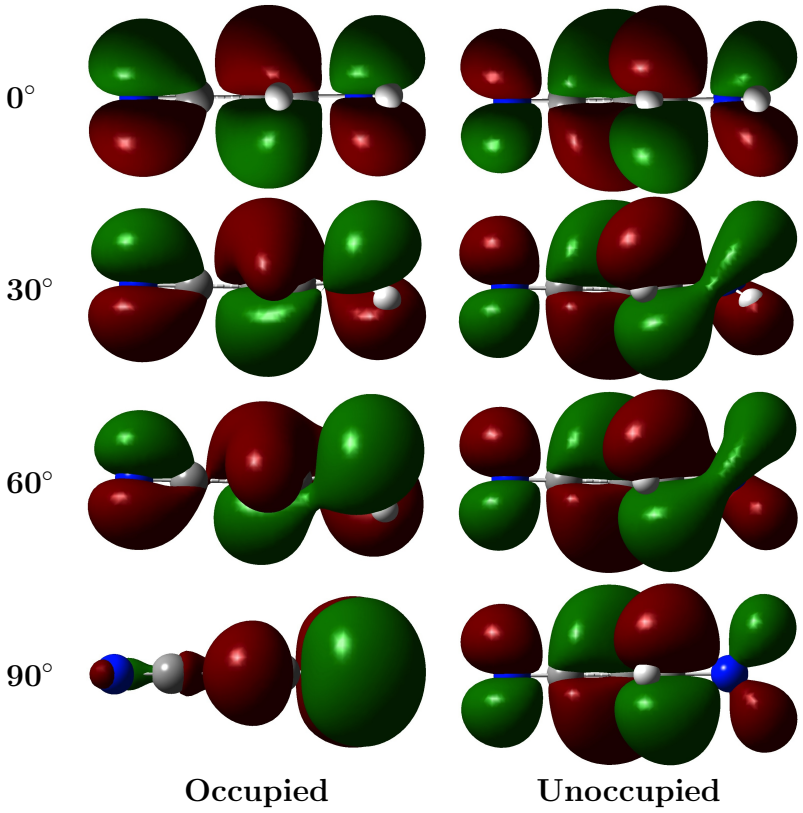

Figure 7.9: The evolution of the PBE ground state occupied and unoccupied orbitals involved in the dominant transition of the first triplet excited state, with increasing twist angle τ.

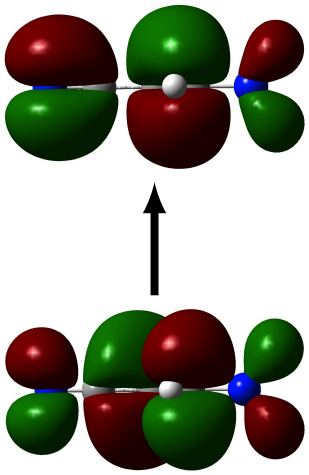

Figure 7.10: The dominant orbital transition involved in the second triplet excited state at 90° using PBE.

as the diabatic state denoted by red followed by green in figure 7.8. As expected, the value of Λ for this state never rises above 0.4. Again, this is reflected in the significant underestimation of the energy of this state.

At $\tau = 90°$ the 2nd state is unlike any of the states seen in the singlet cases. At this angle, it is a local excitation. During the twist from 0° to 90° this state drops significantly in energy from the 7th to 2nd state; intersecting all states in between. During this drop in energy, it maintains a Λ value well above the threshold value and therefore, the significant drop in energy cannot be attributed to a breakdown in TDDFT performance.

In the region close to $\tau = 90°$, the 1st and 2nd states begin to approach each other in energy and their characters increasingly mix. However, at 90°, the two states adopt different symmetries. Therefore, as the twist angle approaches this value, they must begin to adopt the character they will possess at that angle. The result is a reduction in mixing and a separation of character. This can be seen as an "aborted avoided-crossing" and is reflected in the rapid divergence of the relevant Λ values (red and blue curves in figure 7.8(b)) in the region of $\tau > 85°$. The orbital transition involved in the second excitation at $\tau = 90°$ is shown in figure 7.10. It is this transition that is involved in the mixing with the lowest state immediately before $\tau = 90°$.

CAM-B3LYP TDDFT Triplets

Figure 7.11 presents plots of the TDDFT energy and Λ value for the lowest three triplet excited states of $C_3N_2H_4$ as determined using CAM-B3LYP. Despite the prediction of a TDDFT failure for the lowest excited state with PBE, the lowest state given by CAM-B3LYP bears a striking similarity in both form and energy to that of PBE. This is unexpected as, usually, the presence of a charge-transfer state should result in CAM-B3LYP producing the state at a significantly higher energy than PBE. It is the case here that the TDDFT failure arising when using GGA functionals in cases with low occupied-unoccupied orbital overlap does not manifest itself as an error in the energy, but rather as an error in the *character* of the excited state.

Despite the similarity in behaviour and energy between PBE and CAM-B3LYP, there is a marked difference in the nature of the lowest triplet excited state at angles approaching 90°. Whereas with PBE, the lowest state is dominated throughout by the

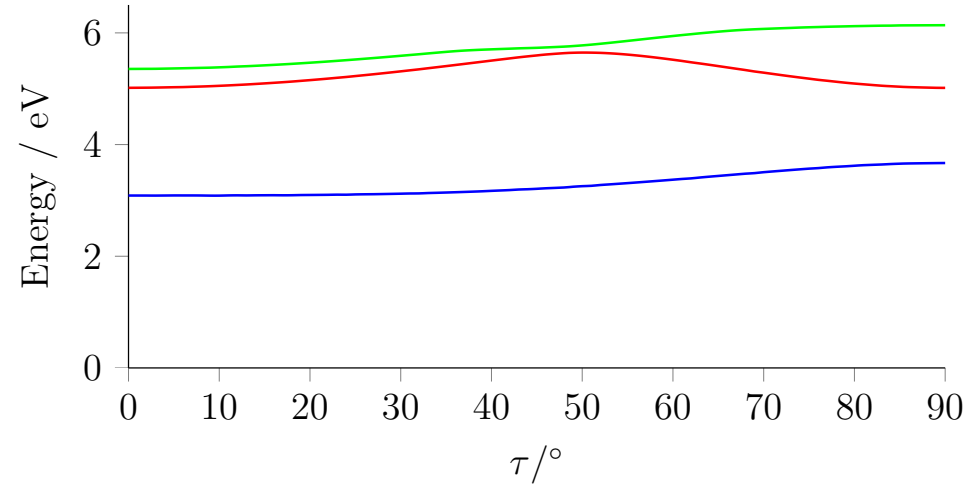

(a)

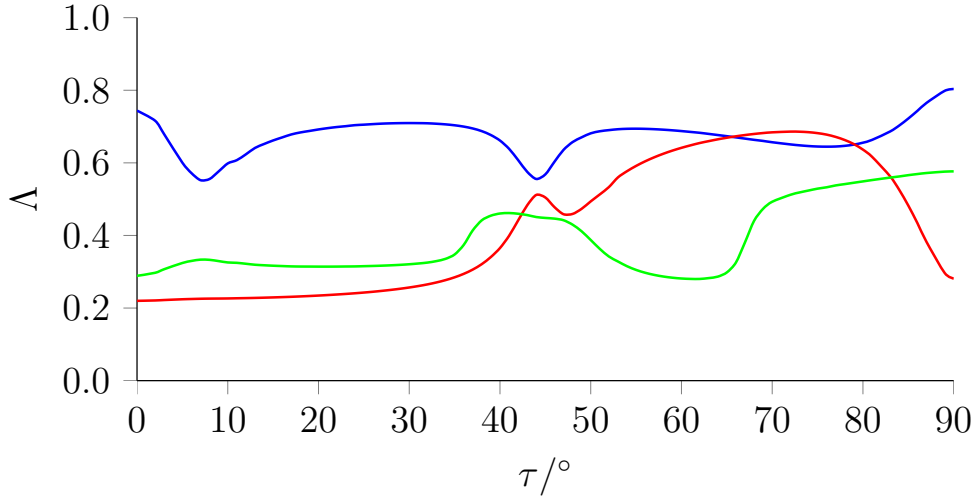

(b)

Figure 7.11: Plots of the TDDFT (a) Energy and (b) Λ value as a function of the twist angle τ for the lowest three triplet excited states of $C_3N_2H_4$ calculated using CAM-B3LYP. 1^3A blue, 2^3A red and 3^3A green.

LE→CT transition (evident from the rapid decrease in Λ seen in figure 7.8(b)), CAM-B3LYP gives an avoided crossing between the lowest two states at $\tau \sim 75°$. This avoided crossing is not as clear as others seen previously but occurs over a wide range of angles and only involves mixing to a small degree.

The appearance of this avoided crossing in CAM-B3LYP but not in PBE can be understood in terms of the charge-transfer underestimation by PBE. As CAM-B3LYP pushes the energy of this state up (correcting the PBE underestimation), the "aborted avoided-crossing" observed when using PBE is now replaced with an actual avoided crossing, at an angle well before 90°. As a result, CAM-B3LYP produces the correct

state ordering at 90°. The evolution of the orbitals involved in the dominant transitions of the lowest triplet excited state when using CAM-B3LYP are plotted in figure 7.12 for angles of $\tau > 60°$. Below this angle, the orbitals match those seen when using PBE (figure 7.9). At $\tau = 75°$ there are two dominant transitions as this is in the region of the avoided crossing. At $\tau = 90°$, the occupied orbital involved in the transition is different from that seen when using PBE (figure 7.9), giving instead, the correct local character. This is the same as the orbital transition involved in the second state at $\tau = 90°$ when using PBE (figure 7.10). A schematic depiction of the different treatment of the lowest two states by PBE and CAM-B3LYP at 90° is shown in figure 7.13, which also plots the dominant orbital transitions of the lowest two excited states at 90°. It shows how the increase in energy of the charge-transfer state with CAM-B3LYP gives rise to an avoided crossing, the result of which is a lowest energy surface matching PBE in energy, but not in character.

The key difference when comparing with the reference CCSD data is therefore in the *character*. As can be seen in table 7.2, the energy of the lowest triplet state at 90° when using PBE, CAM-B3LYP and CCSD are all fairly similar. However, PBE gives an incorrect ordering of states. Caution is therefore advised in circumstances where it appears that GGA functionals have successfully predicted TDDFT excitation energies despite low orbital overlaps (Λ values) as the error may be manifesting as an error in character rather than energy. It can also be seen that CAM-B3LYP provides a better qualitative description of the lowest three triplet excited states when compared to the reference CCSD data shown in figure 7.14.

7.2.2 ΔSCF Triplets

Time-*independent* DFT, as used throughout this thesis, is applicable to the lowest state of any space-spin symmetry. Usually, this involves the determination of the ground singlet state. However, it is equally applicable to the determination of the lowest triplet state regardless of whether or not it is the ground state. It is therefore possible to determine the lowest triplet excitation energy for a system with singlet ground state

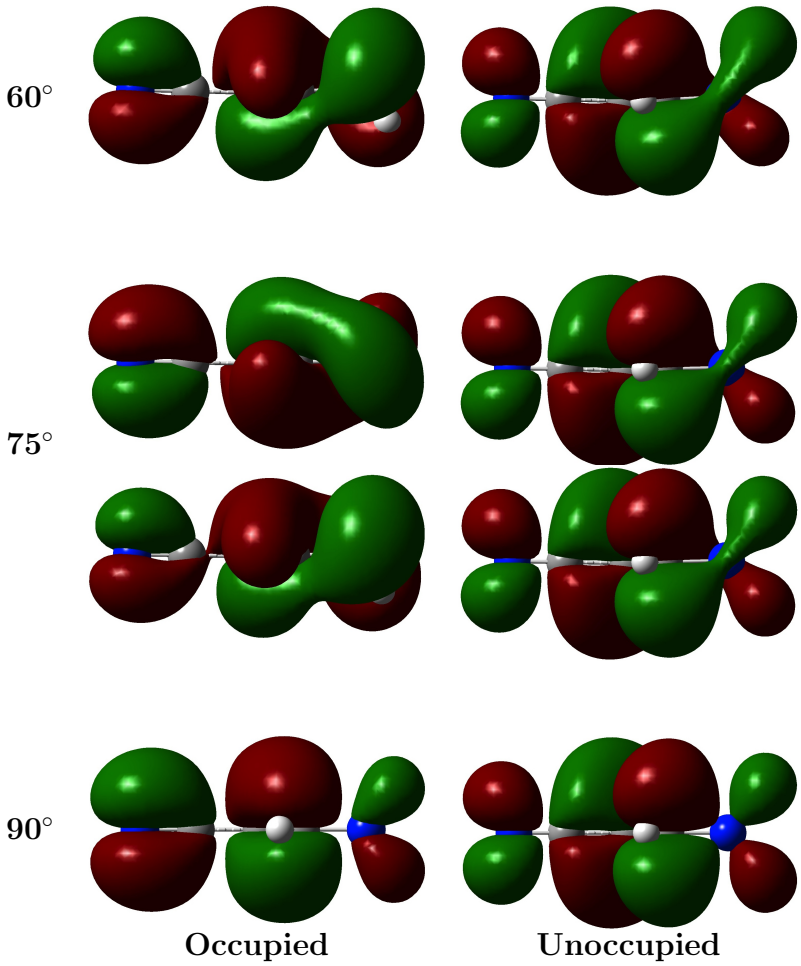

Figure 7.12: The evolution of the CAM-B3LYP ground state occupied and unoccupied orbitals involved in the dominant transition of the first excited state from $\tau = 60°$ onwards. Note that for 75° there are two dominant transitions.

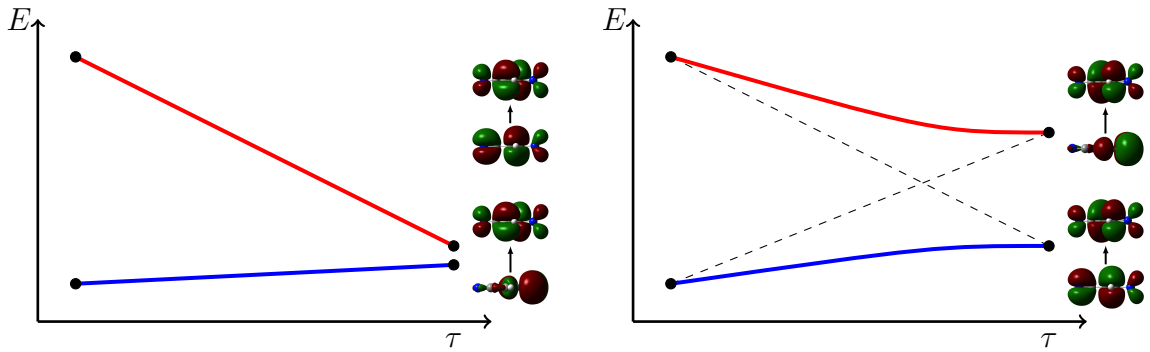

Figure 7.13: Schematic diagrams illustrating how, at 90°, the correction of the underestimated charge-transfer state when using (a) PBE gives rise to an avoided crossing when using (b) CAM-B3LYP. The dashed lines represent diabatic states while the solid lines correspond to the actual surfaces.

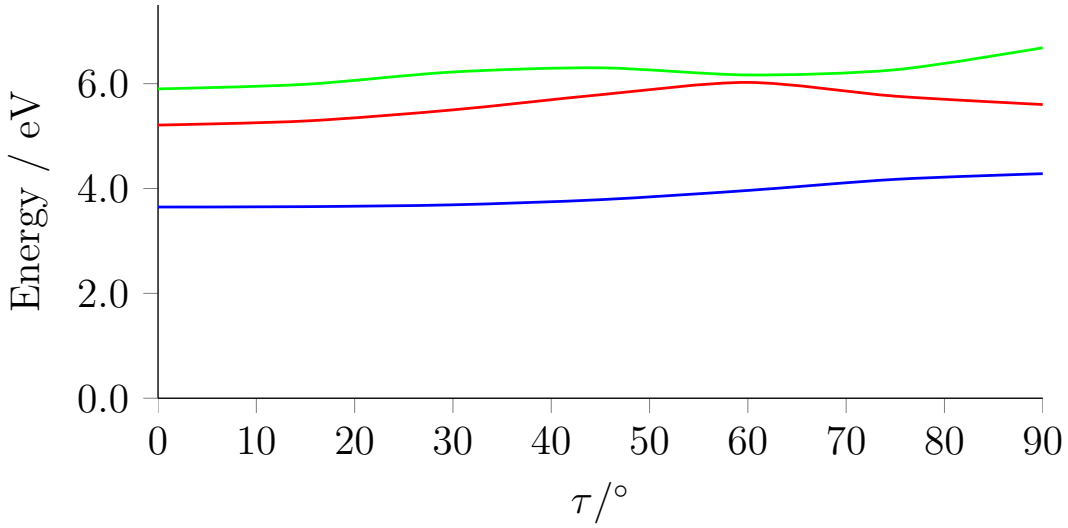

Figure 7.14: Plot of the Energy as a function of the twist angle τ for the lowest three triplet excited states of $C_3N_2H_4$ calculated using CCSD. 1^3A blue, 2^3A red and 3^3A green.

simply as a difference,

$$E_{\Delta\text{SCF}} = E_{\text{triplet}} - E_{\text{singlet}} \tag{7.1}$$

from time-independent calculations on the two states. This approach is known as ΔSCF. The final part of this chapter makes an explicit comparison between the TDDFT and ΔSCF approaches, with an emphasis on excitation character.

PBE ΔSCF Triplets

For PBE, the energy using the ΔSCF approach has an almost identical appearance to that determined through TDDFT, although slightly higher in energy as can be seen from figure 7.15, thereby closer to the CCSD data. At $\tau = 0°$, the character of the transition is identical with both TDDFT and ΔSCF. However, at $\tau = 90°$, the ΔSCF approach correctly gives the locally excited state as the lowest, as opposed to the charge-transfer state which was incorrectly predicted to be the lowest when using TDDFT. It is the case then, that *the charge-transfer breakdown in TDDFT does not arise when using* ΔSCF, in this case.

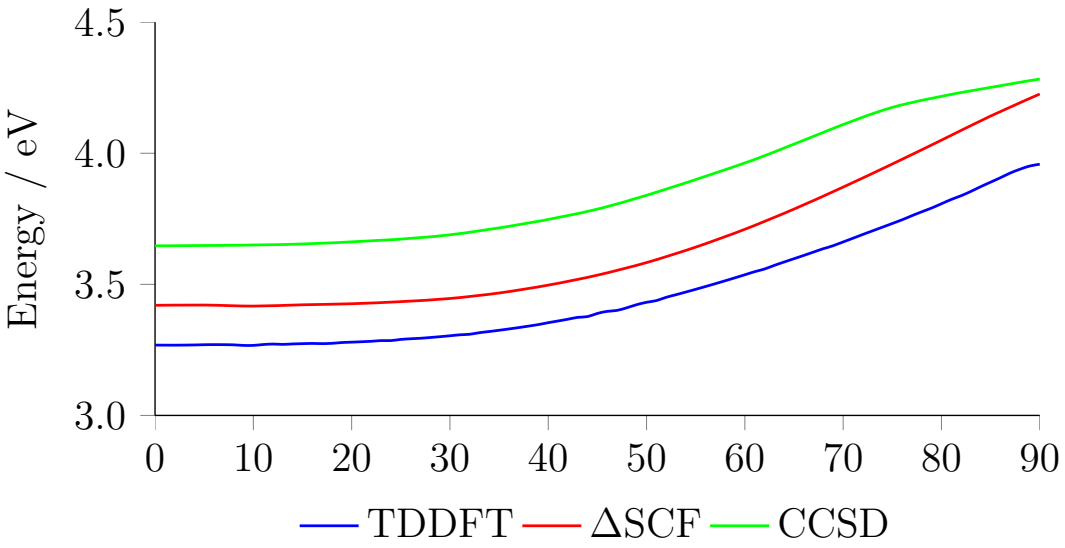

Figure 7.15: Plot of the Energy as a function of the twist angle τ for the lowest triplet excited state of $C_3N_2H_4$, determined using TDDFT and ΔSCF with PBE. Reference CCSD data also shown.

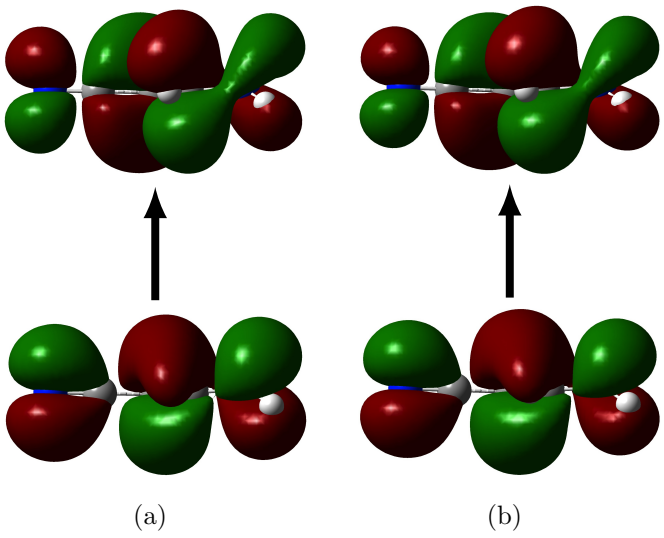

Figure 7.16: The similarity in the PBE orbital transitions at $\tau = 30°$ for the (a) ground state HOMO→LUMO and (b) triplet state βLUMO→αHOMO, corresponding to the TDDFT and ΔSCF descriptions, respectively.

In order to reconcile the multiple occupied–unoccupied orbital transitions that contribute to the character of TDDFT excitations with the single transition picture arising from the ΔSCF approach, we can combine the ground state orbitals involved in the dominant TDDFT transitions and compare those with the relevant excited state orbitals from ΔSCF. In doing so, we assume that the transition involved in the ΔSCF approach has taken place from the lowest unoccupied β spin orbital to the highest occupied α spin orbital, of an explicit calculation on the triplet state. For twist angles of $\tau < 45°$, the lowest PBE TDDFT excitation is dominated by one transition only: HOMO→LUMO, which exactly matches the lowest unoccupied β and highest occupied α orbitals from the ΔSCF approach. The orbital transitions for a representative example ($\tau = 30°$) are shown in figure 7.16, where the similarity in the orbital transitions from the two approaches can be seen.

At larger twist angles, the lowest two states, HOMO→LUMO and HOMO−1→LUMO, begin to mix in TDDFT. Figure 7.17 shows how (at $\tau = 60°$) a combination of the ground state HOMO and HOMO−1 orbitals according to their respective κ values produces an orbital transition which matches that obtained when using ΔSCF. Although it is not possible to perform the ΔSCF procedure for any triplet state but the lowest, it can be inferred from the agreement with the character of the lowest state given by CCSD that the method correctly introduces an avoided crossing between the lowest two states.

CAM-B3LYP ΔSCF Triplets

The character of the lowest excitation produced by the ΔSCF approach matches that from TDDFT for all twist angles. The energy of the state is slightly higher when determined with ΔSCF, as can be seen in figure 7.18 and so is again close to CCSD. The same observations seen for PBE can be made concerning the combination of ground state orbitals according to their TDDFT κ values producing orbitals agreeing with those from triplet calculations. This is seen for any circumstances under which there is significant mixing of orbitals, which occurs for both orbital re-ordering and avoided crossings of excited states. Therefore, as far as CAM-B3LYP is concerned, it can be concluded that irrespective of approach (TDDFT or ΔSCF) the correct character can be obtained.

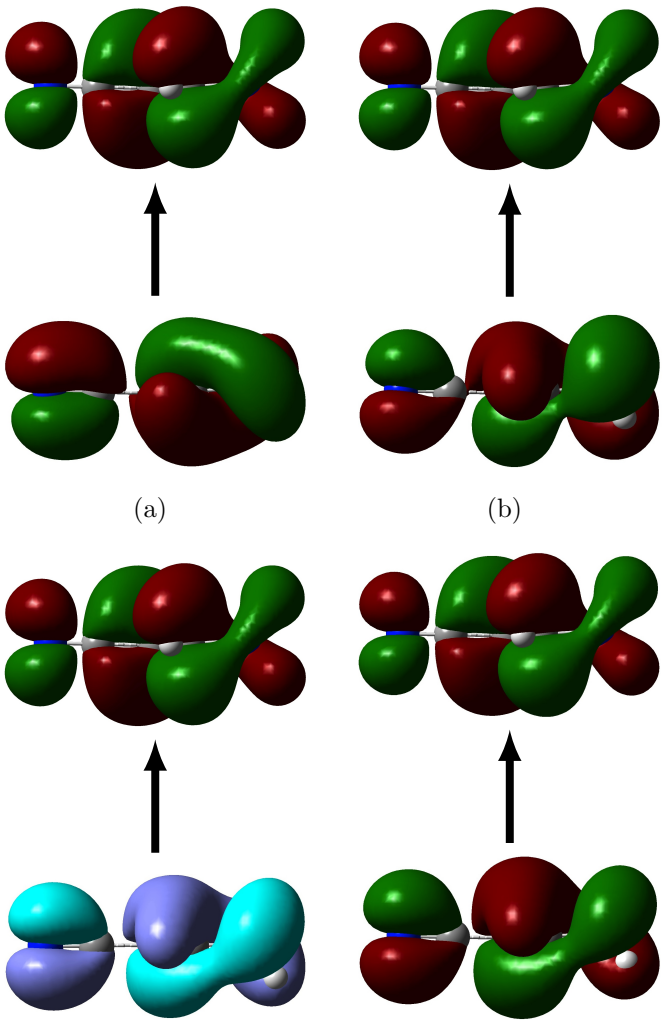

Figure 7.17: The combination of PBE ground state (a) HOMO−1→LUMO and (b) HOMO→LUMO according to their respective κ values is shown in (c). This bears a striking similarity to the triplet state (d) βLUMO→αHOMO.

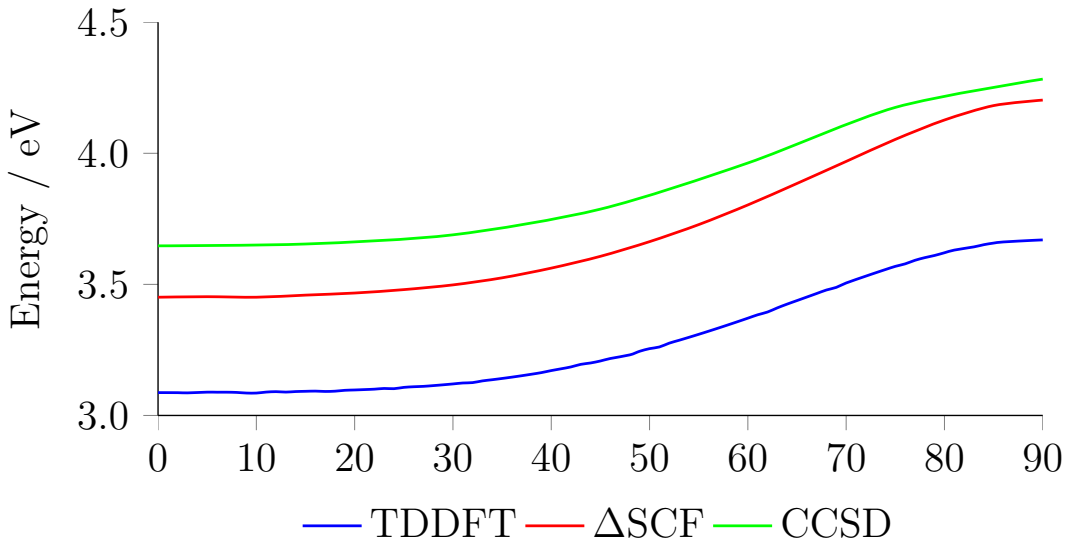

Figure 7.18: Plot of the energy as a function of the twist angle τ for the lowest triplet excited state of $C_3N_2H_4$, determined using TDDFT and ΔSCF with CAM-B3LYP. Reference CCSD data also shown.

Summary

There are two general features that arise when considering TDDFT singlet and triplet excited states upon twisting of $C_3N_2H_4$. Firstly, as there is no symmetry during the twist, there are several avoided crossings between the excited states. These are observable in the plots of energy, Λ and oscillator strength as a function of angle. In all three cases, these avoided crossings give rise to features which involve the switching of the two states involved. It is possible to trace a diabatic state which jumps from one surface to the other. An example of this is shown in figure 7.19(a) which shows variation in Λ. Secondly, it is also possible for the ordering of the orbitals to change during the twist. For example, the orbitals which are HOMO and HOMO−1 at 40° could then be HOMO−1 and HOMO at 50°, respectively. This behaviour is not observable in the plots of energy or oscillator strength as a function of angle. However, it does cause a feature in the equivalent Λ plot, an example of which is shown in figure 7.19(b). It is important to be able to distinguish between these two cases when considering the Λ plots and it also illustrates that there is additional information about the character of the states contained within Λ that is not present in the energy or oscillator strength.

Another feature that arises is the evolution of a local state at $\tau = 0°$ involving orbitals that are both extended over the whole molecule into a charge-transfer state at

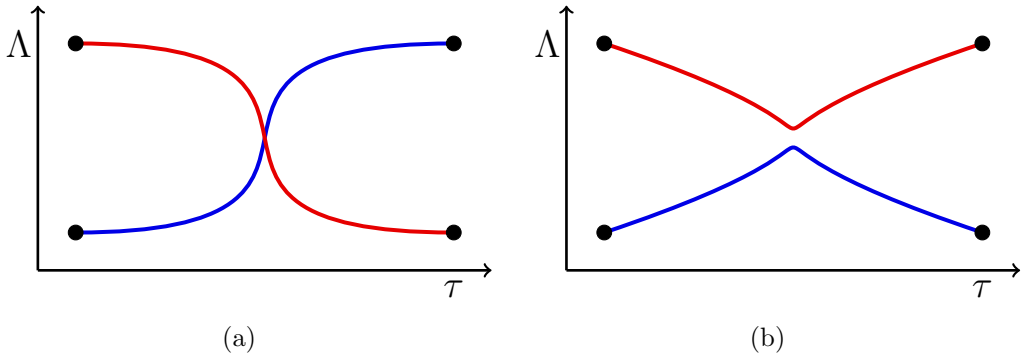

Figure 7.19: Schematic diagrams of the two principal features observed in the plots of Λ vs. τ. They correspond to (a) an avoided crossing and (b) a re-ordering of orbitals.

$\tau = 90°$, where the occupied orbital is localised on the amine. The presence of this state causes inaccuracies in the topography of the TDDFT PBE surface as the corresponding Λ value drops below the threshold value of ~ 0.4. In the case of singlet excited states, the incorrect description of this state by TDDFT results in too low an *energy* whereas in the case of triplet excited states, the result is incorrect *character*. Despite the charge-transfer error, the character of the state is correct in the former case and the energy is correct in the latter case. CAM-B3LYP is able to resolve both of these issues. Finally, it has also been shown that the ΔSCF approach to determining triplet excited states can overcome the charge-transfer error observed in the use of PBE with TDDFT and that the character of excitation from TDDFT (multiple contributions) and ΔSCF (single contribution) can be reconciled.

Chapter 8

Conclusion

Research into the development and application of modern DFT covers a wide range of topics. In this thesis, two areas of active interest have been considered. Firstly, the application of DFT to weak interactions was used to illustrate the issues of fractional spins and fractional charges as well as intermolecular interactions governed by the dispersion force. Secondly, the determination of excited states through TDDFT that is of critical importance in the comparison with, and understanding of, experimental observations. For both of these topics, the application of a Coulomb-attenuated exchange-correlation functional (CAM-B3LYP) has demonstrated that recent developments in DFT are yielding results of a higher accuracy than the functionals currently in widespread use.

In chapter 3, the three key problems of dispersion, fractional spins and fractional charges were illustrated through the model systems, H_2 and H_2^+. The effect of these issues was understood by considering them in terms of the force and the Feynman distortion of electron densities. It was found that the increasing proportions of exact exchange in Coulomb attenuated functionals can exaggerate the fractional spin error compared to resolving the fractional charge error.

This was followed by a closer look at the weak intermolecular force, dispersion, in chapter 4, where the ability of DFT functionals to accurately reproduce C_6 dispersion coefficients was assessed. CAM-B3LYP showed a notable improvement over conventional GGA and hybrid functionals. C_6 coefficients were then employed through the popular DFT-D method which provides an empirical dispersion correction for DFT calculations. Dispersion corrected potential energy surfaces of the rare-gas diatomics and dispersion corrected interaction energies of biologically relevant complexes were subsequently de-

termined. Although CAM-B3LYP provided no significant improvement in performance over other currently available DFT-D functionals, its performance was of a comparable accuracy. The role of the attenuation parameters in CAM-B3LYP was assessed in both the study relating to the determination of C_6 coefficients and that concerning the application of DFT-D.

The remaining three chapters were concerned with the determination of excited states through the TDDFT approach. In chapter 5 an extensive comparison was made between theoretically determined excitation energies and experimentally observed absorption spectra for pyrene and several of its derivatives. Although B3LYP can show promising results, this is in fact a fortuitous cancellation of errors. A more rigorous comparison, accounting for the vibrational structure of the states involved in the transition shows that B3LYP results are not satisfactory. CAM-B3LYP, however, provides an excellent description of the excited states. Also discussed in this chapter was the formation of organic excimers and the need for exchange-correlation functionals to contain sufficient quantities of exact exchange. This is necessary to avoid the underestimation of charge-transfer states that can disrupt other states of a similar energy and therefore preclude a correct description of excimer formation.

Chapter 6 considered several properties of the retinal chromophore, whose description with conventional functionals has been flawed. Through the application of CAM-B3LYP it was shown that improved descriptions of proton transfer reactions and the effects of a protein's environment are possible. This was followed by a detailed examination of how simple physical and chemical processes can cause charge-transfer excitations to arise. This poses a significant problem for conventional functionals whose poor performance for such excitations is well established. Through the application of CAM-B3LYP, significant errors in both character—identified through an analysis of oscillator strengths—and energy for charge-transfer excitations were largely removed. It was also shown how a diagnostic test based on orbital overlap can not only provide insight into such problems, but also could have predicted that they would arise before any comparison with reference data was required. The results of this study show that CAM-B3LYP has the potential to provide a qualitatively correct description with accuracy approaching that offered by coupled-cluster methods.

Finally, the issues with character and energy previously observed in charge-transfer

excitations, was further analysed. Through the use of a model compound it was shown how the charge-transfer error with conventional functionals can misleadingly arise in character only—giving seemingly accurate energies. CAM-B3LYP accurately determines both the character and the energy of the relevant excitations. The determination of triplet excited states was considered both through TDDFT and the less commonplace ΔSCF approach. It was shown that the charge-transfer error experienced when using TDDFT is largely eliminated when ΔSCF is employed. Additionally, CAM-B3LYP was shown to have a significantly superior performance than the GGA functional PBE.

The past few years have seen a surge of interest in long-range corrected functionals within the DFT community. By incorporating varying amounts of exact exchange into functionals, significantly improved performance can be realised. This thesis has shown how such functionals, with specific emphasis on CAM-B3LYP, can go some way to solving some of the traditional problems experienced in the application of DFT.

Bibliography

[1] E. Schrödinger, *Ann. Phys.*, 1926, **79**, 361–376.

[2] M. Born and J. R. Oppenheimer, *Ann. Phys.*, 1927, **84**, 457–484.

[3] D. R. Hartree, *Proc. Camb. Phil. Soc.*, 1928, **24**, 89–110.

[4] D. R. Hartree, *Proc. Camb. Phil. Soc.*, 1928, **24**, 111–132.

[5] D. R. Hartree, *Proc. Camb. Phil. Soc.*, 1928, **24**, 426–37.

[6] V. Fock, *Z. Phys.*, 1930, **61**, 126–148.

[7] V. Fock, *Z. Phys.*, 1930, **62**, 795–805.

[8] J. C. Slater, *Phys. Rev.*, 1929, **34**, 1293–1322.

[9] J. C. Slater, *Phys. Rev.*, 1930, **35**, 509–529.

[10] W. Pauli, *Z. Phys.*, 1927, **43**, 601–623.

[11] C. C. J. Roothaan, *Rev. Mod. Phys.*, 1951, **23**, 69–89.

[12] G. G. Hall, *Proc. Roy. Soc.*, 1951, **A205**, 541–552.

[13] J. A. Pople and R. K. Nesbet, *J. Chem. Phys.*, 1954, **22**, 571–572.

[14] J. Čížek, *J. Chem. Phys.*, 1966, **45**, 4256–4266.

[15] J. Čížek and J. Paldus, *Int. J. Quantum Chem.*, 1971, **5**, 359–379.

[16] J. Čížek, *Theor. Chim. Acta.*, 1991, **80**, 91–94.

[17] K. Raghavachari, G. W. Trucks, J. A. Pople and M. Head-Gordon, *Chem. Phys. Lett.*, 1989, **157**, 479–483.

[18] O. Christiansen, H. Koch and P. Jørgensen, *Chem. Phys. Lett.*, 1995, **243**, 409–418.

[19] O. Christiansen, *Theor. Chem. Acc.*, 2006, **116**, 106–123.

[20] S. F. Boys, *Proc. Roy. Soc.*, 1950, **A200**, 542–554.

[21] E. Bright-Wilson, *Structural Chemistry and Biology*, W.H. Freeman, San Francisco, 1968.

[22] L. H. Thomas, *Proc. Camb. Phil. Soc.*, 1927, **23**, 542–548.

[23] E. Fermi, *Z. Phys.*, 1928, **48**, 73–79.

[24] P. A. M. Dirac, *Proc. Cam. Phil. Soc.*, 1930, **26**, 376–385.

[25] R. G. Parr and W. Yang, *Density-Functional Theory of Atoms and Molecules*, Oxford University Press, 1989.

[26] P. Hohenberg and W. Kohn, *Phys. Rev.*, 1964, **136**, B864–B871.

[27] E. H. Lieb, *Int. J. Quantum Chem.*, 1983, **24**, 243–277.

[28] M. Levy, *Phys. Rev. A*, 1982, **26**, 1200–1208.

[29] M. Levy, *Proc. Natl. Acad. Sci. USA*, 1979, **76**, 6062–6065.

[30] W. Kohn and L. J. Sham, *Phys. Rev.*, 1965, **140**, A1133–A1138.

[31] D. M. Ceperley and B. J. Alder, *Phys. Rev. Lett.*, 1980, **45**, 566–569.

[32] S. H. Vosko, L. Wilk and M. Nusair, *Can. J. Phys.*, 1980, **58**, 1200–1211.

[33] J. P. Perdew, K. Burke and M. Ernzerhof, *Phys. Rev. Lett.*, 1996, **77**, 3865–3868.

[34] J. P. Perdew and Y. Wang, *Phys. Rev. B*, 1992, **45**, 13244–13249.

[35] J. P. Perdew and W. Yue, *Phys. Rev. B*, 1986, **33**, 8800–8802.

[36] A. D. Becke, *Phys. Rev. A*, 1988, **38**, 3098–3100.

[37] C. Lee, W. Yang and R. G. Parr, *Phys. Rev. B*, 1988, **37**, 785–789.

[38] D. C. Langreth and J. P. Perdew, *Solid State Commun.*, 1975, **17**, 1425–1429.

[39] O. Gunnarsson and B. I. Lundqvist, *Phys. Rev. B*, 1976, **13**, 4274–4298.

[40] D. C. Langreth and J. P. Perdew, *Phys. Rev. B*, 1977, **15**, 2884–2901.

[41] J. Harris and R. O. Jones, *J. Phys. F. Met. Phys.*, 1974, **4**, 1170–1186.

[42] J. Harris, *Phys. Rev. A*, 1984, **29**, 1648–1659.

[43] H. Hellmann, in *Einführung in die Quantenchemie*, Leipzig: Franz Deuticke, 1937, p. 285.

[44] R. P. Feynman, *Phys. Rev.*, 1939, **56**, 340–343.

[45] A. D. Becke, *J. Chem. Phys.*, 1993, **98**, 1372–1377.

[46] A. D. Becke, *J. Chem. Phys.*, 1993, **98**, 5648–5652.

[47] P. J. Stephens, F. J. Devlin, C. F. Chabalowski and M. J. Frisch, *J. Phys. Chem.*, 1994, **98**, 11623–11627.

[48] M. Ernzerhof and G. E. Scuseria, *J. Chem. Phys.*, 1999, **110**, 5029–5036.

[49] C. Adamo and V. Barone, *J. Chem. Phys.*, 1999, **110**, 6158–6170.

[50] A. D. Becke, *J. Chem. Phys.*, 1997, **107**, 8554–8560.

[51] F. A. Hamprecht, A. J. Cohen, D. J. Tozer and N. C. Handy, *J. Chem. Phys.*, 1998, **109**, 6264–6271.

[52] T. Yanai, D. P. Tew and N. C. Handy, *Chem. Phys. Lett.*, 2004, **393**, 51–57.

[53] T. Leininger, H. Stoll, H.-J. Werner and A. Savin, *Chem. Phys. Lett.*, 1997, **275**, 151–160.

[54] R. D. Adamson, J. P. Dombroski and P. M. W. Gill, *J. Comput. Chem.*, 1999, **20**, 921–927.

[55] P. M. W. Gill, R. D. Adamson and J. A. Pople, *Mol. Phys.*, 1996, **88**, 1005–1010.

[56] A. Savin, in *Recent Developments and Applications of Modern Density Functional Theory*, ed. J. M. Seminario, Elsevier, Amsterdam, 1996, pp. 327–357.

[57] H. Iikura, T. Tsuneda, T. Yanai and K. Hirao, *J. Chem. Phys.*, 2001, **115**, 3540–3544.

[58] Y. Tawada, T. Tsuneda, S. Yanagisawa, T. Yanai and K. Hirao, *J. Chem. Phys.*, 2004, **120**, 8425–8433.

[59] M. Kamiya, T. Tsuneda and K. Hirao, *J. Chem. Phys.*, 2002, **117**, 6010–6015.

[60] E. Runge and E. K. U. Gross, *Phys. Rev. Lett.*, 1984, **52**, 997–1000.

[61] M. E. Casida, in *Recent Advances in Density Functional Methods, Part I*, ed. D. P. Chong, Singapore, World Scientific, 1995, pp. 155–192.

[62] A. Dreuw and M. Head-Gordon, *Chem. Rev.*, 2005, **105**, 4009–4037.

[63] E. K. U. Gross, C. A. Ullrich and U. J. Gossmann, in *Density Functional Theory*, ed. E. K. U. Gross and R. M. Dreizler, Plenum, New York, 1994, pp. 149–171.

[64] M. A. L. Marques and E. K. U. Gross, *Annu. Rev. Phys. Chem.*, 2004, **55**, 427–455.

[65] M. A. L. Marques and E. K. U. Gross, *A Primer in Density Functional Theory*, 2003, 144–184.

[66] J. P. Perdew, R. G. Parr, M. Levy and J. L. Balduz, *Phys. Rev. Lett.*, 1982, **49**, 1691–1694.

[67] J. P. Perdew and M. Levy, *Phys. Rev. Lett.*, 1983, **51**, 1884–1887.

[68] A. M. Teale, F. De Proft and D. J. Tozer, *J. Chem. Phys.*, 2008, **129**, 044110.

[69] J. P. Perdew and K. Burke, *Int. J. Quantum Chem.*, 1996, **57**, 309–319.

[70] D. J. Tozer and N. C. Handy, *J. Chem. Phys.*, 1998, **108**, 2545–2555.

[71] D. J. Tozer and N. C. Handy, *J. Chem. Phys.*, 1998, **109**, 10180–10189.

[72] A. Dreuw, G. R. Fleming and M. Head-Gordon, *Phys. Chem. Chem. Phys.*, 2003, **5**, 3247–3256.

[73] A. Dreuw and M. Head-Gordon, *J. Am. Chem. Soc.*, 2004, **126**, 4007–4016.

[74] S. Anand and H. B. Schlegel, *Mol. Phys.*, 2006, **104**, 933–941.

[75] E. A. Perpète, J. Preat, J.-M. Andre and D. Jacquemin, *J. Phys. Chem. A*, 2006, **110**, 5629–5635.

[76] X. Xu, Z. Cao and Q. Zhang, *J. Phys. Chem. A*, 2006, **110**, 1740–1748.

[77] A. Dreuw, J. L. Weisman and M. Head-Gordon, *J. Chem. Phys.*, 2003, **119**, 2943–2946.

[78] D. J. Tozer, *J. Chem. Phys.*, 2003, **119**, 12697–12699.

[79] O. Gritsenko and E. J. Baerends, *J. Chem. Phys.*, 2004, **121**, 655–660.

[80] R. Kobayashi and R. D. Amos, *Chem. Phys. Lett.*, 2006, **420**, 106–109.

[81] P. N. Day, K. A. Nguyen and R. Pachter, *J. Chem. Phys.*, 2006, **125**, 094103.

[82] D. Jacquemin, E. A. Perpète, O. A. Vydrov, G. E. Scuseria and C. Adamo, *J. Chem. Phys.*, 2007, **127**, 094102.

[83] K. A. Nguyen, P. N. Day and R. Pachter, *J. Chem. Phys.*, 2007, **126**, 094303.

[84] M. J. G. Peach, P. Benfield, T. Helgaker and D. J. Tozer, *J. Chem. Phys.*, 2008, **128**, 044118.

[85] M. J. G. Peach, C. R. L. Sueur, K. Ruud, M. Guillaume and D. J. Tozer, *Phys. Chem. Chem. Phys.*, 2009, **11**, 4465–4470.

[86] A. J. Cohen, P. Mori-Sanchez and W. T. Yang, *Science*, 2008, **321**, 792–794.

[87] A. J. Cohen, P. Mori-Sánchez and W. Yang, *J. Chem. Theory Comput.*, 2009, **5**, 786–792.

[88] A. J. Cohen, P. Mori-Sánchez and W. Yang, *J. Chem. Phys.*, 2008, **129**, 121104.

[89] P. Mori-Sánchez, A. J. Cohen and W. Yang, *Phys. Rev. Lett.*, 2008, **100**, 146401.

[90] A. J. Cohen, P. Mori-Sanchez and W. T. Yang, *Phys. Rev. B*, 2008, **77**, 115123.

[91] P. Mori-Sánchez, A. J. Cohen and W. Yang, *Phys. Rev. Lett.*, 2009, **102**, 066403.

[92] M. J. Allen and D. J. Tozer, *J. Chem. Phys.*, 2002, **117**, 11113–11120.

[93] C. E. Dykstra, *Chem. Phys. Lett.*, 1977, **45**, 466–469.

[94] N. C. Handy, J. A. Pople, M. Head-Gordon, K. Raghavachari and G. W. Trucks, *Chem. Phys. Lett.*, 1989, **164**, 185–192.

[95] R. Kobayashi, N. C. Handy, R. D. Amos, G. W. Trucks, M. J. Frisch and J. A. Pople, *J. Chem. Phys.*, 1991, **95**, 6723–6733.

[96] T. Korona, H. L. Williams, R. Bukowski, B. Jeziorski and K. Szalewicz, *J. Chem. Phys.*, 1997, **106**, 5109–5122.

[97] R. D. Amos, I. L. Alberts, J. S. Andrews, A. J. Cohen, S. M. Colwell, N. C. Handy, D. Jayatilaka, P. J. Knowles, R. Kobayashi, G. J. Laming, A. M. Lee, P. E. Maslen, C. W. Murray, P. Palmieri, J. E. Rice, E. D. Simandiras, A. J. Stone, M.-D. Su and D. J. Tozer, CADPAC 6.5*, The Cambridge Analytic Derivatives Package*, 1998, Cambridge, England.

[98] DALTON*, a molecular electronic structure program, Release 2.0*, 2005, see http://www.kjemi.uio.no/software/dalton/dalton.html.

[99] J. Mitroy and M. W. J. Bromley, *Phys. Rev. A*, 2005, **71**, 032709.

[100] H. J.O. and M. A. Eliason, *J. Chem. Phys.*, 1967, **47**, 1164.

[101] A. D. Buckingham, P. W. Fowler and J. M. Hutson, *Chem. Rev.*, 1988, **88**, 963–988.

[102] P. Jurecka, J. Cerny, P. Hobza and D. R. Salahub, *J. Comput. Chem.*, 2007, **28**, 555–569.

[103] S. Grimme, J. Antony, T. Schwabe and C. Muck-Lichtenfeld, *Org. Biomol. Chem.*, 2007, **5**, 741–758.

[104] C. M. Dobson, *Nature*, 2003, **426**, 884–890.

[105] E. Querol, J. A. PerezPons and A. MozoVillarias, *Protein Eng.*, 1996, **9**, 265–271.

[106] R. Aurora and G. D. Rose, *Protein Sci.*, 1998, **7**, 21–38.

[107] J. Vondrasek, L. Bendova, V. Klusak and P. Hobza, *J. Am. Chem. Soc.*, 2005, **127**, 2615–2619.

[108] S. Grimme, *J. Comput. Chem.*, 2006, **27**, 1787–1799.

[109] A. D. Becke and E. R. Johnson, *J. Chem. Phys.*, 2005, **122**, 154104.

[110] A. D. Becke and E. R. Johnson, *J. Chem. Phys.*, 2005, **123**, 154101.

[111] H. B. G. Casimir and D. Polder, *Phys. Rev.*, 1948, **73**, 360–372.

[112] C. Jamorski, M. E. Casida and D. R. Salahub, *J. Chem. Phys.*, 1996, **104**, 5134–5147.

[113] R. D. Amos, N. C. Handy, P. J. Knowles, J. E. Rice and A. J. Stone, *J. Phys. Chem.*, 1985, **89**, 2186–2192.

[114] T. W. Keal and D. J. Tozer, *J. Chem. Phys.*, 2003, **119**, 3015–3024.

[115] T. W. Keal and D. J. Tozer, *J. Chem. Phys.*, 2004, **121**, 5654–5660.

[116] M. Swart, T. van der Wijst, C. F. Guerra and F. M. Bickelhaupt, *J. Mol. Mod.*, 2007, **13**, 1245–1257.

[117] E. R. Johnson and G. A. DiLabio, *Chem. Phys. Lett*, 2006, **419**, 333–339.

[118] A. G. Ioannou, S. M. Colwell and R. D. Amos, *Chem. Phys. Lett.*, 1997, **278**, 278–284.

[119] K. P. Huber and G. Herzberg, *Molecular spectra and molecular structure. 4, Constants of diatomic molecules.*, Van Nostrand, New York, 1979.

[120] G. Graner, C. Rossetti and D. Bailly, *Mol. Phys.*, 1986, **58**, 627–636.

[121] A. R. Hoy, I. M. Mills and G. Strey, *Mol. Phys.*, 1972, **24**, 1265–1290.

[122] E. R. Johnson and A. D. Becke, *J. Chem. Phys.*, 2005, **123**, 024101.

[123] N. C. Handy and D. J. Tozer, *Mol. Phys.*, 1998, **94**, 707–715.

[124] M. J. G. Peach, A. J. Cohen and D. J. Tozer, *Phys. Chem. Chem. Phys.*, 2006, **8**, 4543–4549.

[125] K. Rapcewicz and N. W. Ashcroft, *Phys. Rev. B*, 1991, **44**, 4032–4035.

[126] E. Hult, H. Rydberg, B. I. Lundqvist and D. C. Langreth, *Phys. Rev. B*, 1999, **59**, 4708–4713.

[127] J. F. Dobson and B. P. Dinte, *Phys. Rev. Lett.*, 1996, **76**, 1780–1783.

[128] Y. Andersson, D. C. Langreth and B. I. Lundqvist, *Phys. Rev. Lett.*, 1996, **76**, 102–105.

[129] E. Hult, Y. Andersson, B. I. Lundqvist and D. C. Langreth, *Phys. Rev. Lett.*, 1996, **77**, 2029–2032.

[130] T. Thonhauser, V. R. Cooper, S. Li, A. Puzder, P. Hyldgaard and D. C. Langreth, *Phys. Rev. B*, 2007, **76**, 125112.

[131] R. Ahlrichs, R. Penco and G. Scoles, *Chem. Phys.*, 1977, **19**, 119–130.

[132] H. Y. Liu, M. Elstner, E. Kaxiras, T. Frauenheim, J. Hermans and W. T. Yang, *Proteins: Struct. Func. Gen.*, 2001, **44**, 484–489.

[133] W. T. M. Mooij, F. B. van Duijneveldt, J. G. C. M. van Duijneveldt-van de Rijdt and B. P. van Eijck, *J. Phys. Chem. A*, 1999, **103**, 9872–9882.

[134] M. Elstner, P. Hobza, T. Frauenheim, S. Suhai and E. Kaxiras, *J. Chem. Phys.*, 2001, **114**, 5149–5155.

[135] X. Wu, M. C. Vargas, S. Nayak, V. Lotrich and G. Scoles, *J. Chem. Phys.*, 2001, **115**, 8748–8757.

[136] S. Grimme, *J. Comput. Chem.*, 2004, **25**, 1463–1473.

[137] J. Antony and S. Grimme, *Phys. Chem. Chem. Phys.*, 2006, **8**, 5287–5293.

[138] S. Grimme, C. Diedrich and M. Korth, *Angew. Chem. Int. Ed.*, 2006, **45**, 625–629.

[139] S. Grimme, J. Antony, S. Ehrlich and H. Krieg, *J. Chem. Phys.*, 2010, **132**, 154104.

[140] M. Korth and S. Grimme, *J. Chem. Theory Comput.*, 2009, **5**, 993–1003.

[141] T. Schwabe and S. Grimme, *Acc. Chem. Res.*, 2008, **41**, 569–579.

[142] M. Piacenza and S. Grimme, *ChemPhysChem*, 2005, **6**, 1554–1558.

[143] F. O. Kannemann and A. D. Becke, *J. Chem. Theory Comput.*, 2009, **5**, 719–727.

[144] F. O. Kannemann and A. D. Becke, *J. Chem. Theory Comput.*, 2010, **6**, 1081–1088.

[145] J. Kong, Z. T. Gan, E. Proynov, M. Freindorf and T. R. Furlani, *Phys. Rev. A*, 2009, **79**, 042510.

[146] A. Krishtal, K. Vanommeslaeghe, A. Olasz, T. Veszpremi, C. Van Alsenoy and P. Geerlings, *J. Chem. Phys.*, 2009, **130**, 174101.

[147] E. R. Johnson and A. D. Becke, *J. Chem. Phys.*, 2006, **124**, 174104.

[148] A. D. Becke and E. R. Johnson, *J. Chem. Phys.*, 2006, **124**, 014104.

[149] A. D. Becke and E. R. Johnson, *J. Chem. Phys.*, 2007, **127**, 154108.

[150] T. Sato, T. Tsuneda and K. Hirao, *Mol. Phys.*, 2005, **103**, 1151–1164.

[151] Q. Wu and W. T. Yang, *J. Chem. Phys.*, 2002, **116**, 515–524.

[152] A. Bondi, *J. Phys. Chem.*, 1964, **68**, 441–451.

[153] S. F. Boys and F. Bernardi, *Mol. Phys.*, 1970, **19**, 553.

[154] J. M. Perez-Jorda, J. M. and A. D. Becke, *Chem. Phys. Lett.*, 1995, **233**, 134–137.

[155] S. Kristyan and P. Pulay, *Chem. Phys. Lett.*, 1994, **229**, 175–180.

[156] T. van Mourik and R. J. Gdanitz, *J. Chem. Phys.*, 2002, **116**, 9620–9623.

[157] A. Milet, T. Korona, R. Moszynski and E. Kochanski, *J. Chem. Phys.*, 1999, **111**, 7727–7735.

[158] S. M. Cybulski, T. M. Bledson and R. R. Toczylowski, *J. Chem. Phys.*, 2002, **116**, 11039–11040.

[159] S. M. Cybulski and C. E. Seversen, *J. Chem. Phys.*, 2005, **122**, 014117.

[160] J. M. Perez-Jorda, E. San-Fabian and A. J. Perez-Jimenez, *J. Chem. Phys.*, 1999, **110**, 1916–1920.

[161] K. T. Tang and J. P. Toennies, *J. Chem. Phys*, 1984, **80**, 3726.

[162] K. T. Tang and J. P. Toennies, *J. Chem. Phys.*, 1977, **66**, 1496.

[163] K. T. Tang and J. P. Toennies, *J. Chem. Phys.*, 2003, **118**, 4976.

[164] K. T. Tang, J. M. Norbeck and P. R. Certain, *J. Chem. Phys.*, 1976, **64**, 3063.

[165] J. F. Ogilvie and F. Y. H. Wang, *J. Mol. Struct.*, 1992, **273**, 277.

[166] J. F. Ogilvie and F. Y. H. Wang, *J. Mol. Struct.*, 1993, **291**, 313.

[167] I. C. Gerber and J. G. Ángyán, *J. Chem. Phys.*, 2007, **126**, 044103.

[168] P. Jurecka, J. Sponer, J. Cerny and P. Hobza, *Phys. Chem. Chem. Phys.*, 2006, **8**, 1985–1993.

[169] Y. Zhao and D. G. Truhlar, *J. Chem. Theory Comput.*, 2007, **3**, 289–300.

[170] M. E. Foster and K. Sohlberg, *Phys. Chem. Chem. Phys.*, 2010, **12**, year.

[171] J. P. McNamara and I. H. Hillier, *Phys. Chem. Chem. Phys.*, 2007, **9**, 2362–2370.

[172] T. Sato, T. Tsuneda and K. Hirao, *J. Chem. Phys.*, 2007, **126**, 234114.

[173] J.-D. Chai and M. Head-Gordon, *Phys. Chem. Chem. Phys.*, 2008, **10**, 6615–6620.

[174] W. M. Zhu, J. Toulouse, A. Savin and J. G. Angyan, *J. Chem. Phys.*, 2010, **132**, 244108.

[175] M. Dierksen and S. Grimme, *J. Chem. Phys.*, 2004, **120**, 3544–3554.

[176] J. Franck, *Trans. Faraday Soc.*, 1926, **21**, 0536–0542.

[177] E. Condon, *Phys. Rev.*, 1926, **28**, 1182–1201.

[178] E. U. Condon, *Phys. Rev.*, 1928, **32**, 0858–0872.

[179] G. Herzberg and E. Teller, *Z. Phys. Chem. Abt. B*, 1933, **21**, 410–446.

[180] M. Muccini, *Nature Mater.*, 2006, **5**, 605–613.

[181] P. Sonar, M. S. Soh, Y. H. Cheng, J. T. Henssler and A. Sellinger, *Organic Lett.*, 2010, **12**, 3292–3295.

[182] S. B. Zhao, P. Wucher, Z. M. Hudson, T. M. McCormick, X. Y. Liu, S. N. Wang, X. D. Feng and Z. H. Lu, *Organometallics*, 2008, **27**, 6446–6456.

[183] K. Kalyanasundaram and J. K. Thomas, *J. Am. Chem. Soc.*, 1977, **99**, 2039–2044.

[184] W. M. Vaugham and G. Weber, *Biochemistry*, 1970, **9**, 464.

[185] H. J. Kim, J. H. Bok, J. Vicens, I. H. Suh, J. Ko and J. S. Kim, *Tetrahedron Lett.*, 2005, **46**, 8765–8768.

[186] J. R. Platt, *J. Chem. Phys.*, 1949, **17**, 484–495.

[187] J. R. Platt, *J. Opt. Soc. Am.*, 1953, **43**, 252–257.

[188] S. Grimme and M. Parac, *ChemPhysChem*, 2003, **4**, 292–295.

[189] M. Parac and S. Grimme, *Chem. Phys.*, 2003, **292**, 11 – 21.

[190] M. Dierksen and S. Grimme, *J. Phys. Chem. A*, 2004, **108**, 10225–10237.

[191] M. J. Frisch, G. W. Trucks, H. B. Schlegel, G. E. Scuseria, M. A. Robb, J. R. Cheeseman, J. A. Montgomery, Jr., T. Vreven, K. N. Kudin, J. C. Burant, J. M. Millam, S. S. Iyengar, J. Tomasi, V. Barone, B. Mennucci, M. Cossi, G. Scalmani, N. Rega, G. A. Petersson, H. Nakatsuji, M. Hada, M. Ehara, K. Toyota, R. Fukuda, J. Hasegawa, M. Ishida, T. Nakajima, Y. Honda, O. Kitao, H. Nakai, M. Klene, X. Li, J. E. Knox, H. P. Hratchian, J. B. Cross, V. Bakken, C. Adamo, J. Jaramillo, R. Gomperts, R. E. Stratmann, O. Yazyev, A. J. Austin, R. Cammi, C. Pomelli, J. W. Ochterski, P. Y. Ayala, K. Morokuma, G. A. Voth, P. Salvador, J. J. Dannenberg, V. G. Zakrzewski, S. Dapprich, A. D. Daniels, M. C. Strain, O. Farkas, D. K. Malick, A. D. Rabuck, K. Raghavachari, J. B. Foresman, J. V. Ortiz, Q. Cui, A. G. Baboul, S. Clifford, J. Cioslowski, B. B. Stefanov, G. Liu, A. Liashenko, P. Piskorz, I. Komaromi, R. L. Martin, D. J. Fox, T. Keith, M. A.

Al-Laham, C. Y. Peng, A. Nanayakkara, M. Challacombe, P. M. W. Gill, B. Johnson, W. Chen, M. W. Wong, C. Gonzalez and J. A. Pople, GAUSSIAN 03*, Revision C.02*, Gaussian, Inc., Wallingford, CT, 2004.

[192] B. C. Wang, J. C. Chang, H. C. Tso, H. F. Hsu and C. Y. Cheng, *J. Mol. Struct.: THEOCHEM*, 2003, **629**, 11–20.

[193] I. S. K. Kerkines, I. D. Petsalakis, G. Theodorakopoulos and W. Klopper, *J. Chem. Phys.*, 2009, **131**, 224315.

[194] Y. H. Park and B. S. Cheong, *Curr. App. Phys.*, 2006, **6**, 700–705.

[195] S. W. Yang, A. Elangovan, K. C. Hwang and T. I. Ho, *J. Phys. Chem. B*, 2005, **109**, 16628–16635.

[196] N. Matsumi, K. Naka and Y. Chujo, *J. Am. Chem. Soc.*, 1998, **120**, 5112–5113.

[197] Z. Yuan, N. J. Taylor, T. B. Marder, I. D. Williams, S. K. Kurtz and L. T. Cheng, *J. Chem. Soc. Chem. Comm.*, 1990, 1489–1492.

[198] M. Charlot, L. Porres, C. D. Entwistle, A. Beeby, T. B. Marder and M. Blanchard-Desce, *Phys. Chem. Chem. Phys.*, 2005, **7**, 600–606.

[199] M. Elbing and G. C. Bazan, *Angew. Chem. Int. Ed.*, 2008, **47**, 834–838.

[200] I. A. I. Mkhalid, J. H. Barnard, T. B. Marder, J. M. Murphy and J. F. Hartwig, *Chem. Rev.*, 2010, **110**, 890–931.

[201] B. Stevens and E. Hutton, *Nature*, 1960, **186**, 1045–1046.

[202] N. J. Turro, in *Modern molecular photochemistry*, Mill Valley, Calif. : University Science Books, 1991.

[203] T. Forster and K. Kasper, *Z. Phys. Chem.*, 1955, **59**, 976–980.

[204] R. Huenerbein and S. Grimme, *Chem. Phys.*, 2008, **343**, 362–371.

[205] C. Moore, *Atomic Energy Levels*, U.S. Natl. Bur. Stand. Circ. No. 467, 1949, vol. I.

[206] T. Rocha-Rinza and O. Christiansen, *Chem. Phys. Lett.*, 2009, **482**, 44–49.

[207] R. F. Fink, J. Pfister, H. M. Zhao and B. Engels, *Chem. Phys.*, 2008, **346**, 275–285.

[208] J. C. Amicangelo, *J. Phys. Chem. A*, 2005, **109**, 9174–9182.

[209] A. Langseth and B. P. Stoicheff, *Can. J. Phys.*, 1956, **34**, 350–353.

[210] T. Forster, *Ann. Phys.*, 1948, **2**, 55–75.

[211] E. Zingher, S. Kendler and Y. Haas, *Chem. Phys. Lett.*, 1996, **254**, 213–222.

[212] J. A. Syage, F. Aladel and A. H. Zewail, *Chem. Phys. Lett.*, 1983, **103**, 15–22.

[213] G. Wald, *Nature*, 1968, **219**, 800.

[214] R. Send, D. Sundholm, M. P. Johansson and F. Pawłowski, *J. Chem. Theory Comput.*, 2009, **5**, 2401–2414.

[215] M. Wanko, M. Hoffmann, T. Frauenheim and M. Elstner, *J. Comput. Aided Mol. Des.*, 2006, **20**, 511–518.

[216] M. Wanko, M. Hoffmann, P. Strodel, A. Koslowski, W. Thiel, F. Neese, T. Frauenheim and M. Elstner, *J. Phys. Chem. B*, 2005, **109**, 3606–3615.

[217] R. Send and D. Sundholm, *J. Phys. Chem. A*, 2007, **111**, 8766–8773.

[218] I. V. Rostov, R. D. Amos, R. Kobayashi, G. Scalmani and M. J. Frisch, *J. Phys. Chem. B*, 2010, **114**, 5547–5555.

[219] R. Send and D. Sundholm, *Phys. Chem. Chem. Phys.*, 2007, **9**, 2862–2867.

[220] G. G. Kochendoerfer, S. W. Lin, T. P. Sakmar and R. A. Mathies, *Trends Biochem. Sci.*, 1999, **24**, 300–305.

[221] S. L. Logunov, L. Song and M. A. ElSayed, *J. Phys. Chem.*, 1996, **100**, 18586–18591.

[222] F. Neese, *J. Chem. Phys.*, 2003, **119**, 9428–9443.

[223] R. R. Zaari and S. Y. Wong, *Chem. Phys. Lett.*, 2009, **469**, 224–228.

[224] W. J. DeGrip, Bovee-Geurts, I. van der Hoef and J. Lugtenburg, *J. Am. Chem. Soc.*, 2007, **129**, 13265–13269.

[225] C. A. Guido, B. Mennucci, D. Jacquemin and C. Adamo, *Phys. Chem. Chem. Phys.*, 2010, **12**, 8016–8023.

[226] P. Wiggins, J. A. G. Williams and D. J. Tozer, *J. Chem. Phys.*, 2009, **131**, 091101.

[227] J. Plotner, D. J. Tozer and A. Dreuw, *J. Chem. Theory Comput.*, 2010, **6**, 2315–2324.

[228] M. R. Silva-Junior, M. Schreiber, S. P. A. Sauer and W. Thiel, *J. Chem. Phys.*, 2008, **129**, 104103.

[229] D. Jacquemin, E. A. Perpete, I. Ciofini and C. Adamo, *J. Chem. Theory Comput.*, 2010, **6**, 1532–1537.